ELECTRICAL CHARACTERIZATION OF NICKEL OXIDE AND NICKEL IRON OXIDE THIN FILMS AND RESISTIVE RANDOM ACCESS MEMORY DEVICES GROWN BY RADIO FREQUENCY SPUTTERING

by

James Nicholas Talbert, B.S.

A thesis submitted to the Graduate Council of
Texas State University in partial fulfillment
of the requirements for the degree of
Master of Science
with a Major in Physics
December 2019

Committee Members:

Wilhelmus J. Geerts, Chair

Luisa Scolfaro

Alexander Zakhidov

FAIR USE AND AUTHOR'S PERMISSION STATEMENT

Fair Use

Duplication Permission

ACKNOWLEDGEMENTS

I would like to present my gratitude for Dr. Wilhelmus Geerts for his patience and guidance throughout this thesis project as well as my graduate studies. I would also like to thank my thesis committee members Dr. Scolfaro and Dr. Zakhidov for their knowledge and understanding. I thank my peers for their constant support and help, Samuel Cantrell, Beth Leblanc, Abdul Ahad Talukder, Chandler Hutton, Egla Madrid, Lauren Henderson, Anival Ayala, Jaime Ruiz, and Shankara Acharya. I thank my family for pushing through the hard times and their constant support. I would like to send a big thank you to the physics department at Texas State for being so inclusive and making me feel part of the family with the learning assistant program and recruitment programs.

I acknowledge financial support from Texas State University, DOD (HBCU/MI grant W911NF-15-1-0394), and DOD HBCU/MI equipment/instrumentation grant (W911NF-16-R-0024). Furthermore, I would like to thank Dr. Casey Smith and the ARSC for training and support. I would like to thank Texas State University for travel support to the Materials Research Society Spring Conference in Phoenix, Arizona 2019.

Part of this thesis was published in the following conference proceedings:

[1] Binod D.C., Andres Oliva, Anival Ayala, Shankar Acharya, Fidele Twagirayezu, James Nick Talbert, Luisa M. Scolfaro, Wilhelmus J. Geerts, “Magnetic Properties of reactive co-sputtered NiFe-oxide samples”, IEEE Trans. on Magn. 55 (2019) 2900205, pp. 2900205-1-6, DOI: 10.1109/TMAG.2018.2866788.

[2] James N. Talbert, Samuel R. Cantrell, Md. Abdul Ahad Talukder, Luisa M. Scolfaro, Wilhelmus J. Geerts, "Electrical Characterization of Silicon - Nickel Iron Oxide Heterojunctions", MRS Advances, July 2019, DOI: 10.1557/adv.2019.321.

Furthermore, part of the thesis was presented at the following conferences:

[1] Nick Talbert, Wilhelmus J. Geerts, Luisa M. Scolfaro, “Electrical Characterization of Silicon Nickel Iron Oxide heterojunctions”, poster presentation at MRS Spring meeting Spring 2019, April 22-26.

[2] James Nick Talbert, Wilhelmus J. Geerts, Luisa Scolfaro, “Electrical Characterization of Nickel oxide and Nickel Iron Oxide Thin Films and Resistive Random Access Memory Devices grown by Radio Frequency Sputtering”, oral presentation at Fall-2018 TSAPS meeting, October 15, Houston.

[3] James Nicholas Talbert, Darrell Adams, Jose Mayorga, Wilhelmus J. Geerts, “Measurement Setup for Resistivity RAM Devices”, poster presentation at the Fall-2016 joint meeting of the TSAPS and the 4 corners section of the APS, Las Cruces, New Mexico, October 2016.

[4] Chandler Hutton, Ahad Talukder, Wilhelmus J. Geerts, James Nicholas Talbert, "Electrical Characterization of Thin Films", Joint Fall 2017 Meeting of the Texas Section of the APS, Texas Section of the AAPT, and Zone 13 of the Society of Physics Students, Richardson, Texas, October 2017.

[5] Binod D.C., Andres Oliva, Anival Ayala, Shankar Acharya, Fidele Twagirayezu, James Nick Talbert, Luisa Scolfaro, Wilhelmus Geerts, "Magnetic Properties of reactive sputtered NiFe-oxide samples", poster presentation at the International Conference on Magnetism 2018, July 18, San Francisco.

[6] Brian Collier, Wilhelmus Geerts, Ahad Talukder, James Nicholas Talbert, Aaron Medina, Andres Oliva, "Magneto-Optical Faraday Effect in NiO and NiFeO Thin Films", oral presentation at the Joint Fall 2017 Meeting of the Texas Section of the APS, Texas Section of the AAPT, and Zone 13 of the Society of Physics Students, Richardson, Texas, October 2017.

[7] Clint Boldt, Md. Abdul Ahad Talukder, James Nicholas Talbert, Luisa Scolfaro, Wilhelmus J. Geerts, "Properties of carrier traps in diode and RRAM device via DLTS", poster presentation at the Fall-2018 TSAPS, October 15, Houston.

TABLE OF CONTENTS

Page

LIST OF TABLES

Table **Page**

LIST OF FIGURES

Figure **Page**

ABSTRACT

The electrical properties of Radio Frequency Sputtered NiFeO and NiO films deposited on n and p-type Silicon was investigated for two different oxygen flows. Rectifying properties for $Ni_{0.8}Fe_{0.2}O_{\alpha}$ on n-Si showed $I_{forward}/I_{reverse}$ >10,000 for $\alpha>1$ and $I_{forward}/I_{reverse}$ >50 for $\alpha<1$. Both types of devices have opposite forward biases. Resistive switching was found for low oxygen samples but not for high oxygen flow samples. Results suggest that NiFeO sputtered at high oxygen flow is p-type. For NiO and NiFeO on p-Si no strong rectifying properties were observed. The specific contact resistivity of $Pt/Ni_{0.9}Fe_{0.1}O_{\alpha}$ ($\alpha>1$) was estimated from the difference between the 2pp and 4pp resistance ($0.0007 \pm 0.0003\ \Omega\ cm^2$). The carrier concentration and mobility for high oxygen flow samples were calculated using the perpendicular resistivity and transition voltage between Ohmic and V^2 behavior and were $5.73 \times 10^{17}\ cm^{-3}$ and $8.6 \times 10^{-4}\ cm^2/Vs$. This mobility does not tell which charge carrier is dominating. Through CV analysis the acceptor mobility was calculated to be approximately $8 \times 10^{-3}\ cm^2/Vs$. The acceptor concentration for NiFeO was approximated to be $8 \times 10^{16}\ cm^{-3}$ through CV analysis.

I. INTRODUCTION

NiO thin films have been investigated extensively for various applications, namely as a p-type transparent conducting oxide for application in semiconductor devices and as a switching medium in Resistive-RAM (RRAM) memory devices. Films sputtered at low oxygen flow show presence of oxygen vacancy clusters that can be moved in and out of the thin film layer by electric fields and thermal processes. This allows for the reversible change of the resistance of a metal/oxide/metal device using an applied electric potential that is limited by the compliance of the source with the low resistance state of RRAM being metallic and the high resistance state being semiconducting [1][2]. These RRAM devices can be switched much faster, have a smaller footprint, and are less sensitive to radiation than the currently used flash memory in mobile devices.

NiO thin films prepared at high oxygen flow are believed to contain metal vacancies that behave like acceptors and generate mobile holes. As NiO has a bandgap of about 4 eV, such films fall into the category of transparent conductive oxides and are of interest for applications in novel semiconductor devices as electron blockers or p-type emitters [3][4][5][6]. In this thesis project the electrical properties of RF sputtered NiFeO thin films are studied, specifically the properties of heterojunction devices on silicon. The resistivity of ion-beam sputtered reactive NiFeO thin films is approximately $4x10^3$ Ω cm and appears to increase with temperature suggesting as sputtered NiFeO is a semiconductor [7].

II. PREVIOUS STUDIES

The previous research on Nickel Oxide (NiO) and Nickel Iron Oxide (NiFeO) heterojunctions is reviewed in this chapter. The following sections summarizes the specific work done by the author listed at the head of each sub-section.

Alexander H. Berg [8] NiO thin films were grown on n-Si wafers by atomic layer deposition (ALD) and proved to be a first step to high performing selective electron blocking heterojunctions. Two different metals were used for the electrodes (i.e. Al, Ag). The electrical characterization showed a change in the current density when a 15 nm NiO film was added in-between the electrode and the Silicon wafer. Rectifying behavior was observed for the metal Silicon film stack with current densities at $J = 4.8 \times 10^{-5}$ A/cm^2 and $J = 8.2 \times 10^{-6}$ A/cm^2 for Ag and Al respectively. When a NiO film was used in between the electrodes and the silicon, the current densities in forward bias decreased to $J = 6.8 \times 10^{-8}$ A/cm^2 and $J = 5 \times 10^{-2}$ A/cm^2 for Ag and Al respectively. The cause for this change was reported as the passivation of Si by the NiO and the depinning of the Fermi level which made the Schottky barrier height dependent on the metal's work function. The built-in voltage was determined from C-V measurements using a $1/C^2 - V$ curve. The addition of NiO to the film stack increased the built-in voltage (i.e. $V_{bi} = 0.42$V to $V_{bi} = 0.55$V). This shift to a higher built-in voltage is caused by the depinning of the Fermi level and is consistent with their I-V data.

Francesca Menchini [6]NiO thin films were investigated for the purpose of an emitter layer in Si-based heterojunction solar cells due to the oxide layer having a desirable hole collection selectivity. NiO thin films were grown using radio frequency

(RF) sputtering at room temperature. The sputtering parameters were set to the following: base pressure = 7.5E-7 Torr, Ar percent gas flow = 33%, O_2 percent gas flow = 67%, Sputtering pressure = 13.5 mTorr, RF power = 50W. The optoelectronic properties were examined using a multitude of techniques that include UV-Vis-NIR spectrophotometer, four point probe, liquid nitrogen cryostatic system, ultraviolet photoelectron spectroscopy (UPS), Keithley SMU 236 electrometer. The NiO films had a transmittance of 63.9% at the 550 nm, 120kΩ/cm^2 sheet resistance that corresponds to a resistivity of 0.24 Ωcm where the thickness determined was 20 nm. The activation energy was estimated as E_a = 0.19eV between the range of 100-345 K. From the UPS measurements the electron affinity was determined to be χ = 1.8eV. The current density – voltage (JV) characteristics were measured in the dark and under light exposure (right graph) and displayed the relationships shown in the figure below. Under light exposure (right graph) the IV curve drastically changes for small voltages. Calculations using DIFFIN showed that the s-shaped curve is due to interface defects (1.8E13 cm^{-2}) at the cSi-NiO interface. The presence of defects at the Si-NiO interface cause the bands to bend down near the interface and will not keep electrons from approaching the interface. So, RF sputtered NiO might not be a good electron blocker as electrons will be able to approach the interface and recombine with holes via interface defects. The dark J-V characteristic of the heterojunction could be modeled by the three diode model shown in figure 1 on the left. The following parameters were used to model the J-V data in table 1.

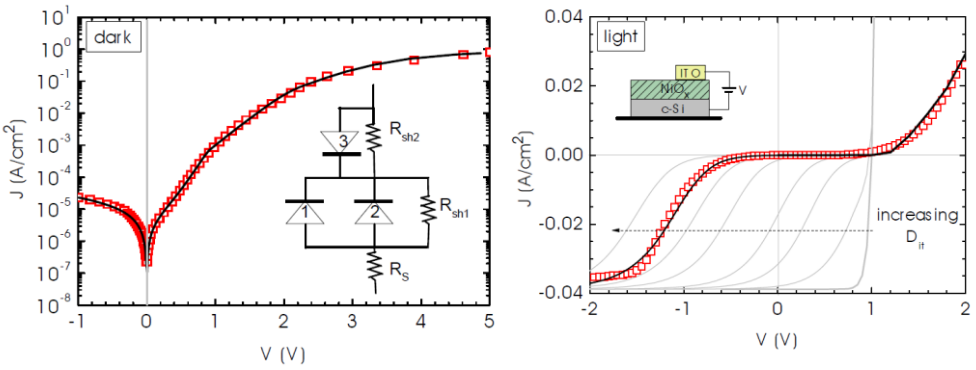

Figure 1. J-V relationship modeled by three diode system. (a) Squares display raw dark J-V characteristics of a heterojunction formed by a p-type 20nm NiO film grown on a n-type Si wafer. The data was fitted using a three diode circuit and is displayed with the solid line; (b) The graph on the right shows the H-V curve under light exposure. The squares are the measurement data and the solid line the result of a calculation assuming an interface defect density of 2×10^{13} cm^{-3} [6].

Table 1. Three Diode Model Fit Parameters.[6]

Diode 1		Diode 2		Diode 3	
J_0 (A)	n	J_0 (A)	n	J_0 (A)	n
8.38×10^{-12}	3.84	1.35×10^{-6}	5.52	1.89×10^{-5}	1.12
R_{sh1} (Ω)		R_{sh2} (Ω)		R_S (Ω)	
2.69×10^{6}		4.59×10^{4}		2.93	

Maclyn Compton [9]. Permalloy Oxide ($Ni_{80}Fe_{20}O_{a<1}$ or PyO) thin films were grown using dual ion beam sputtering. This deposition method is ideal when trying to fabricate magnetic oxides by sputtering using very low pressures (i.e. $\approx10^{-7}$ Torr). Films were grown on three different substrates including SiO_2 / Si, Al / Si, and soda glass. Optical transmission and resistivity measurements were done on the PyO films deposited on soda glass substrates due to the optical properties. Due to a high refraction index of PyO (i.e. above 2) the 65-75% transmission in the near infrared (500-600 nm) is not caused by absorption in the oxide but by reflection. Ellipsometric data has not revealed whether PyO has a direct or indirect bandgap. With an oxygen flow rate of 10 sccm and a

glass substrate the PyO resistivity approximated to (3.6-5.0)×10^3 Ω cm. Magnetic moment measurements were taken with a physical property measurement system (PPMS) from Quantum Design which is a liquid helium cooled system that uses a superconducting magnet. This system allows low temperature measurements (300K-1.9K) in a magnetic field on the order of 9 T. These measurements revealed a small ferromagnetic component to the films with a magnetic moment smaller than 10^{-8} Am^2. The dielectric constant had a value of 522 at 320 Hz and decreased with frequency down to 16.6 at 8 MHz. It was not clear from Compton's results what the conduction mechanism is in NiO, conduction in the band or hopping.

Yubo Cui [10]. PyO thin films were grown using RF magnetron sputtering using an oxygen gas flow of 2 sccm and an argon gas flow of 8 sccm which corresponds to a sputter pressure of approximately 10^{-3} Torr. Different substrate temperatures were used in the fabrication process (i.e. 300K – 861.15K) as well as a range of deposition times (38-1200s) and an oxygen flow series (i.e. 5-20%) was made. Two iron concentrations were studied (10-19 at.%) in this thesis. Measurements systems used to characterize the samples include: ellipsometer, four point probe, electron microscope, Energy-dispersive X-ray Spectroscopy (EDAX), atomic force microscopy (AFM).

FTIR measurements were taken on the temperature series and verified the rock salt crystal structure of the RF sputtered films [10]. Electrical characterization was performed on the thickness series and resistivity decreases strongly with the film thickness. For films of 50 nm the measured resistivity was around 4E5 Ohm.cm and for films of 150 nm thickness, the resistivity was around 3E4 Ohm.cm. These films were

$Ni_{0.8}Fe_{0.2}O$ that were sputtered at room temperature with a 20% oxygen flow rate out of a 10 sccm flow.

Atomic force microscopy was used to determine the surface roughness of PyO films grown on top of glass and SiO_2/Si substrates. The Ra-roughness of all films was slightly higher than the Ra-roughness of the substrates but well below 1 nm showing that RF sputtered NiFeO films are very smooth. No evidence for pin-holes was found. The figure below shows two AFM images from his thesis. Scanning electron microscopy studies on his samples also showed no pinholes. The following image presents the findings of the measurements in figure 2.

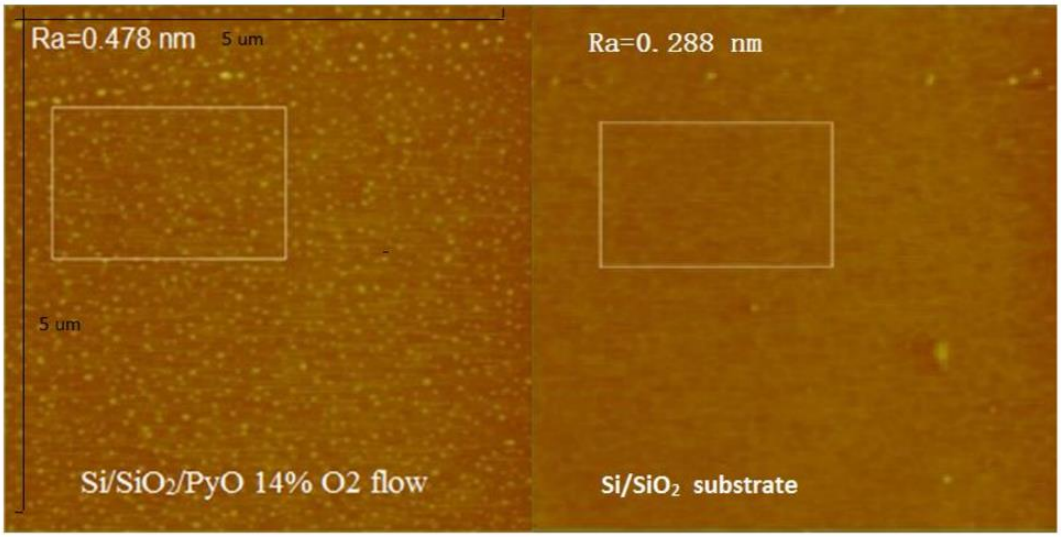

Figure 2. AFM images of Si/SiO_2 and PyO. AFM image of the surface of a Si/SiO2/PyO thin film sample (left) and Si/SiO2 substrate (right) including calculated Ra roughness.[10]

Ahad Talukder [11]. NiO and Fe-doped NiO thin films were grown using RF magnetron sputtering. Parameters for deposition were varied and studied for the goal of improving the oxide film. To improve the film homogeneity a larger sputter pressure was

used than in previous works [12]. Measurements for this thesis include thickness, roughness, microstructure orientation, electrical properties, and magnetic properties. Instruments used for these measurements include, ellipsometer, X-Ray reflectivity (XRR) X-Ray Diffraction (XRD), four point probe, and Physical property measurements system (PPMS), Magneto-Optical Kerr Magnetometry (MOKE), and Rutherford Backscattering (RBS). The thickness of the films determined from XRR and ellipsometer measurements were similar, but the roughness obtained with both techniques differed. Results concerning oxygen flow yielded a good deposition rate for low flows. However, for oxygen flows of 10 sccm and above, the deposition rate was much lower, i.e. 0.1 A/sec. X-Ray Diffraction (XRD) measured a rock salt crystal structure for all samples even though peaks got weaker for higher oxygen flow samples. The crystallite size and texture depend on the oxygen flow during deposition. For high pressure thick NiFeO films made with either high or low oxygen flows the dominant orientation is {111}. As for NiO made at high oxygen flows a {111} orientation is also obtained. The low oxygen flow for NiO shows a different orientation of {200}. The electrical properties of the films were investigated by a linear four point probe. The graph below shows the resistivity of NiO thin films as a function of the oxygen percentage in the sputter gas. The resistivity peaks at 10% oxygen flow (see Fig. 3 below). It is believed that this maximum corresponds to stochiometric like films. For higher oxygen flow the films are expected to contain metal vacancies which act like acceptors. At lower oxygen flow, the oxidation is not complete, and part of the films are metallic.

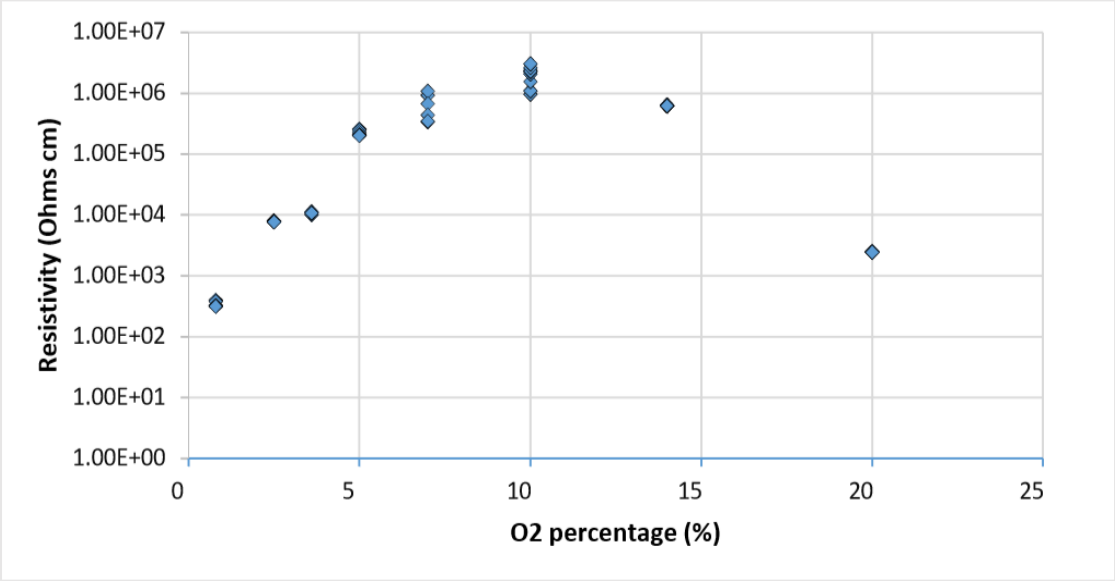

Figure 3. NiO Resistivity as a function of the oxygen concentration. In the sputter gas for high pressure RF sputtered NiO thin films [12][13].

Fidele Twagirayezu [14]. Density Functional Theory (DFT) using a Vienna ab initio Simulation Package (VASP) was used to calculate the electronic, optical and magnetic properties. A 4-atom NiO, 32-atom NiO, and a 32-atom Fe-doped NiO supercell all having a spin polarization in the {111} plane were the systems studied. The GGA and GGA + U were used to model and calculate the properties of each system and then compared to experimental results. The electronic properties of NiO and NiFeO are presented in density of states figure 4 below.

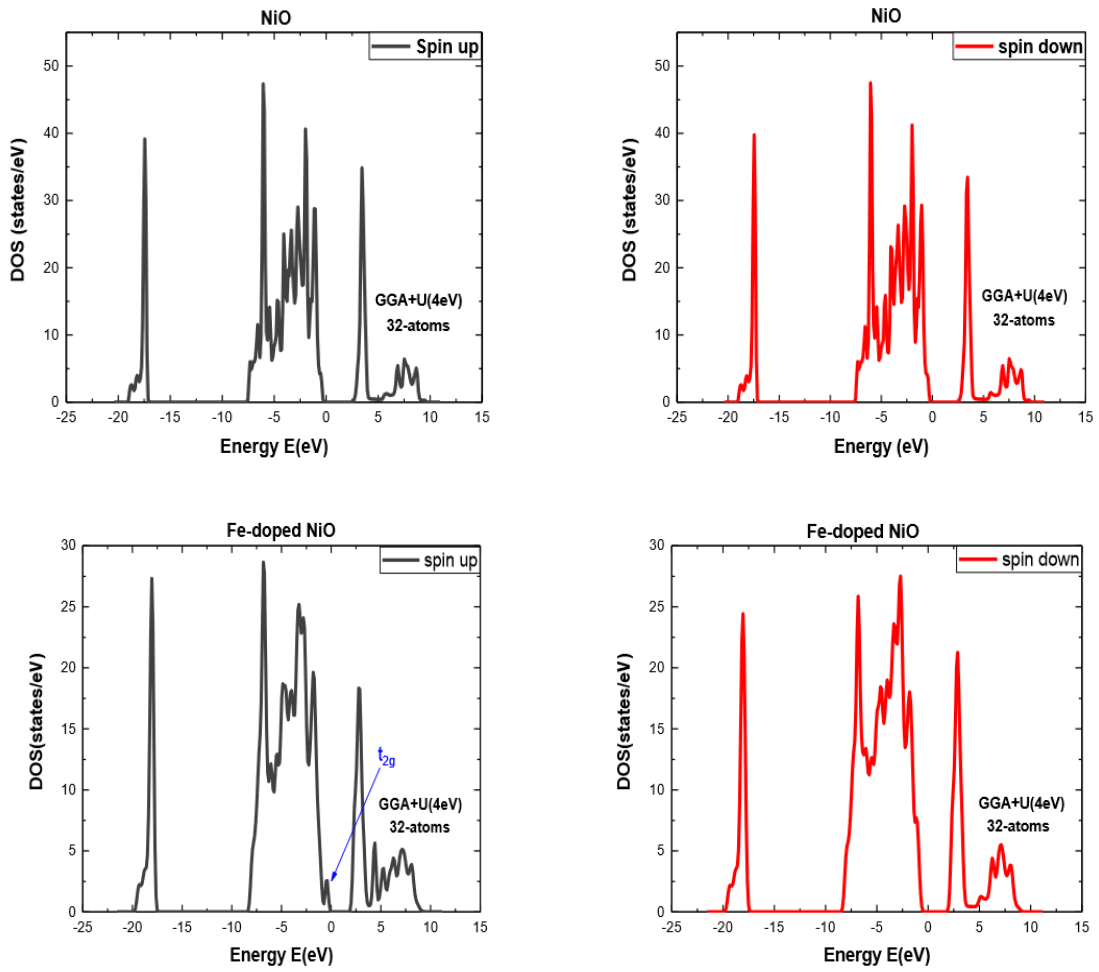

Figure 4. Density of States for NiO and NiFeO GGA+U. For spin up (left) and spin down bands (right) calculated using the GGA + U for a 32-atom model (U-J=2.5 eV).[14]

These results show that NiO has a higher bandgap than NiFeO with a difference of 0.5eV (i.e. NiO bandgap = 2.5eV and NiFeO bandgap = 2.0eV). These bandgap values are considerably lower than the experimental bandgaps of both materials. Better agreement between calculated and experimental bandgaps was obtained for calculations that used a larger U-value. The addition of Fe decreases the optical properties (i.e. dielectric function, the refractive index, the reflectivity, real optical conductivity and the absorption function) but increases the static refractive index from 2.2 to 2.25 along with static reflectivity from 0.14 to 0.15. The calculated optical properties measured by the

refractive index (n) in the lowest energy state for both materials agree with experimental data (i.e. 2.2 for NiO, and 2.25 for 6.25 at.% Fe-doped NiO). Using DFT the magnetic properties of NiO show an antiferromagnetic behavior, however the Ni and Fe magnetic moments differ from each other resulting in the supercell being ferri-magnetic because only one Fe replaces a Ni for 6.25%. If the concentration of doped Fe is doubled from 6.25 at.% to 12.5 at.% the magnetic properties change from ferri-magnetic to antiferromagnetic.

Deposition was done by RF sputtering where films of NiO and PyO were grown on SiO_2/Si substrates. The XRD results suggest no presence of impurity phases when Ni is doped with Fe. The premise to this conclusion is based on the six peaks measured in both NiO and Fe-doped NiO (i.e. {111}, {200}, {220}, {311}, {222} and {400}). Using the physical property measurement system (PPMS) the magnetic properties of NiO and PyO vary with oxygen and iron concentration. Higher magnetization was recorded for films sputtered at low oxygen flow rates and at room temperature. These film's magnetic moment increases as a function of temperature. Increasing the Fe doping increases the magnetization with a factor 4-6 for low oxygen flow conditions. For higher oxygen flows the magnetic moment decreases as the temperature increases. Note that the measured magnetization is very small, i.e. 0.1% of the saturation magnetization of pure nickel [26]. It is currently not clear if the residual magnetization originates from another phase, is due to defects or originates from the surface or grain boundaries in the thin films.

John Petersen [15]. The properties of transition metal oxides were studied using Density Functional Theory which include, structural, electronic, magnetic, and optical properties. Results on the structure of NiO is reported having a rock salt crystal structure.

The electronic properties are calculated using a GGA + U approach assuming U-J=5.3 eV. This U value was chosen as it resulted in several experimental and computed properties to agree which is represented in figure 5. The inclusion of Fe in NiO decreases the bandgap as indicated in figure 6 below.

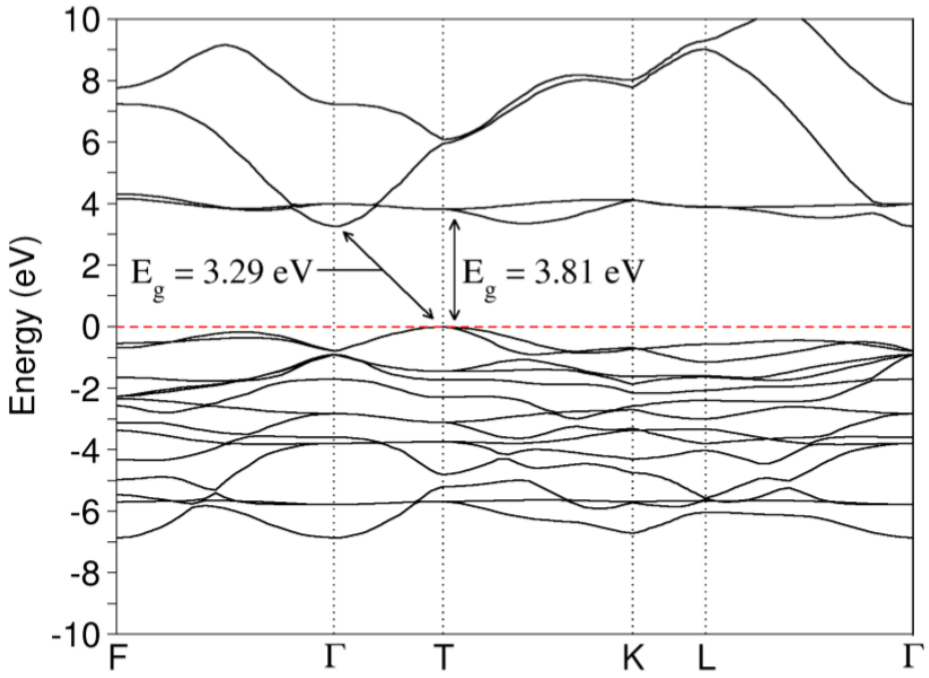

Figure 5 Model of Intrinsic NiO band structure, GGA + U (U-J=5.3 eV) 32- atom unit cell. An indirect band gap of 3.29 eV is observed between the Γ and T zones. At the T zone a larger direct band gap is observed of 3.81. The red dashed line defines the Fermi level of 0eV.[15]

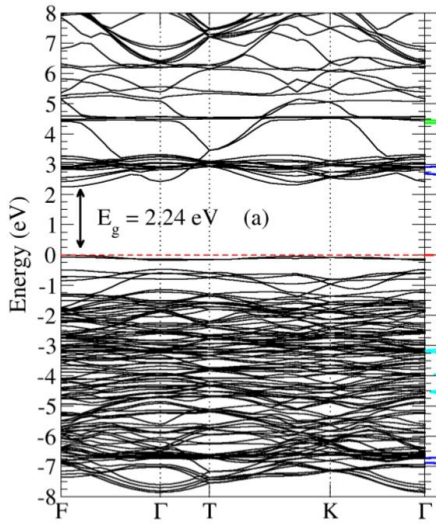

Figure 6. Band structure of $Ni_{0.75}Fe_{0.25}O$. The bandgap resides in the F zone as the red dashed line is the Fermi energy at 0eV.[15]

The optical properties of both NiO and NiFeO were calculated from the electronic band structures. Comparing the optical properties from NiFeO and NiO gives the following graphs in figure 7. The large peaks around 4 eV in the graphs indicate the bandgap. This absorption is caused by electron transitions from the valence band to the conduction band. For the Fe doped material the dielectric loss seems to be larger for photon energies between 2-3.5 eV indicating a smaller bandgap.

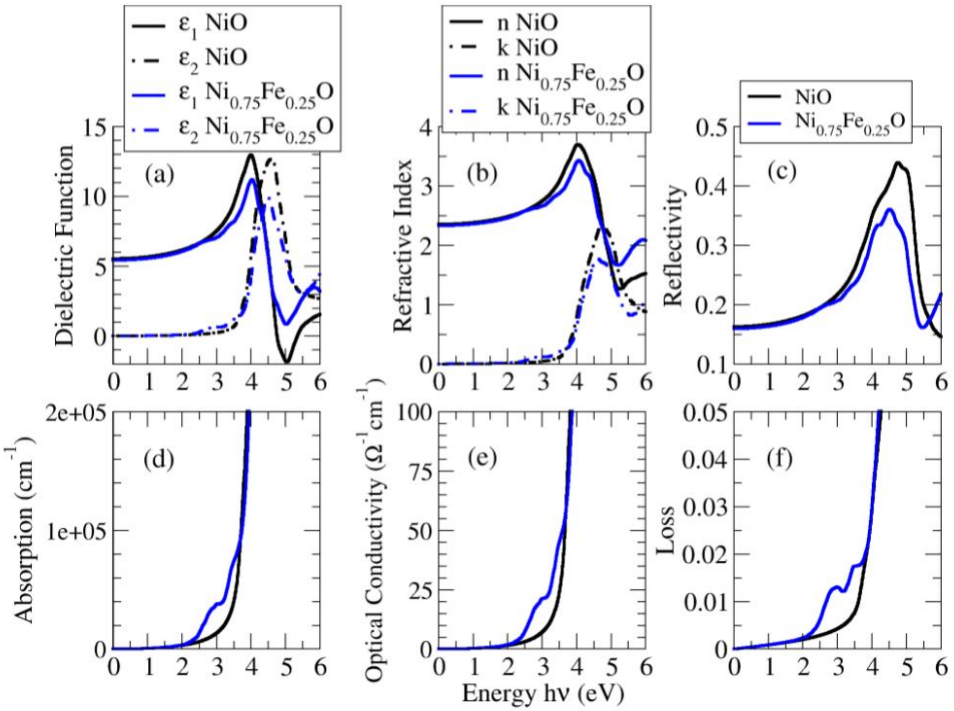

Figure 7. Optical properties of NiO vs $Ni_{0.75}Fe_{0.25}O$. (a) complex dielectric function, (b) complex refractive index, (c) reflectivity, (d) absorption, (e) optical conductivity, and (f) dielectric loss.[15]

III. FABRICATION

AJA Orion 8 Sputtering System

The AJA Orion 8 Sputtering System is an instrument that consists of a chamber, vacuum pumps, valves, metallic sources, and gauges. The purpose of this instrument is to fabricate the thin films and thin film devices presented in this thesis. The chamber has a specific geometric design to deposit multiple source materials onto a variety of substrates thereby creating thin films. The sputtering system operates in the high vacuum to ultra-high vacuum pressure range to minimize contaminations. Such vacuum is achieved by removing the atmosphere with pumps and thereby creating an approximate background pressure on the order of 10^{-7} to 10^{-8} Torr range. Deposition is done by RF and DC magnetron sputtering. The activation of target plasma which removes material from the sputter target (source) is achieved at a relatively high pressure from that of the base pressure. Introducing a nonreactive gas such as Argon into the chamber increases the pressure and permits a clean environment to create a plasma. The atoms removed from the sputter target obtain a momentum from the Ar atoms bombarding the target from the plasma. Therefore, a flux of target atoms is directed to the substrate and the substrate is plated with a thin film: the process of building devices begins.

This section is dedicated to the fundamental operation of the sputtering system. Vacuum pumps are essential to achieving the base pressure and thereby the removal of undesirable molecules and atoms. Different pumps are needed to step down the pressure within the chamber due to the limitations of their design and the particle-particle interactions. The AJA Orion 8 Sputtering System uses two different pumps, the roughing pump and the turbomolecular pump. These pumps function in the rough and high vacuum

regimes. As the pressure in the chamber decreases the difficulty of maintaining a vacuum increase because of continuous outgassing. Table 2 shows the functional pressure ranges for the pumps used in the sputtering system.

Table 2. Vacuum Pumps and their Ranges

Roughing Pump (Rough Vacuum)	760 to $1x10^{-3}$ torr (approx.)
Turbomolecular Pump (High Vacuum)	$1x10^{-3}$ to $1x10^{-8}$ torr (approx.)

At atmospheric pressure (i.e. 760 torr) and room temperature (i.e. 300 K) the molecules and atoms collide often with each other at great speeds. The concept that governs these interactions is called the mean free path. The mean free path is the average distance the particles travel before they collide. The mean free path depends inversely on the pressure inside the chamber. This can be derived using a hard sphere approximation [16]. The hard sphere approximation is widely used in the statistical mechanical theory of fluids-solids and uses the concept as impassable spheres that cannot occupy the same space. The value of the mean free path (λ) is described in equation 3.1 [16]. Where k is Boltzmann's constant, T is the temperature in Kelvin, πd^2 is the collision cross section, and P is the pressure in the chamber.

$$\lambda = \frac{kT}{\sqrt{2}\pi d^2 P} \tag{3.1}$$

The difference of the mean free path between atmospheric and sputter pressure is of an order 10^6 and for high vacuum the difference is 10^8. The magnitude of the mean free path at atmospheric pressure is a couple of micrometers. This mean free path for rough vacuum is much less than the length of the chamber and therefore the molecules of

the gas mainly collide with each other. This interaction falls within the viscous flow regime and equation 3.1 is applicable. At lower pressure the interaction of the molecules with each other decreases and collisions are mainly with the casing, the walls of the vacuum system. This vacuum regime is referred to as the molecular flow regime. The quantity that describes what flow regime a system is within is called the Knudsen number (Kn) which depends on the ratio of the gas's mean free path and the dimensions of the system (i.e. the diameter of the chamber). Table 3 shows the vacuum flow regimes with the associated Knudsen number range for the AJA system.

Table 3. Vacuum Flow Regimes

Vacuum Flow Regimes		AJA Pressure Ranges
Molecular Flow	Kn > 1	~10^{-4} – 10^{-8} Torr
Intermediate Flow	1 > Kn > 0.01	~10^{-1} – 10^{-4} Torr
Viscous Flow	Kn < 0.01	~760 – 10^{-1} Torr

So, it is thereby concluded that the particle-particle collisions dominate the interaction in the chamber at atmospheric pressures.

As shown in Figure 8 the turbomolecular pump inlet is connected to the vacuum chamber and is also in series with the roughing pump. This design is required as most turbopumps will get damaged if their outlet is at atmospheric pressure and takes advantage of the vacuum flow regimes in the sense of conductance.

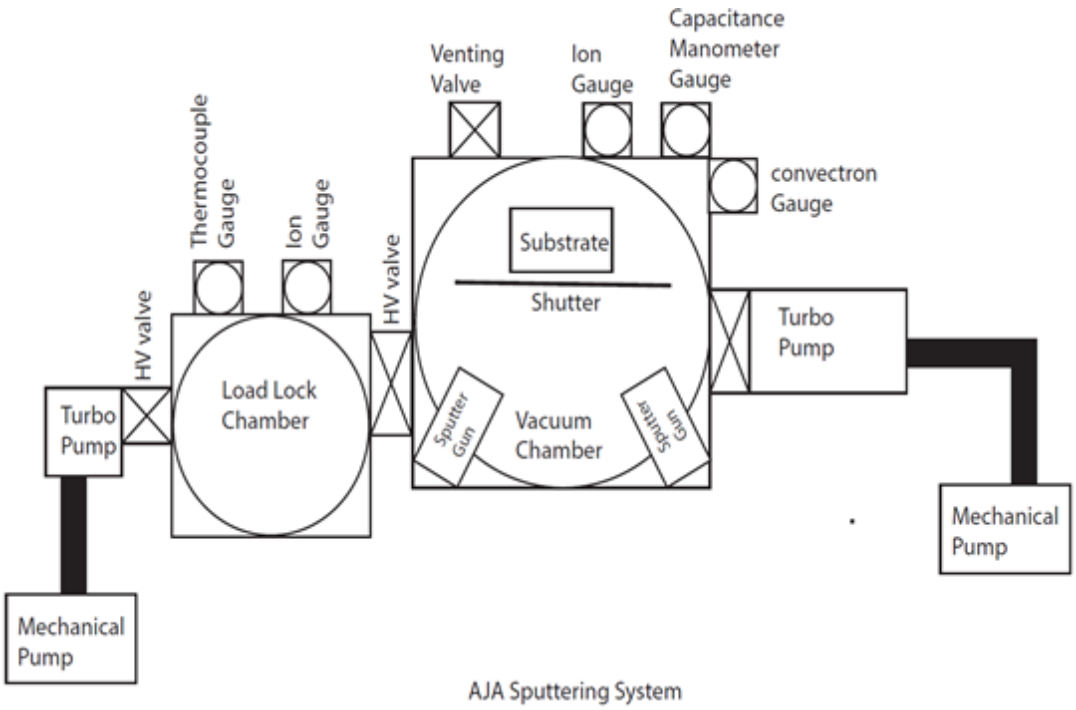

Figure 8. AJA Orion 8 Sputtering System Blueprints

The conductance (C) in the viscous flow regime depends on pressure and the dimensions of the conduit that the fluid is transported through. Equation 3.2 shows the conductance in the Viscous Flow Regime [17][18].

$$C = \frac{184(P_2+P_1)D^4}{2L} \tag{3.2}$$

Where P_2 is the pressure in Torr at the vacuum side of the tube and P_1 is the atmospheric pressure in Torr, D represents the diameter of the conduit, and L is the length from the chamber to the discharge pump. As for the molecular flow regime the following equation provides the relationship between conductance of a pipe of length L and diameter D: [18][17].

$$C = \frac{12.2D^3}{L} \tag{3.3}$$

When pumps and hoses are connected in series the conductance is given by the following equation.

$$\frac{1}{C_{system}} = \frac{1}{C_1} + \frac{1}{C_2} + \frac{1}{C_3} + \cdots \quad (3.4)$$

In the Viscous Flow Regime conductance is much larger than in the Molecular Flow Regime as shown by equations 3.3 and 3.2. The former also depends on the pressure difference and is proportional to D^4. So, pumps that work in the molecular flow regime require larger diameter tubing. Therefore, a higher gas flow will occur during the viscous flow than during the molecular flow regime, due to the conductance being greater. As the pressure transitions to the high vacuum state molecular interaction decreases and the Knudsen number becomes greater than one. This state is called the molecular flow regime where the mean free path increases beyond the dimensions of chamber. This increase causes the molecular-wall interaction to dominate the motion of the particles which makes removal of said particles harder. To increase the probability of taking the molecules out of the system a large inlet connected directly to the chamber is needed. This design concept is implemented in the AJA Orion 8 Sputtering System with the turbomolecular pump connected directly to the vacuum chamber using a large diameter valve and the roughing pump connected to the outlet of the turbo pump using a smaller diameter tube.

Roughing Pump: The low Vacuum Regime

The standard operating procedure for creating a vacuum in a chamber requires first and foremost a stage called roughing the chamber. This stage will result in an approximate pressure of 10^{-3} Torr using a pump often referred to as the roughing or

mechanical pump. These pumps use a concept called positive displacement. This concept alters the motion of the particles such that they are transferred from low to high pressure ambient. The mechanical pump uses two eccentric figure eight rotators where one is connected to a motor and the other is connected via gears. The following figure 9 depicts the mechanical structure of a roughing pump.

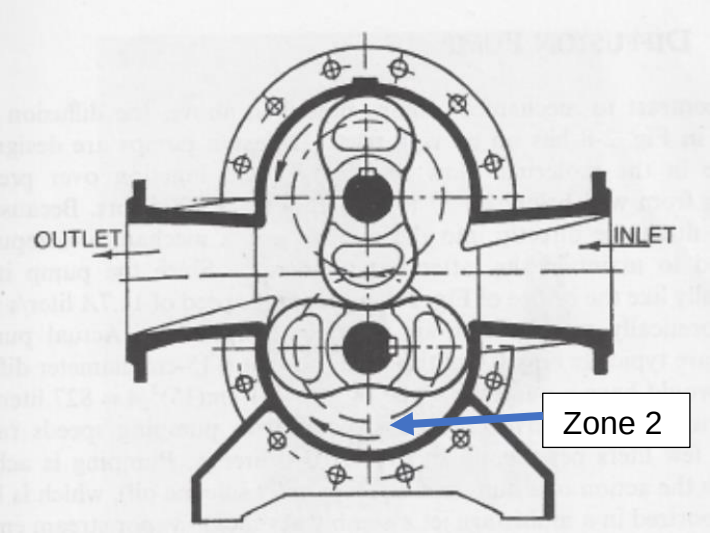

Figure 9. Roughing pump Cross section schematics. [17]

Roughing pumps function in the viscous flow regime by the compression of gas. As the gas flows in from the inlet there are two paths that lead to the outlet. The gas is isolated from the inlets by the rotors increasing the pressure of the gas in zone 2 where the volume is decreased. As the rotors turn exposing the compressed zone 2 gas to a lower pressure the gas flows to the outlet. Multi-stage root pumps (i.e. roughing pumps) are one of the expensive viscous flow regime pumps. These pumps do not need oil as a lubricant and thus are referred to as dry pumps. There are many types of pumps that function in the viscous flow regime which include oil-sealed and dry pumps. Instead of a

lubricant the root pumps have a small clearance of about 0.1 mm from the rotators to the walls of the pump and rotators and walls of the pump are coated with Teflon. For deposition systems, oil-sealed pumps are not favorable due to the inevitable contamination of the vacuum system by the oil. As the pressure decreases inside the chamber back-streaming of oil from the pump into the vacuum chamber (i.e. oil flowing into the chamber) can contaminate the vacuum system. The pump oil will enter the vacuum system as a gas and condense on objects in the chamber thus contaminating the system. This situation could also contaminate any samples being made which will disrupt the stoichiometry making the analyses of any characterization unclear. When oxygen gas is used during the sputtering process, oxidation of the oil and other parts of the pump can limit the oil's and pump's lifetime. Thus, for the viscous flow regime an oil free Alcatel ACP-40 G multi-stage root pump is used in the AJA Orion 8 sputtering system. The roughing pump is connected to the back of the turbomolecular pump which allows for fast pump down speeds.

Turbomolecular Pump: The High Vacuum Regime

The next step in the standard operating procedure for creating a vacuum in a chamber requires a pump that operates in the molecular flow regime. This stage will result in an approximate pressure of 10^{-8} Torr. The AJA system uses a turbomolecular pump. These pumps use a concept called kinetic or momentum transfer. The turbomolecular pump has several stages that includes rotating (rotors) and stationary blades (stators). The rotor and stator are a few millimeters apart and the pair create a stage, the pump has many stages. The rotors maximum angular speed is approximately 35,000 r.p.m with compression ratios up to 10^9 for molecules such as N_2. As the

compression ratio depends exponentially on the square root of the mass of the particle and the tangential velocity of the rotors. High compression ratios make the back-streaming neglectable. The stator is a stationary layer that is designed for volume changes to create a pressure gradient. When a rotor is right above a stator this function is similar to zone 2 in a roughing pump. The following figure 10 depicts the general mechanical design of a turbomolecular pump.

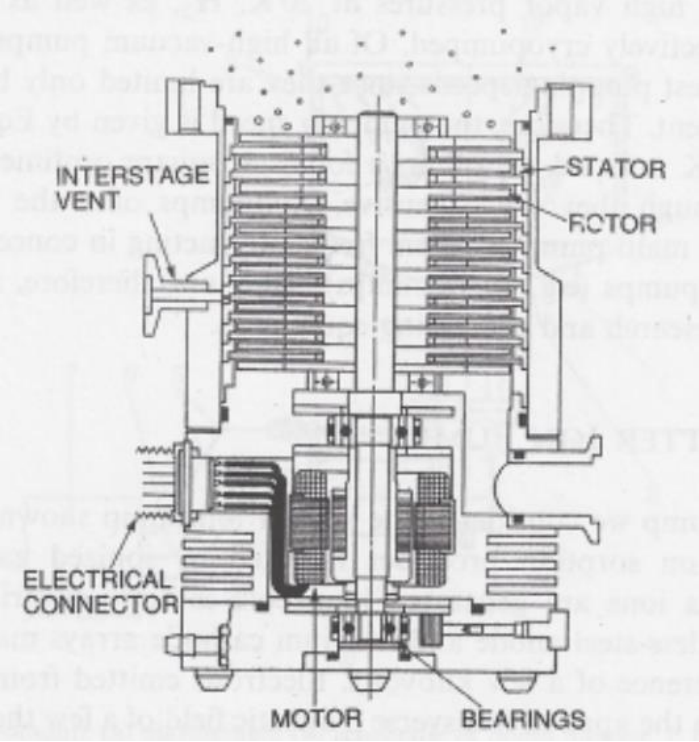

Figure 10. Turbomolecular pump schematics of cross section. [17]

In the molecular flow regime, the dominating interaction is molecular-wall response, where the mean free path is the largest. This means that the gas molecules will collide with the blades rather than with each other. As a collision occurs the rotor blades transfer momentum to the particles which accelerates them to the stator. The momentums

of the blades are so large that the incident angle of the particle does not matter and so is reflected by a telescopic angle of 180°. Rotors near the inlet have large angles to increase probability of collision. While stages near the outlet have smaller angles for increased compression to match the pressure in the fore-line. The fore-line is the channel that connects the exhaust of the turbomolecular pump to the inlet of the roughing pump.

Every system has disadvantageous and the turbomolecular pump is no stranger to failure. Operation above 10^{-2} Torr can cause disaster in the turbomolecular pump. In the viscous flow regime, there is enough pressure to cause a bend in the rotor blades. Since the stator are stationary any contact between the rotor and the stator can lead to a crippling of the rotors and possible break them. If the turbomolecular pump is exposed to high pressure lift can occur in the rotors which can cause the load on the bearings to lessen. If this occurs the bearings can encounter each other and cause them to dimple. If the bearings are damaged, then the rotors will surely encounter the stators and the pump will irreversible break.

Direct Current Sputtering

The thin films fabricated for this thesis used a form of physical vapor deposition called sputtering. There were two sputtering methods used to create the devices: Radio Frequency and Direct Current magnetron sputtering. The system geometry consists of two parallel metal electrodes one of which is the cathode or target of the metal to be deposited and the other is the substrate. Connected to the cathode is a voltage source. The anode faces the cathode and is usually grounded but can be heated, biased positively or negatively, or some combination of these. After the chamber has been pumped down to the baseline pressure an inert gas is introduced into the system, typically argon. This gas

serves as the medium for electrical discharge. The gate valve is throttled to protect the turbopump from the amount of gas that is controlled by a mass flow controller. The introduction of argon increases the gas pressure in the vacuum system to 1-10 millitorr for the AJA system. A high pressure is required for the ignition of an electrical discharge above an RF or DC magnetron gun. To achieve a high pressure in the AJA system (up to 17 mTorr) the two Ar mass flow controllers are opened completely, resulting in an Ar flow of 150 sccm. In addition, the turbo-pump valve is throttled. When a visible flow discharge is sustained between the electrodes a current flow is observed and the metal from the target is deposited on the substrate. The concept that governs sputtering is momentum transfer through positive gas ions that strike the cathode and physically eject the metal targets atoms. Figure 11 displays the different areas where the charge carriers differ in the plasma between the two electrodes.

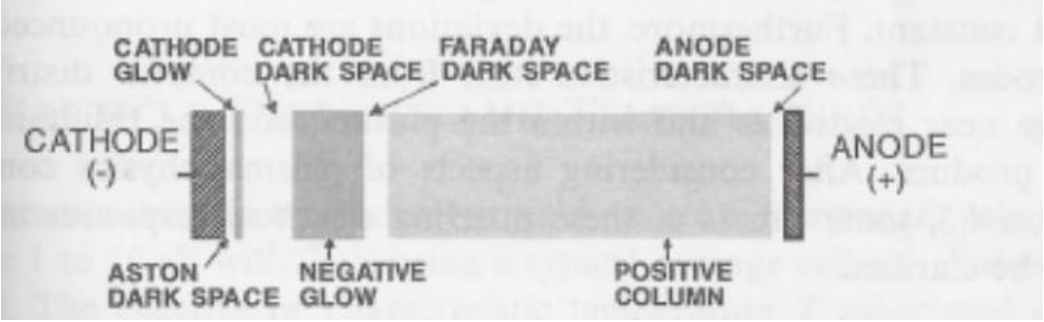

Figure 11. Plasma Schematics [17]

The Aston dark space has charge carriers of both high and low energy moving in opposite directions. The low energy carriers are the electrons and the high energy are the ions in this region. The cathode glow is the luminous layer where de-excitation of the ions is the probable mechanism for light emission. The dark space is where electrons

have very little energy and therefore do not have enough velocity to ionize. The dark space is also referred to as the sheath where most of the voltage drop occurs. The sheath is discussed in the next section. The electric field in the cathode dark space linearly increases from the cathode and serves to accelerate ions toward the cathode for collision. The negative glow is where secondary electrons and neutrals interact causing a visible emission. The substrate is typically placed in the negative glow area and therefore the Faraday dark space and positive column are not usually seen in a sputtering system. The ion charge density is greatest in the cathode dark space such that the electric field is also the greatest there. Whereas the electron charge density is greatest near the anode. The electric field is approximately zero in the positive column due to the net charge density being neutral. These concepts are graphed in figure 12.

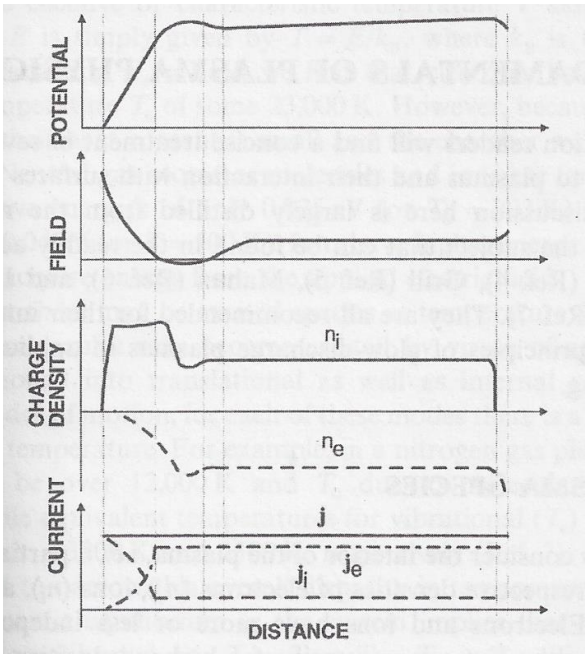

Figure 12. Electrical Characteristics of Plasma Schematics. [17]

The zones starting from left to right start with the Aston dark space all the way through the anode dark space. The thin film is grown from the ejected atoms that pass through the discharge region. The discharge region imitates a gaseous breakdown that can be compared to a dielectric breakdown in an insulating solid and converts the sputter gas above the target material to a plasma consisting of charged sputter gas ions, radicals, and free electrons. Breakdown occurs when the electrons gain the necessary energy for ionization cascade and thus requires a large distance between the electrodes. The loss of electrons or ions through sideways diffusion is minimized by the magnetron configuration and thus the size of the electrodes is irrelevant. This is due to the charged particles following a helix path from the force exerted by the magnetic field lines. The magnets are placed under the target and field lines extend above the target material causing charged particles to move along helical paths and increasing the probability for them to ionize more of the sputter gas. The figure 13 below depicts the different configurations needed depending on the magnetic properties of the target material.

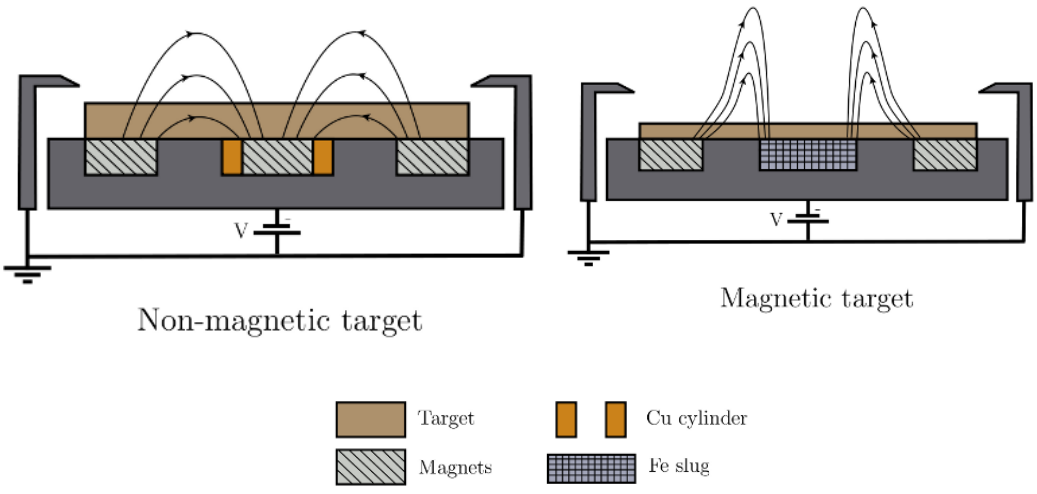

Figure 13. Magnetic Schematic For DC and RF sputtering. [19]

Different magnet configurations are needed to take advantage of the magnetic properties of the target material. For example, magnetic materials produce their own magnetic field and an iron slug is placed in exchange of a magnet so as not to increase the field at the target surface.

Radio Frequency Sputtering

Reactive Radio Frequency (RF) sputtering was used to fabricate the oxide layers of the devices presented in this thesis. The different electrical set up for DC and RF sputtering is depicted in figure 14.

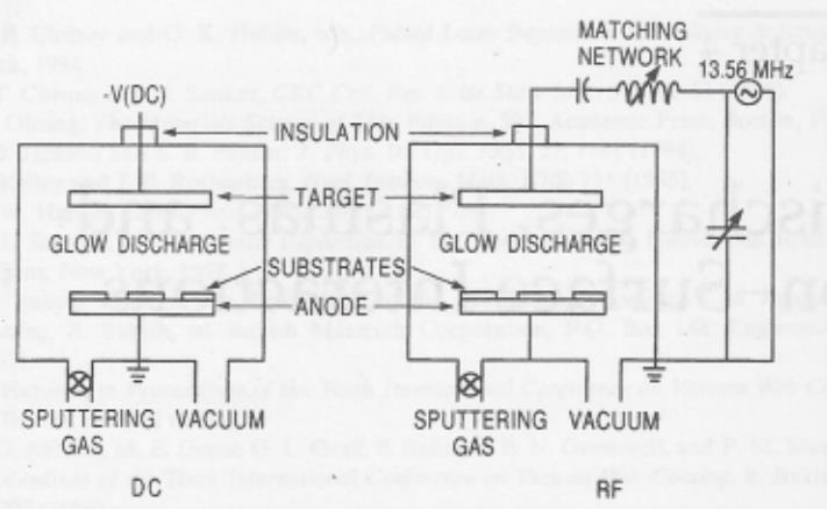

Figure 14. Basic Schematic for DC and RF sputtering. [17]

In addition to the Ar gas also O_2 gas is introduced in the vacuum during sputtering. During the sputtering process the oxygen gas will react with the permalloy. At high oxygen flows beyond 5 sccm, this reaction takes mainly place at the target's surface creating an insulating layer on top of the target material. Deposition rates decrease by the introduction of oxygen into the system because oxidation can occur on the target material

and the sputter rate of oxide is less than the sputter rate of metals. Also, DC sputtering of an insulating target leads to a decreasing sputter rate as charge builds up in the insulating material due to self-bias of the target where deposition occurs from positive ion-bombardment. Ultimately this can lead to target poisoning where the charge build-up in the oxides avoids Ar ions to reach the target surface. Charging effects can be avoided by using an RF power supply. The IV characteristics of a plasma are asymmetric for RF voltages due to the increased mobility of electrons compared to the ions. Since electrons have a smaller mass, they can easily follow the periodic change of an RF electric field. Positively charged electrodes induce a higher electron current (see the lowest graph in Fig. 12) than negatively charged electrodes due to the different mobilities of electrons and ions discharging the target. For this reason, the IV characteristics of a sputter chamber resembles a leaky rectifier or diode. Figure 15 shows the charge distribution as a function of the voltage and the different regions of charges that dominate in certain sections.

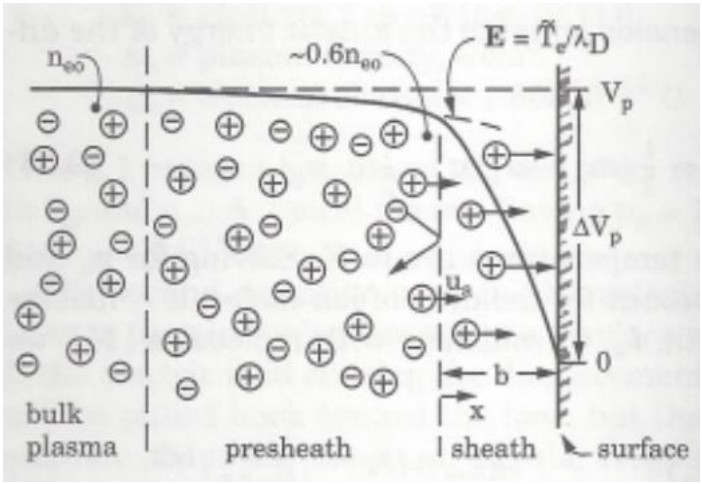

Figure 15. Charge distribution vs. voltage profile near the surface of a target material. Delta V is the anode sheath. [18]

In RF sputtering a frequency of ~ 1MHz is needed to ensure the necessary energy electrons need for ionizing collisions. DC sheath conditions apply at the target in cycles relative to the frequency. This frequency creates a pulsating sheath which causes the electrons to oscillate between the sheath and the plasma. During this oscillation, if timing is precise the electrons gain some additional energy from the expanding sheath when returning to the plasma. This expansion occurs when the cycles alternate from a cathode sheath to an anode sheath at the target surface. (page 212 of materials science of thin films). The expansion of the sheath depends on current flow which is the reason the cathode sheath is larger than the anodes. During the switch between sheaths the electric field repels electrons during the anode sheath cycle and gives the electrons extra energy to ionize excess atoms that are near. This results in the unnecessary relevance for secondary electrons to sustain the discharge like in DC sputtering. Summarizing: when using a radio frequencies power supply, the electrodes do not have to be conductors as continuous charging and discharging takes place at the target during the sputtering process. Thus, any material may be sputtered independent of its resistivity.

Gauges

The AJA Orion 8 sputtering system has several sensors to monitor temperature, pressure and thickness during the film growth. A thermocouple is connected off to the side of the substrate holder and measures via radiation the temperature of the sample holder. The devices made for this thesis were made at room temperature at approximate 18ºC.

The monitoring of the pressure inside the main chamber requires three gauges, an capacitance manometer which measures the pressure directly from the bending of a

diaphragm (i.e. direct measurement), a convection gauge which measures the pressure indirectly from the thermal conductivity of the gasses remaining in the vacuum system (i.e. indirect measurement), and a hot ionization gauge (i.e. indirect measurement). The ranges for these pressure gauges are different as well as their accuracies. The capacitance manometer contains a diaphragm (i.e. thin metal plate) that forms one or more capacitors with an electrode assembly. The capacitance of the capacitors depends on the pressure inside the chamber. This dependence is so because the pressure zone p3 in the following figure exerts a mechanical force upon the metal plate and decreases the gap between the three individual plates. Capacitance is defined as the following expression.

$$C = \frac{\varepsilon_o A}{d} \tag{3.5}$$

Where A is the area of the plates, ε_o is the permittivity of free space, and d is the gap between the plates. So, as d decreases then the capacitance increases. This gauge works so long as the reference pressure $P_r << P_3$. The upper pressure limit depends on the strength of the metal plate (diaphragm) or by the collapse of the gap between the plates. The capacitance manometer pressure gauge cannot be relied on in high vacuum condition and is also not reliable above 2×10^2 Torr. The capacitance manometer is independent of the gas that is introduced to the system and so measures the real pressure. The schematic is depicted in figure 16.

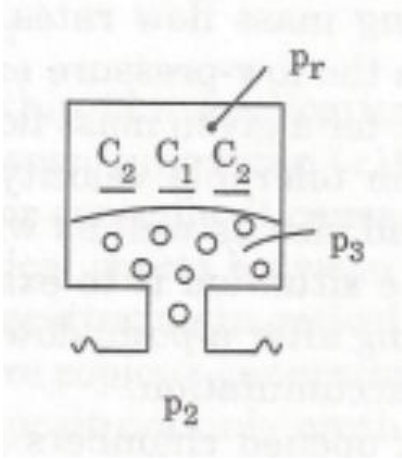

Figure 16. Capacitance Diaphragm Gauge Schematic[18]

The convection gauge consists of a gold-plated tungsten sensing wire and measures the convection currents to relay the pressure. The range on the convection gauge is reliable to 10^{-4} Torr and does depend on the gas that is used for sputtering. The gauge is calibrated for N_2 gas and since Ar is primarily used for sputtering the real pressure a factor 1.4 larger than the indicated value. The pressures reported in this thesis are uncorrected values. This is an indirect measurement via the properties of the gas the cross section of the gauge is depicted below in figure 17.

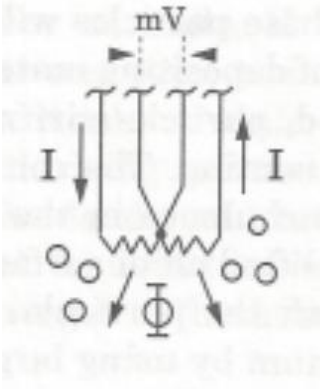

Figure 17. Thermocouple gauge Schematic. [18]

The wire presented in the figure heats up from the constant current I. This increase of temperature is measured with a thermocouple as a voltage within the range of mV. In the molecular flow regime, the heat of the wires is removed from background gas which is subjected by the heat-transfer coefficient, h_c. As the heat-transfer coefficient is proportional to the pressure this concludes that if the temperature of the wire drops then the pressure has increased. The heat-transfer coefficient is defined with the relationship of the heat flux equation which is expressed below.

$$\Phi = h_c(T_h - T_s) \tag{3.6}$$

The heat flux Φ is related to the difference of temperature between the wire T_h and the vacuum system T_s. In the fluid flow regime this equation changes due to the increased pressure and so the bulk thermal conductivity K_T governs and is independent of the pressure. The following equation expresses this relationship.

$$\Phi = -K_T \frac{dT}{dx} = \frac{K_T}{b}(T_h - T_s) \tag{3.7}$$

At high pressure the above equation governs, and b is the gap between the two plates (i.e. filament and vacuum system) and K_T is the thermal conductivity.

The hot ionization gauge is dependable in the high vacuum range but not for sputtering and must be turned off during deposition. The construction of this gauge consists of a filament, a cylindrical grid, and an ion collector which is depicted below in figure 18.

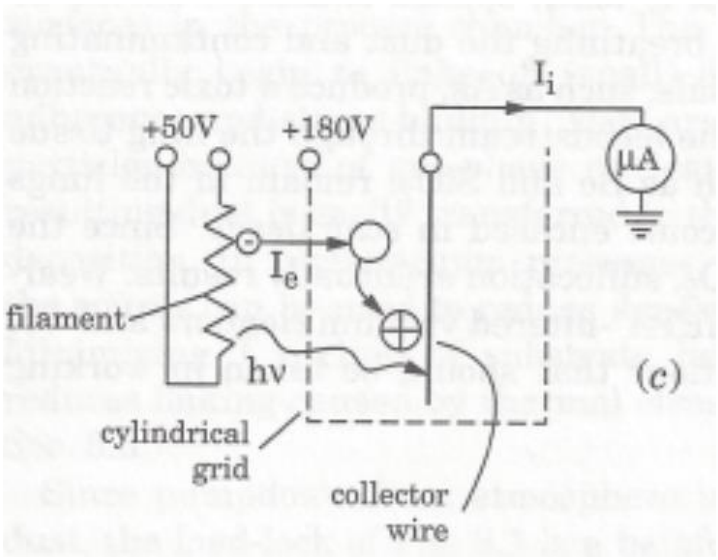

Figure 18. Hot Ionization Gauge Schematic[18]

The heated filament uses ejected electrons that are collected by the cylindrical grid that creates a positive potential. The ejected electrons create a plasma by ionizing the gas and the density of the plasma depends on the gas present in the chamber. The pressure is proportional to the density of the plasma. The lower pressure limit is determined by the flux shown as (hυ) in figure 18 these are high energy photons irradiating from the collector wire from the filament. This limit is called the x-ray limit.

The control over the sputtering gas comes from two types of mass flow controllers MKS Type M100B/M10MB Mass Flo. The basic principle of these controllers is a thermal process and the schematic is depicted below in figure 19.

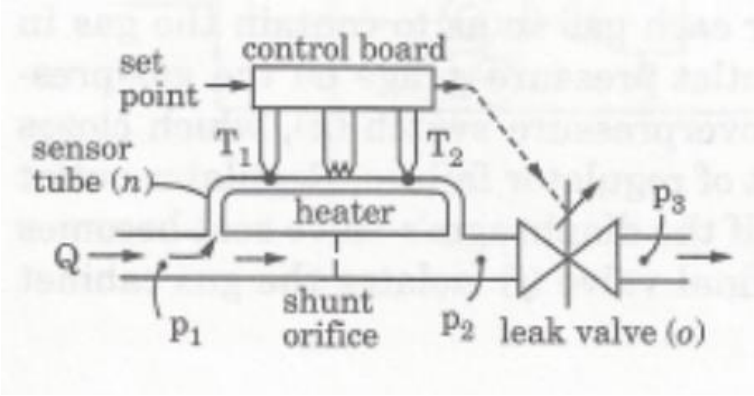

Figure 19. Thermal mass flow controller cross section. [18]

Definition of variables are as follows, T_1 and T_2 are temperatures, P_1, P_2 and P_3 are pressures, and Q is the mass flow rate. The diagram above shows a non-intrusive schematic due to the heating element along with the temperature sensors are not in the path of the gas. The sensor tube and the leak valve work via feedback loop to achieve the set point gas flow. The sensor tube has a limited range of gas flow that it can handle and so the shunt orifice accommodates any excess. The shunt orifice defines the total amount of flow the controller supplies and can be changed via substituting different orifices. The basic equation that governs this control unit is the following.

$$T_2 - T_1 = Bc_pQ \tag{3.8}$$

The temperature imbalance occurs because of the two paths in which the gas flows. The path near the heater increases the temperature of the gas and then carried downstream and deposited back into the main flow tube. On the right side of the above equation B is the constant of proportionality and Q is the mass molar flow rate with c_p being the heat capacity. The Argon the mass flow controller has a range from 0-100 sccm and the Oxygen mass flow monitor has a range of 0-20sccm. The error in the flow rate is approximate 1% of the full flow range. For the deposition of the oxide films the total

flow of gas was kept at 50 sccm. Films were sputtered at high oxygen flow and low oxygen flow.

To measure the sputter rate and film thickness a MODEL TM-350/400 quartz crystal monitor was used. The following figure 20 shows the general design of the cross section for a crystal monitor.

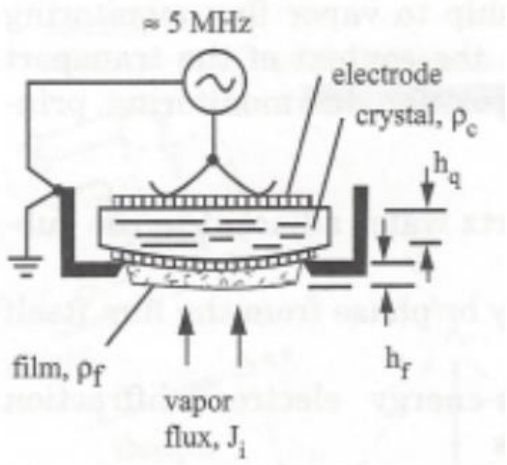

Figure 20. Crystal Quartz Monitor Schematic[18]

Defining the variables within the figure gives the following concepts, J_i is the vapor flux, h_q is the thickness of the crystal, h_f is the thickness of the deposited material, ρ_f is the mass density of the deposit (g/cm^3), ρ_c is the density of the crystal (g/cm^3). The most powerful tool for measuring the deposition rate is the vibrating quartz crystal mass-deposition monitor in the thin film industry. This monitor uses the resonant frequency of the crystal to generate an oscillating voltage. When a mechanical stress is applied to the crystal material a voltage is produced and so this material is said to be piezoelectric. If this mechanical stress was to oscillate the produced voltage would also oscillate. This

voltage could be amplified and fed back into the ac power source which would drive the crystal material at the resonant frequency. The ac power source is connected via sputtered electrodes connected to the crystal material. The bottom electrode is exposed to the deposition material which reduces the crystal's resonant frequency, v_r. This reduction is how the deposition rate is calculated from the measured change in frequency or beat frequency. The beat frequency can be measured to a few hertz due to the resonant frequency being very stable. The mass spring oscillator is the model used for this system which is crude but effective. The following concept is mathematical define as:

$$v_r = \frac{1}{T_v} = \frac{1}{2\pi}\sqrt{\frac{k}{m}} \tag{3.9}$$

The resonant frequency is expressed as v_r (Hz), the vibrational period is T_v (s), spring constant is k (N/m), and the mass of the spring m (kg). For a mass loaded crystal, the concepts are described as the following.

$$T_v = T_{vo} + \Delta T_v$$

Where (3.10)

$$\Delta T_v \propto \rho_f h_f$$

With the assumption the mass of the deposit is much less than the mass of undeposited crystal. To correct for the change in k and m an acoustic impedance, z, is used for the crystal deposit combination. The acoustic impedance depends on the material being deposited. This measurement system gives an absolute of the mass flow and therefore an absolute of the flux of the deposited material. Using the cosine law [17] and the Knudsen equation [18] and if their assumptions (the flux is perpendicular to the

monitor, and the target is circular) are reasonable one can calculate the vapor pressure, p_v, of the evaporates.

The cosine law is the flux that determines the deposition rate and mathematical expressed as the following. Where Q has units of (mc/s) and is the total evaporation rate from a circular source. The area around the source is described as a circle with radius r_o which is defining the geometry of the projected evaporated material. The geometry changes for sputtering however this is still an expectable model.

$$J_{\perp} = J_o cos^4\theta = \frac{Q cos^4\theta}{\pi r_o^2} \tag{3.11}$$

The Knudsen Equation describe the molecular impingement flux and is expressed as the following. With p, M, and T having units of Pa, g, and K. This equation is valid in the vacuum and fluid regimes of an operating pressure p.

$$J_i \left(\frac{mc}{cm^2 \cdot s}\right) = 2.63 \times 10^{20} \frac{p}{\sqrt{MT}} \tag{3.12}$$

Since the crystal and substrate are at different positions relative to the target material the vapor flux ratio must be determined empirically or estimated. One can use the cosine effusion law but for this thesis this was not used. Said law must also be adapted to sputtering geometry. The crystal can also be affected from a heated substrate due to thermal energy increasing the vibrations. The crystal monitor can be maneuvered in and out of the way of the sputtering beam for measurements of the sputter rate during the pre-sputtering phase. The deposition rate is measured through a change in the oscillating frequency of the quartz crystal. The deposition rate depends on what material that is being sputtered. To monitor the deposition rate two quantities are needed, the density and the acoustic impedance of the material to be sputtered. Both need to be

entered in the control unit. The values used in this thesis for NiFeO, NiO, Pt, and for Au are presented in the following table.

Table 4. Quartz Crystal Monitor Parameters

Quartz Crystal Monitor	NiFeO	NiO	Pt	Au
Density (g/cm^{-3})	6.67	6.67	21.4	19.3
Acoustic Impedance (10^5 g/cm^2 s)	18.65	18.65	2.7	23.18

Substrates

Films were deposited on quartz substrates, glass microscope slides, and n-type and p-type Silicon. Information on the silicon wafers is provided in Table 5.

Table 5. Doping information of silicon wafers (100) orientation.

Wafer	Dopant	ρ [Ω.cm]	Thickn. [cm]
n-Si 1		0-100	
n-Si 2	Sb	0.07-0.09	.036-.04
p-Si		0-100	

The Si substrates were cleaned in a Hydrofluoric acid solution to strip the native oxide layer from the top and bottom of the n and p type silicon wafers. The HF process was performed by an EDC 650 Series Spin Processor that used a 50:1 (ml) acid solution and a 60 second exposure time. A picture of the instrument is depicted below in figure 21.

Figure 21. EDC 650 Series Spin Processor

The absence of the native oxide film was confirmed by the hydrophobic properties of the solution and no other method was used to analyze the removal. During the exposure partitive the substrate is not rotated and after 60 second a rotational speed of 3500 rpm's is achieved accompanied by water to rinse off the acid solution for two minutes.

During the HF cleaning some substrates had back contamination that was resolved from cleaning the system and reducing exposure to one cycle. The back contamination is illustrated in figure 22 below.

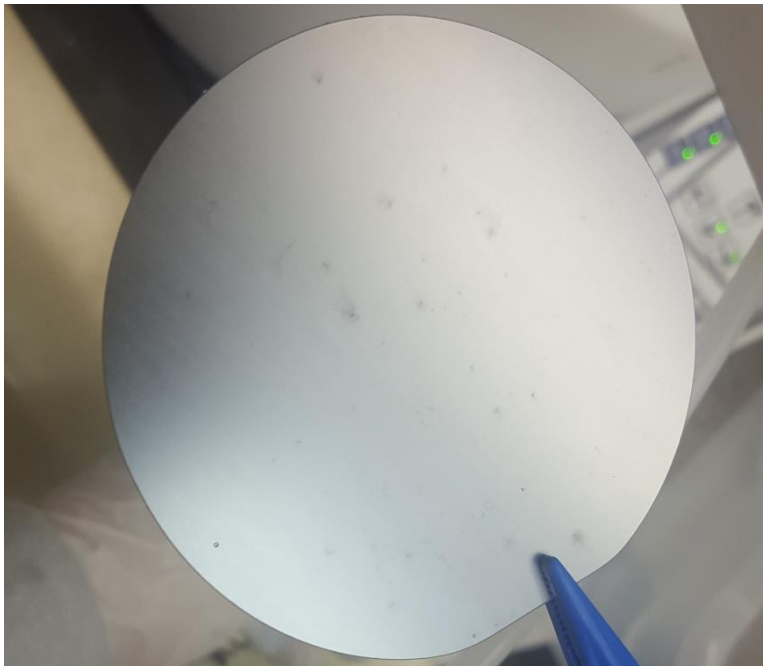

Figure 22. Back side contamination of silicon wafer after HF clean.

The quartz and glass-substrates go through a solvent cleaning process with the following sequence: water, acetone, methanol, and IPA. The IPA step is done on a Spinner (Model WS-400A-6NPP/LITE). Once the spinning process is complete the back of the quartz substrate is wiped using cleanroom tissue to remove any excess IPA. It was noticed that letting the IPA dry on the back of the mask-substrates results in contamination of the silicon substrates that gets in touch with the mask-substrates.
If the quartz substrates are not cleaned properly which means that IPA film is left on them a contamination can occur on the Au electrodes which is depicted in figure 23 below.

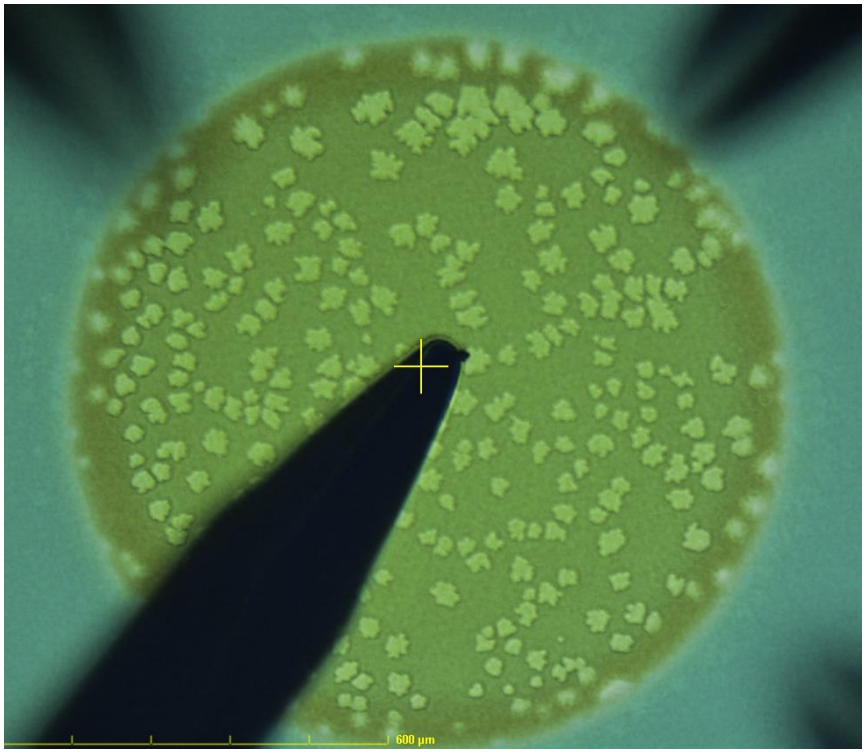

Figure 23. Au Electrode contamination.

Deposition

Deposition occurred using an AJA Orion 8 sputtering system with a base pressure in the 10^{-7} Torr range. Device wafers contained three different top films (i.e. Metal1/Oxide/Metal2) and an aluminum film on the back, promoting good contact for the electrical measurements.

Any metal deposition is sputtered at 5E-3 Torr with 30 sccm of Ar and a power of 150 Watts using a single DC magnetron sputter gun. With a 600 second deposition time this results in an approximate thickness of 100 nm which constitutes a sputter rate of 1.6 Å/sec. One inch quartz substrates and microscope slides are used as masks to block off sections for a certain process layer so that different film stacks are created on the same wafer including Si/metal/oxide/metal 2, Si/oxide/metal 2, and Si/metal 2. The oxide layer

is deposited using reactive RF magnetron sputtering. For good uniformity of the oxide layer, deposition was done at significant sputter pressure ($8x10^{-3}$ Torr), on a rotating substrate holder (50 rpm), using two guns positioned on opposite sides of the substrate holder. Using two guns creates a more homogeneous sputter flux. At high pressure the mean free path decreases and as a result a wider and more homogeneous sputter beam is achieved. Two different oxides were grown using Ni or $Ni_{80}Fe_{20}$ targets and two different oxygen flows yielding four combinations. The gas flow was held constant at 50 sccm into the system resulting in a pressure of around 8 mTorr. For high oxygen films 30 sccm Ar and 20 sccm of O_2 were used. For low oxygen films 45 sccm Ar and 5 sccm O_2 was used. Both guns were powered up to 200 watts with intervals of 30-40 on the tune and load. The sputtering time for the low concentration oxides were 600 or 1200 seconds which yielded an approximate thickness of 95 nm or 190 nm and a rate of 1.55 Å/sec. The sputtering time for the high oxygen flow samples was 1200 seconds resulting in an approximate film thickness of 23 nm which means a deposition rate of approximately 0.2 Å/sec.

A contact mask was made from alloy 42 sheet metal and contained 32 die's each with 41 circular devices varying in radius from 400 μm to 35 μm. The contact mask was used to fabricate the metal top contacts. The size of the electrodes was double checked with a Hirox optical microscope. Nominal device diameters were approximately 20-40 μm beyond the design dimensions. As the sheet metal mask had a thickness of 127 μm, the effect of shadowing by the mask was significant for the devices having a radius below 60 μm. Pictures of the designed contact mask, the realized contact mask, and a typical wafer manufactured with the mask are shown in the figure below. Note that the devices

were not isolated from each other and all shared the same oxide layer and same silicon wafer. The schematic for the shadow mask and a wafer after deposition is depicted in figure 24 below.

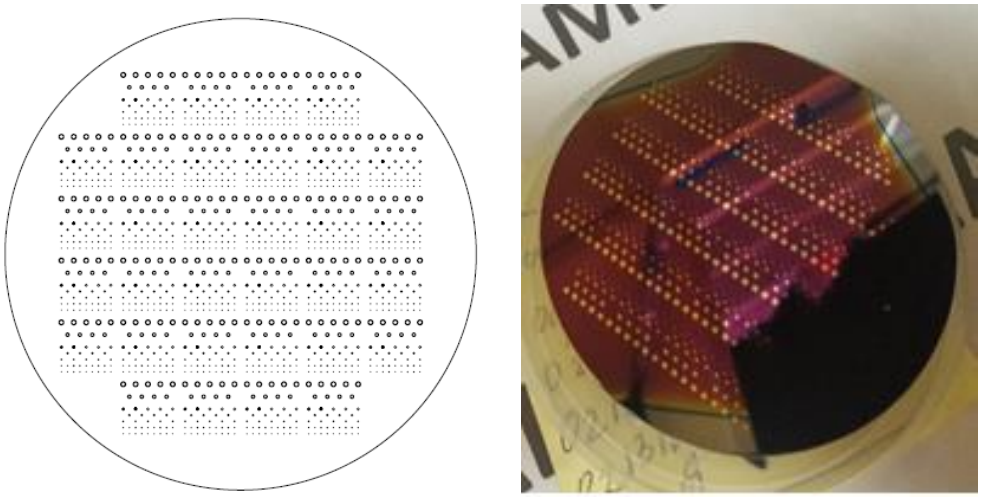

Figure 24. Test Wafer Schematic

IV. CHARACTERIZATION

Ellipsometer

The Ellipsometer technique, uses a polarized plane wave of light that is reflected off the interface of a thin film at some angle to determine the optical properties or the film thickness of the sample under study. The reflected wave's polarization is compared to the polarization of the incident beam and the change can be used to determine the film thickness and index of refraction of the sample. The Analysis Research Service Center (ARSC) provides a J.A. Woollam M-2000UI Automated Angle ESM-300 Base Ellipsometer model with a wavelength range of 245-1700 nm, so from the UV all the way into the Near Infrared Extended (NIR) range up to 1700 nm. These models use fast spectral detection to measure the ellipsometric quantities Δ and ψ at different wavelengths simultaneously.

The Ellipsometer measures the change of the state of polarization which is defined by the curve the electric field vector describes at a certain point in space as a function of time. Note that light is an electromagnetic wave consisting of an electric and magnetic wave that are oriented 90 degrees with respect to each other. As for the visible part of the spectrum only the electric field interacts with matter, for ellipsometry one often only considers the electric field when describing its polarization. Light is defined as linearly polarized wave that when the direction of the electric field vector does not change its orientation at a certain point in space. Elliptically polarized light can be considered the superposition of two linearly polarized waves: one horizontal linearly polarized plane wave and one vertical linearly polarized plane wave. The light is linearly polarized when their orthogonal components are in phase. When one component is phase

shifted by a factor of $\pi/2$ and so is out of phase with the other component, the light is circularly polarized: so, the electric field vector describes a circle as a function of time. Elliptical polarization has different magnitudes along with different phases for both components. Note that in isotropic media these directions are perpendicular to each other and perpendicular with the propagation of motion. This technique general monitors the change in the state of polarization. The incident beam is directed at the thin film and upon reflection a change in the polarization state may occur. The equations that govern the behavior of the reflected light are the Fresnel equations that depend on the orientation and relation of the electric field of EM-wave on both sides of a planar interface. Defining the geometry of the parallel (E_p) and perpendicular (E_s) components of the wave is depicted below in figure 25.

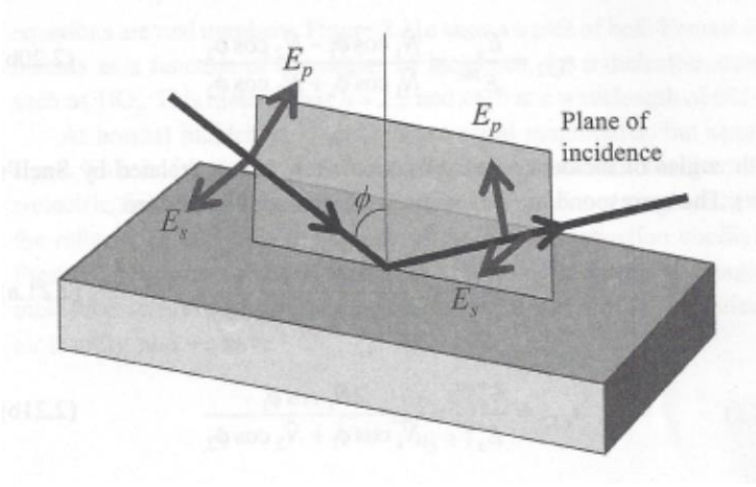

Figure 25. Components of Incident light. Parallel and perpendicular components of the incident and reflected electric fields. [20]

There are two Fresnel equations, that describe the reflected light. One for s-polarized light, if the electrics field is perpendicular to the plane of incidence which is

called transverse electric field (TE). The other Fresnel equation describes the reflection of p-polarized light and is called Transverse magnetic (TM) where the electric field is parallel to the plane of incident. Defining the geometry of this optical system is depicted below in figure 26.

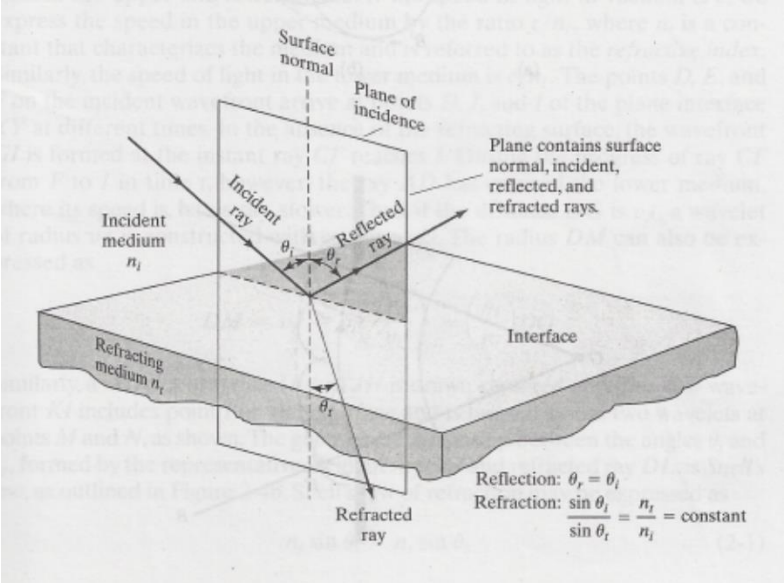

Figure 26. Incident and Reflected Waves on an Interface. [21]

Equation 4.1 introduces the Fresnel equations for a planar interface, i.e. the relationship between the electric field of the reflected beam and the electric field of the incident beam.

$$r_{TE} = \frac{E_r}{E_i} = \frac{n_1 cos\theta_i - n_2 cos\theta_t}{n_1 cos\theta_i + n_2 cos\theta_t} \tag{4.1}$$

$$r_{TM} = \frac{E_r}{E_i} = \frac{n_2 cos\theta_i - n_1 cos\theta_t}{n_2 cos\theta_i + n_1 cos\theta_t}$$

The variables in equation 4.1 are defined as r_{TM} and r_{TE} and are referred to as the Fresnel Reflection Coefficients, n_1 is the complex index of reflection of the ambient material, n_2 is the complex index of reflection of refraction material under study, θ_i is the angle of incidence, and θ_t is the angle of refraction. The complex refraction index (n) is a measure of the velocity of a wave propagating through a material and how much of the wave is absorbed. The refraction index is a complex number and therefore has a real part which describes the speed of the wave and the imaginary part describes the absorption of the wave. The imaginary part is called the extinction coefficient. Snell's law describes the relationship between the angle of incidence and the angle of refraction. The following equation is Snell's law or the law of refraction and describes the relation between the angle of incidence θ_i and the angle of refraction θ_t:

$$n_1 sin\theta_i = n_2 sin\theta_t \tag{4.2}$$

When the electromagnetic wave undergoes a reflection of a planar interface, the phase between the TE and TM component and the relative ratio of the amplitudes of the TE and TM components of the light change. This results in a change of the polarization and is described by the ratio of the two Fresnel reflection coefficients. The ratio of the Fresnel reflection coefficients has two terms the amplitude ratio $\tan(\psi)$ and the phase shift difference between the p and s components Δ. The ratio is described in the complex ellipsometric quantity ρ.

$$\rho = \frac{r_{TE}}{r_{TM}} = \tan(\psi) e^{i\Delta} \tag{4.3}$$

Since the ratio is measurable there is no need to perform absolute intensity and phase measurements. The angles ψ and Δ are determined by the sample's optical properties and the angle of incidence. For a multiple thin film stack the equations become

more complicated due to the many interfaces and materials. The information that one can deduct from the ellipsometric measurement data are many including, optical properties, film thickness and, surface roughness. Theoretically a limit does not exist for the measurability of a film's thickness. A model is used to determine the film thickness and assumes uniform optical properties and a sharp planar film-substrate boundary. Maxwell's equations at the macroscopic level are the foundations of the ellipsometric equations and may not apply to layers that are below 1nm. As for very thick films the optical path lengths increases and may have some interferences between the reflected interface beams. The cyclic nature of thickness measurements is caused by the interference, and for non-absorbing films ψ and Δ are cyclic functions. After one full cycle they repeat and is described in equation 4.4.

$$d = \frac{\Lambda}{2\sqrt{n_1^2 - sin^2(\Phi)}} \qquad (4.4)[22]$$

Where d is the thickness of the film, Λ is the wavelength of the incident light, n_1 is the index of refraction for the film, and Φ is the angle of refraction. The films fabricated for this thesis are a two-interface stack and the following equations govern the total Fresnel reflection coefficients:

$$r_{TE} = \frac{r_{TE,12} + r_{TE,23}e^{-i2\beta}}{1 + r_{TE,12}r_{TE,23}e^{-i2\beta}} \qquad (4.5)$$

$$r_{TM} = \frac{r_{TM,12} + r_{TM,23}e^{-i2\beta}}{1 + r_{TM,12}r_{TM,23}e^{-i2\beta}}$$

Where

$$\beta = 2\pi(\frac{d}{\lambda})n_2 cos\Phi_2 \quad (4.6)$$

Depicting the geometry for equation 4.6 is in the following figure 27.

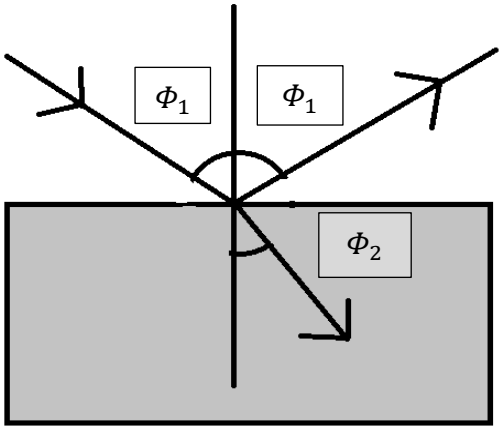

Figure 27. Relationship between the angles of Incident ray and refracted ray.

The variables for equations 4.5 are defined as: $r_{TE,12}$ and $r_{TM,12}$ are the Fresnel reflection coefficients for the interface of the air and thin film and $r_{TE,23}$ and $r_{TM,23}$ the Fresnel reflection coefficients for the film-substrate interface. Equation 4.6 is the phase change as the wave moves from the top interface to the bottom interface. As the wave traverses the film twice the β is then multiplied by 2 in equations 4.5 to account for both phase shifts.

Scanning Electron Microscope (SEM)

Provided to researchers by the ARSC is the FEI Helios Nano Lab 400 Scanning Electron Microscope. Images are obtained from samples using an electron beam for the observation of the morphology and chemical composition. The electron beam originates from an electron gun stationed at the pinnacle of the chamber. A scanning electron

microscope is comprised of an electron gun, a lens system, scanning coils, an electron collector, and a cathode ray display tube (CRT). Thermionic emission is the concept that governs the creation of the electron beam. A metallic wire filament, such as Tungsten or Tantalum, has a driven electrical current which heats up the material due to collisions. Coulomb repulsion causes electrons to diffuse from the source filament. If an accelerator structure is used the electrons emitted from the filament can be brought into focus in an electron beam path. These accelerator structure possess either diode geometries of two or three electrodes. The lens system is mostly comprised of magnetic fields that condense the beam much like what is shown in the figure 28 below.

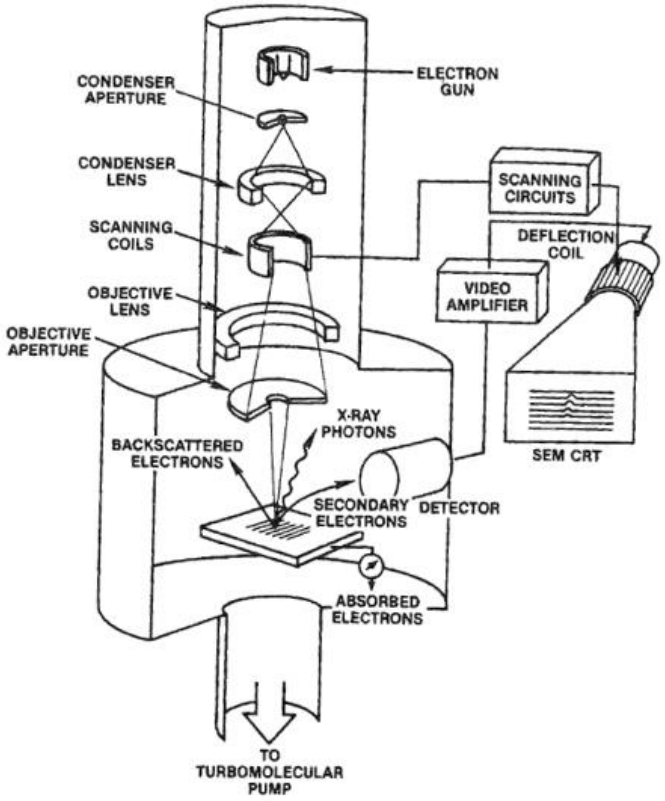

Figure 28. Scanning Electron Microscope (SEM) Schematic. [22]

The ARSC SEM is furnished with a field emission electron beam source. Instead of a filament that heats up, an electric field of sufficient strength is used to emit electrons from the material using the concept of tunneling. Two CRT's are typically used within SEMs that have either large viewing area or a high-resolution for photography. Magnification M results from the mapping process according to the ratio of the dimension scanned on the CRT to the dimension of the scanned sample. Magnification (M) depends on the ratio of the dimensions between the CRT and the sample, equation 4.6 below shows the relationship.

$$M = \frac{Length\ of\ CRT\ Display}{Length\ of\ sample\ scanned} \tag{4.7}$$

As the electron beam is focused and scanned across the surface of the sample secondary and back scattered electrons can be monitored as well as the generated X-rays. The information depth of the scanned image depends on electron penetration depth. The latter is defined as the average distance from the surface of the sample along the trajectory. Equation 4.7 shows how the penetration depth (R_e) depends on the sample's density and electron beam energy.

$$R_e = \frac{4.28 \times 10^{-6} E^{1.75}}{\rho}\ (cm) \tag{4.8}$$

Where ρ is the sample density (g/cm^3) and E is the energy of the electron beam in keV. The figure 29 below shows the information depth for different type of electrons.

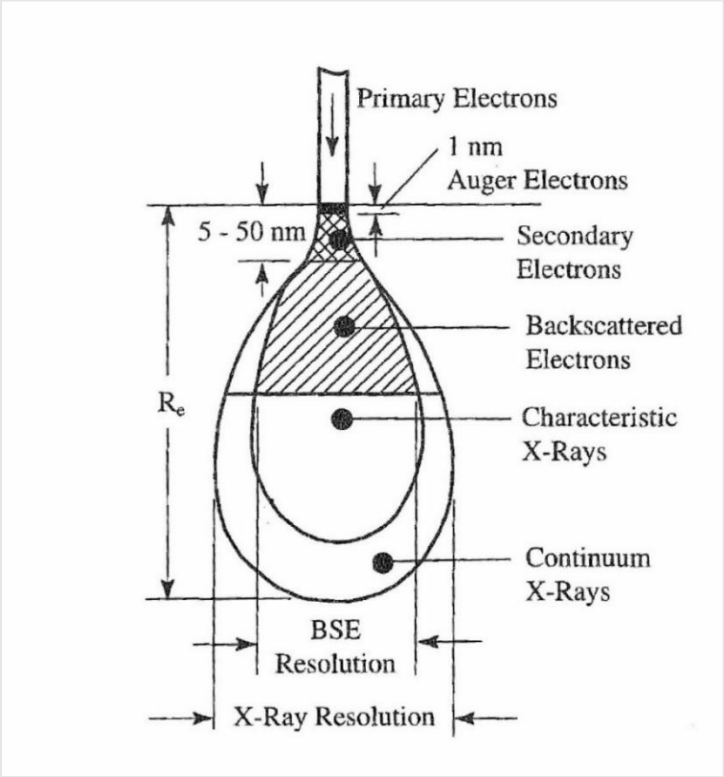

Figure 29. Electron Depth Profile. [22]

Secondary electrons are the most common imaging mode since very little energy is needed to excite these charges. Since the excitation energy is so low these charge carries originate from the subsurface depth which is not bigger than a few angstroms. The secondary electrons are captured by a combination of a scintillator/photomultiplier and the output modulates the intensity of a CRT. Backscattered electrons possess similar energies of the incident electrons and so are defined as high energy charges that are scattered by elastic collisions. As the atomic number increases so does the probability of backscattering. With the highest energy incident electron beam X-rays are generated and emitted. This will allow for the determination of atoms present in the sample. This technique is referred to as X-ray energy dispersive analysis (EDX). The concentration of atoms in the sample can be identified within a couple of percentages.

Optical Microscope

In order to measure the shadowing effects from the deposition mask a Hirox RH-2000 Digital Microscope was used. The images were taken with an MXB-2500REZ Zoom Lens with magnification of 35-2500x connected to a CMOS camera with a visual pixel resolution of 1200 x 1920. The lens and camera are connected via a camera bayonet mount and connected to a motorized z stage for automated zooming. The sample rests upon a motorized x-y stage for automated control using a remote-control device. All photos presented in this thesis were taken in bright field mode. In bright field mode, the light collides perpendicular to the sample. Horizontal surfaces reflect the majority of the light, and hardly any reflection comes from slanted or vertical surfaces. In 1834 the English scientist Airy, showed that for diffraction at a circular aperture of diameter d, the angular position of the first minimum is given by the following equation:

$$\sin(\alpha) = \frac{1.22\lambda}{d} \tag{4.9}$$

Where ʎ is the wavelength of light in free space. Where the light is concentrated is called the Airy or diffraction disc. For two dimensional objects Raleigh suggested the central maximum of a wave coincides with the first minimum of the other. The intensity between the two peaks decreases the peak height, the equation following defines:

$$s = \frac{0.61\lambda}{nsin(\theta)} = \frac{0.61\lambda}{NA} \tag{4.10}$$

This equation defines resolution, where n is the refractive index of the medium between the objective and the object and at the object, θ is the half angle subtended by the lens. The numerical aperture (NA), usually inscribed on the mount of the objective, is a unitless quantity that expresses the brightness of the image it forms and the resolving

power of the lens. The quality of the lens is directly proportional to the NA. For higher resolution the inverse relationship of NA and s requires a small s and a large NA. However, NA relies on the resolution, and the shallow depth and working distance the distance from the focus point to the surface of the objective. The upper limit for the numerical aperture is 0.95. Beyond the limit, higher resolution is achieved by using immersion objectives in which a median with a higher index of refraction is placed in the path of the light beam between the lens and the sample. A picture of the instrument used is presented in figure 30.

Figure 30. Hirox RH-2000 Digital Microscope. [23]

The software of the microscope, the RH-2000 was used to measure the diameter of the electrical contacts on the produced device wafers. This program allows for full access to the instrument such as the motorized capabilities, the capturing of z-stacks, and also allows to measure distances from the captured images as long as and the zoom ring is centered and the magnification ring is set to one of the calibrated values.

Linear Four Point Probe

To measure high resistivity samples a linear four-point probe (4pp) was used on the oxide's samples fabricated for this thesis. Resistivity effects device series resistance, and thus measured capacitance, threshold voltage. and therefore, is important to quantify. The resistivity (ρ) depends on the free electron and hole densities and their mobilities (n and p, u_n and u_p):

$$\rho = \frac{1}{q(nu_n + pu_p)} \tag{4.11}$$

This instrument consists of four electrodes positioned in a line each separated by an approximate distance of 0.1 inch. All four electrodes are connected to a switching matrix which is also connected to a current source, a current amp meter and a nano-voltmeter. Using the switching unit, the current source is connected to two electrodes and the nanovoltmeter to the other two electrodes, and then a measurement is performed, i.e. the sourced current is checked with the ammeter and the voltage over the other two contacts measured with the nanovoltmeter. The use of a switching matrix allows for different combinations of measurements and therefore a higher measurement accuracy. The effect of temperature differences across the sample and offsets of the nanovoltmeter and current source can be canceled out by averaging the V/I of different electrode configurations. The use of a 4pp removes the contact resistance from the measured resistance values, so the measured V/I is only due to the sample's resistivity and does not depend on the size and material of the electrodes. Voltmeters have a very large resistances to ensure negligible current influence. It is important that the resistance of the voltmeter is at least a factor 10 larger than the resistance of the sample to avoid shunting

of the sample by the voltmeter. Thin NiFeO samples that are sputtered at intermediate oxygen pressure will have a larger resistance than the resistance of the nanovoltmeter in the linear 4pp setup. For those samples the switching unit is set to high resistance mode. This places high input resistance buffer amplifiers between the sample and the nanovoltmeter. The input resistance of those buffer amplifiers is 10^{14} Ohm, so the used linear 4pp can measure samples up to at least 10^{13} Ohm. Sheet resistance R_s (ohms/square) is calculated from the measured IV using the following equation:

$$R_s = \frac{\pi V}{\ln(2) I} \tag{4.12}$$

Where $\frac{\pi}{\ln(2)} = 4.53$. The relationship between resistivity and sheet resistance is defined by the following expression.

$$\rho = 4.532 t R_s \tag{4.13}$$

Where t is the thickness of the film. The instrument includes a Keithley-6514 electrometer, a keithley-2182 nanovoltmeter, a Keithley-7001 switching box (Keithley-7065 Hall Card), and a Keithley-6221 current source.

Summit 12000 Probe Station

Electrical characterization on the device wafers was carried out using a B1500A Semiconductor Parameter Analyzer connected to a Summit 12000 Probe Station also provided by the ARSC. IV and CV characterization is available through this system. The accuracy for current measurements has a range of 0.1fA – 1A and for voltage ranges 0.5μV – 200V. Options for spot and sweep measurements are available as well as time sampling measurements. Multi-frequency AC impedance measurement ranges from 1kHz

to 5MHz and a Quasi-Static Capacitance-Voltage measurement with leakage current compensation is available.

The software used for the B1500A is called EasyEXPERT and is equipped with pre-configured test definitions. These pre-configured tests can measure a wide range of devices such as: nanotechnology, power devices, solar cells, MOS devices, pn junctions, and organic devices. While using these pre-configured tests a circuit model is displayed on the screen which clarifies which micro positioners are in use.

The Summit 12000 Probe Station is equipped with a platen lift lever, micro positioners, top hat, motorized x-y-z stage, and microscope. The x-y-z stage is within a chamber with purge capabilities so measurements can be performed below or above room temperature without damaging the sample. Within the chamber the temperature can be adjusted from -60 ^{o}C to 300 ^{o}C using the Chiller C60. When the chiller is active a flow of nitrogen gas is introduced into the chamber so that water cannot condense on the sample. The chuck is connected to a vacuum pump and when the sample makes contact the pressure underneath the sample is reduced. This reduction of pressure keeps the sample at the same position on the chuck during motions of the x-y table. It also improves the contact between the back of the wafer and the chuck. The micro positioners are the electrical contacts that supply power and measure electrical quantities.

The Velox program runs the Summit 12000 and is equipped with quite a lot of features. One of the most usually programs used for this thesis is the wafer map option. This allows the user to program the location of the electrical contacts so that the chuck can move to each device automatically. The wafers used have each 1312 devices and with this program the user can almost instantaneously move the electrodes from one

device to another. This feature when used with the Easy Expert program allows for measurements on a large number of devices in a relative short time frame.

V. MEASUREMENT RESULTS

Current-Voltage Relationship Results

The perpendicular and the parallel resistivity of the oxide films were measured for this thesis. For high oxygen flows NiFeO films there was a factor 1.75 difference between the perpendicular and parallel resistivities. For NiO low oxygen flow samples a factor 20 difference between the parallel and perpendicular resistivities was observed. Table 6 summarizes specific measurement values.

Table 6. Parallel and Perpendicular Resistivities.

Sample id	Material	Thickn. [nm]	% O_2 in gas [%]	ρ // [Ω.cm]	ρ_p [Ω.cm]
052818-04	$Ni_{0.8}Fe_{0.2}O$-low	91 ± 2	10	4.1E5 ± 0.5E5	
052818-02	$Ni_{0.8}Fe_{0.2}O$-high	16 ± 2	40	1.3E4 ± 0.3E4	
041519	$Ni_{0.9}Fe_{0.1}O$-high	22.7	40	0.8E3 ± 0.2E3	1.4E3 ± 0.3E3
051718-03	NiO-low	196 ± 19	10	1E4 ± 0.3E4	4.9E2 ± 1.0E2
052118-01	NiO-high	17 ± 2	40	3.3E2 ± 0.6E2	

The specific contact resistivity was estimated from the difference between the 2pp measurements on metal-oxide-metal devices and the 4pp measurements on the quartz shadow masks. The equation used to determine the contact resistivities is as follows:

$$\mathbf{r_{NiFeO-Pt}} = \frac{\mathbf{A(R_{2pp}-2R_{probe})-\rho_{NiFeO}t}}{\mathbf{2}} = \frac{\mathbf{A(R_{2pp}-2R_{probe})-\rho_{4pp}t}}{\mathbf{2}} \qquad (5.1)$$

Where A is the cross sectional area of the device measured with the 2pp technique (i.e. Summit 12000 probe Station), t is the film thickness of the oxide, R_{2pp} is the resistance of the device measured by the 2pp technique, and ρ_{4pp} is the resistivity determined by linear 4pp on the oxide film on top of the quartz shadow mask. The 2pp IV characteristic of metal-oxide-metal devices is linear as shown in figure 31 below. These measurement results

include the bulk resistance of NiFeO ($\frac{\rho_{NiFeO}t}{A}$), the contact resistance between the metal electrodes and the NiFeO ($2\frac{r_{NiFeO-Pt}}{A}$), and the contact resistance of the probes with the top electrodes ($2R_{probe}$). The total 2pp resistance is given by the following expression:

$$\mathbf{R_{2pp} = \frac{\rho_{NiFeO}t}{A} + 2\frac{r_{NiFeO-Pt}}{A} + 2R_{probe} \approx \frac{\rho_{NiFeO}t}{A} + 2\frac{r_{NiFeO-Pt}}{A}} \qquad (5.2)$$

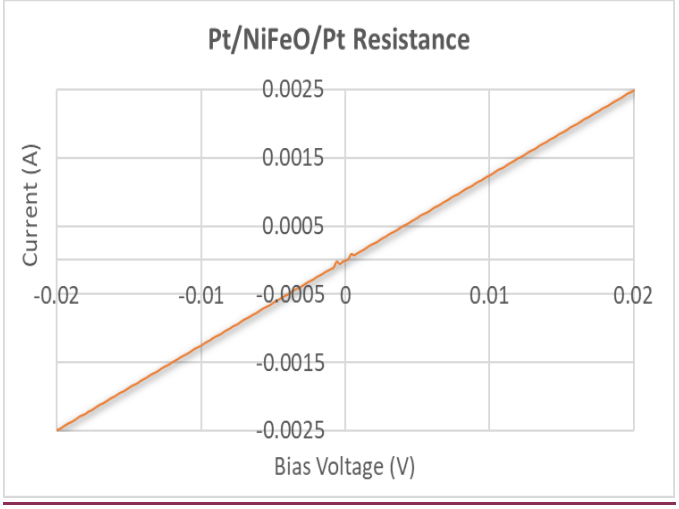

Figure 31. IV characteristic of Pt/$Ni_{0.8}Fe_{0.2}O_1$/Pt devices sputtered at high oxygen flow.

Others have shown that the IV relation of low oxygen concentration NiO sandwiched between conducting electrodes can be modified from a high resistance state to a low resistance state. Such switching makes the oxide interesting for application in non-volatile RRAM devices. The typical resistance ratio of the high and low resistive states for NiO RRAM devices is several orders of magnitude as shown in figure 32 [24]. The switching between the two states causes the IV relation of the oxide to show hysteresis. In addition, the IV characteristic of the material is typically non-linear.

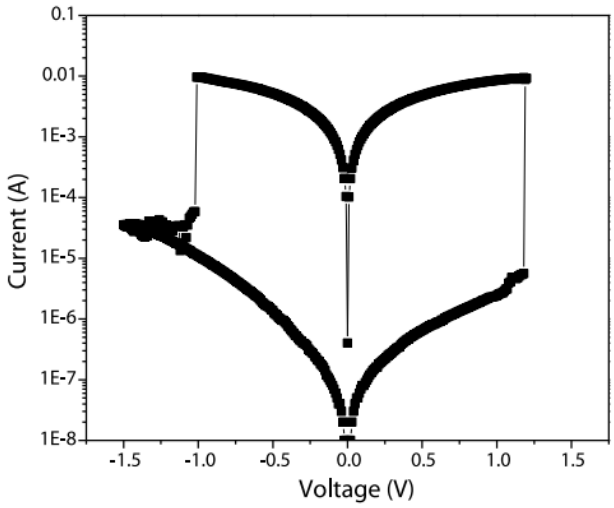

Figure 32. Bipolar resistive switching property Co/NiO/Pt device. [24]

In this section the results of IV measurements performed on the manufactured device wafers described in chapter 4 are reported. The wafers were named by the date of fabrication. The devices were categorized with the following code #die.#device radius.#Series (i.e. 22.400.0). The two-point probe measurements were made between a single wire conventional probe directly placed on the top electrode and the chuck from the Summit 12000 wafer prober and the B1500A Keysight semiconductor device analyzer. All voltage current relationship modeling is an approximation based on preliminary observations. The following figure 33 shows a basic representation of such wire convention.

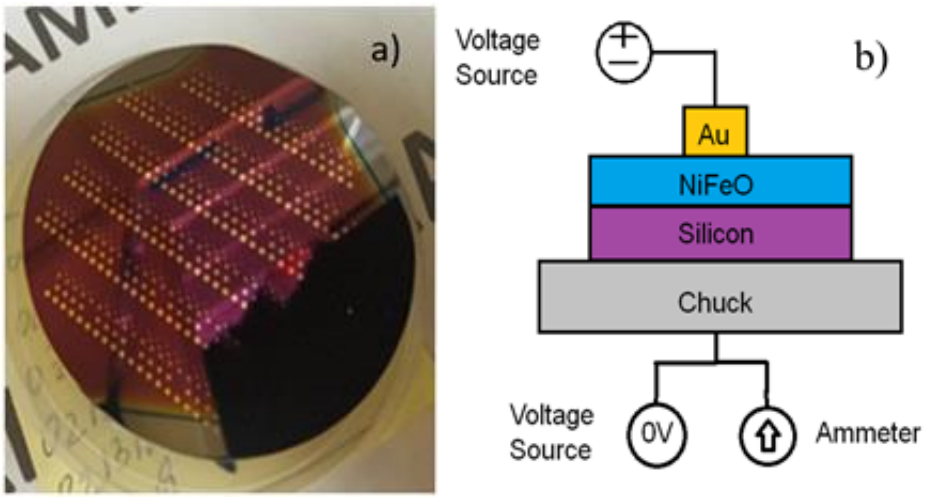

Figure 33. (a) Two-point-probe contact wafer; (b) electric measurement configuration

Several tests were performed to find any systematic errors. Landing the probes twice at the same location reduces the series contact resistance between probe and top electrode below 5 Ω for Au and below 1.7 Ω for Pt top electrodes. This resistance is too small to significantly affect the IV curves. To measure the effect of the back contact of the wafer two additional experiments were performed: (1) Measurements were performed on wafers with and without aluminum back-constant layer. Similar results were obtained from both type of measurements; (2) Measurements between two top contacts on an insulating chuck were performed. They show an IV curve that is consistent with two opposite biased devices in series. Both experiments indicate that the aluminum back contact has no significant influence on the IV properties of the wafers presented in this section.

A current compliance of 3mA was used because it was observed that at currents in excess of 10 mA damage to the device occurred. The thin films delaminated from the substrate at higher currents due to the formation of a gas between the oxide and the

electrode. As the bubbles destroyed the device, the maximum current was limited. This is depicted in figure 34 below.

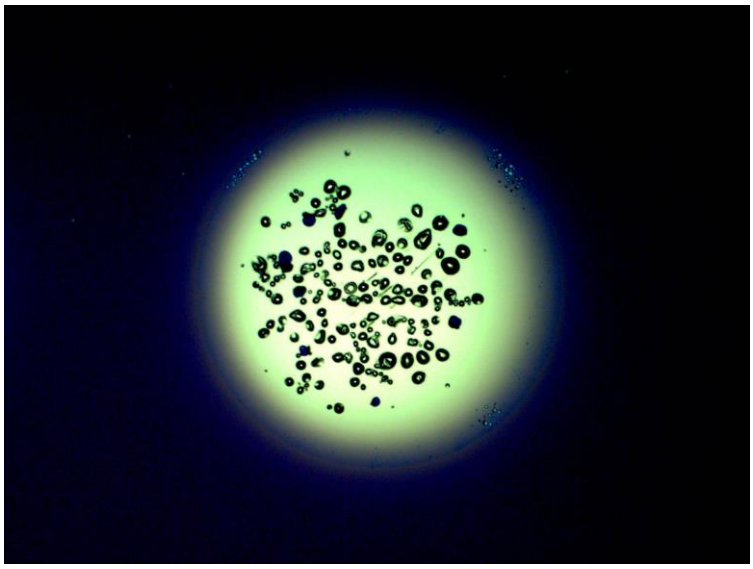

Figure 34. Au electrode blown up device.

Rectifying properties were observed for NiFeO with a low oxygen flow of about 5 sccm when grown on n type silicon substrates. The rectifying ratio ($I_{reverse}/I_{forward}$) is about 82. The test was conducted from 4 V to -4 V and swept back from -4 V to 4 V. During the sweep from -4 V to 4 V the resistance decreased allowing the hysteresis to form. The maximum decrease in the resistance of the sample at zero bias was about a factor of 8. The forward bias IV characteristics is linear from 1V to 4V with a resistance of 1.3 MΩ for figure 35. The current is proportional to V^2 from -0.8V to -4V in reverse bias and similarly from -4V to -0.8V. These relationships agree with space charge limited current (SCLC) which is considered due to bulk effects and the oxygen vacancies. No delay or hold measurement time was implemented during this device testing. The number of steps taken from 4 to -4 was about 101 steps in increments of 0.08 volts. The graph below

demonstrates the observation described above. As can be seen in the figure below the IV curve shows strong rectifying properties and hysteresis.

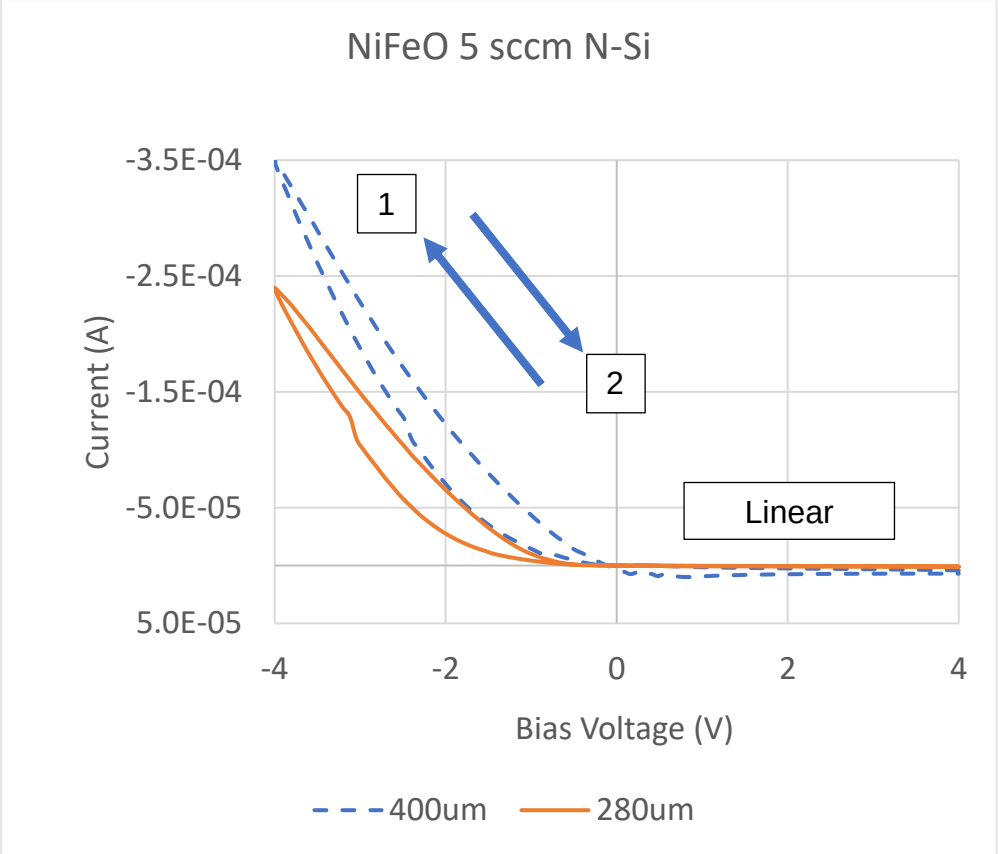

Figure 35. IV curves Au-NiFeO-Si devices: $Ni_{0.8}Fe_{0.2}O_{1-\alpha}$/n-Si. Wafer name 52618-01. Device code 22.400.1 and 22.280.1.

According to literature the above pattern resembles a resistive switching device although the mechanisms that drives this behavior is a complicated topic that has been debated for years. A typically resistive switching device has an oxide sandwiched between two metal electrodes which creates an IV behavior such like the following shown in figure 36 [10].

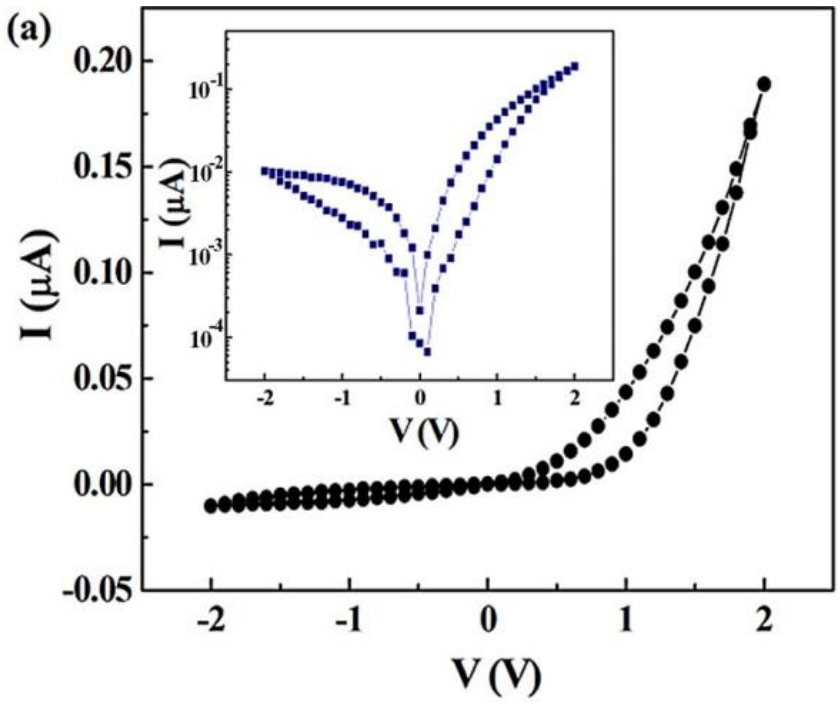

Figure 36. IV Curve on Au/α-Fe2O3/FTO. A Type 1 Resistive Switching Model related to interface effects. Au/α-Fe2O3/FTO (Fluorine-doped SnO2 conducting glass substrate).[25]

The behavior in figure 36 is similar to the behavior measured on the wafers deposited at low oxygen flow reported on in this thesis. A type 1 RS mechanism depends on the oxygen vacancies modulating the Schottky barrier height and width[26][27]. The small change in resistance could be oxygen vacancies that escape the trap sites at the interface and move along the grain boundaries before electroforming occurs[25]. By replacing the bottom electrode with a semiconductor an extra electrical characteristic shows up which is the rectifying properties. Similar rectifying ratios between figure 35 and 36. However, forward bias for α-Fe_2O_3 is the reverse bias of NiFeO. This could be due to the p n junction between p type NiFeO and n type silicon wafer. Note the similarities between the NiFeO device of Figure 35 and the data on the α-Fe_2O_3 devices in figure 36.

Exponents from 1-3 from a log-log graphs were observed by analyzing the data of figure 35[25]. This behavior is characterized as a Type 1 Resistive Switching Model[25] which is defined as a bipolar switching mechanism. The rectifying and hysteresis characteristics indicate a feature of a Schottky junction, and the hysteresis is evidence of resistive switching behavior. As in figures 35 no current jump as shown in figure 32 is observed the resistive switching mechanism observed here might be due to the Schottky barrier effect. Models that depend on the Schottky barrier effect are defined as a Type 1 RS Model[25]. Two mechanisms could possible explain the behaviors observed in the data. The Schottky mechanism depends on the metal insulator interface and whether the applied electric fields decrease the barrier height[28]. This concept is expressed as the following[28]:

$$I \propto T^2 \exp\left[\frac{q\sqrt{qV/(4\pi\varepsilon_i\varepsilon_0 L)}}{k}T\right] \tag{5.3}$$

The space charge limited current (SCLC) depends on current injection into the insulator. When a positive bias voltage is applied to the electrode the velocity of the injected electrons is greater than the drifting insulator electrons and therefore accumulate at the metal insulator interface. Once accumulation begins a space charge region is formed and if the applied voltage becomes sufficiently high the resistance increases due to the space charge electrons repelling incoming electrons. This repulsion could cause nonlinear conduction and negative resistance. Charging of traps due to defects can play a role and the current voltage relation could be described with the following expression.

$$J = \frac{9}{8}\varepsilon_i\varepsilon_0\mu\theta\frac{V^2}{L^3} \tag{5.4}$$

Here J is the current density (A/m^2) and ε_i and ε_0 are the dielectric constant of the semiconductor and the permittivity of free space, μ is the carrier mobility, V is the applied voltage, and L is the thickness of the oxide, θ is related to the trap density ($\theta=n/n_t$) [29]. The traps in the insulating material can be positioned either above or below the fermi level which would be defined as either a shallow or deep trap. Figure 37 shows the band diagram in the case of electron injection near the conductor/insulating interface. Not all of the injected charge carriers will contribute to charge transport as some will end up in the shallow traps (E_{tn1}).

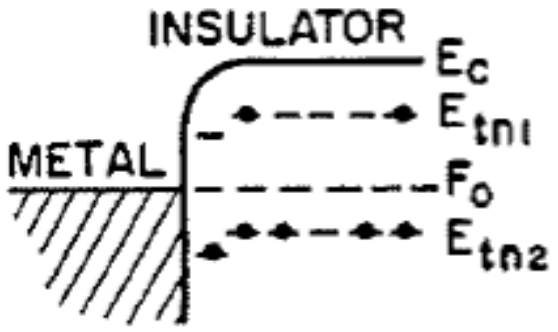

Figure 37. Electron traps positioned relative to the fermi level. Shallow trap exist above the fermi level while deep traps exist below.[29]

Figure 38 shows the current voltage relationship for the power square law or Child's Law. At small voltages the charge is transported by the free charge carriers in the NiFeO available from the natural doping i.e. the metal vacancies in the oxide (n_o). For these voltages the IV-curve is linear and the slope on a log-log curve is 1. The IV-curve is described for this regime by:

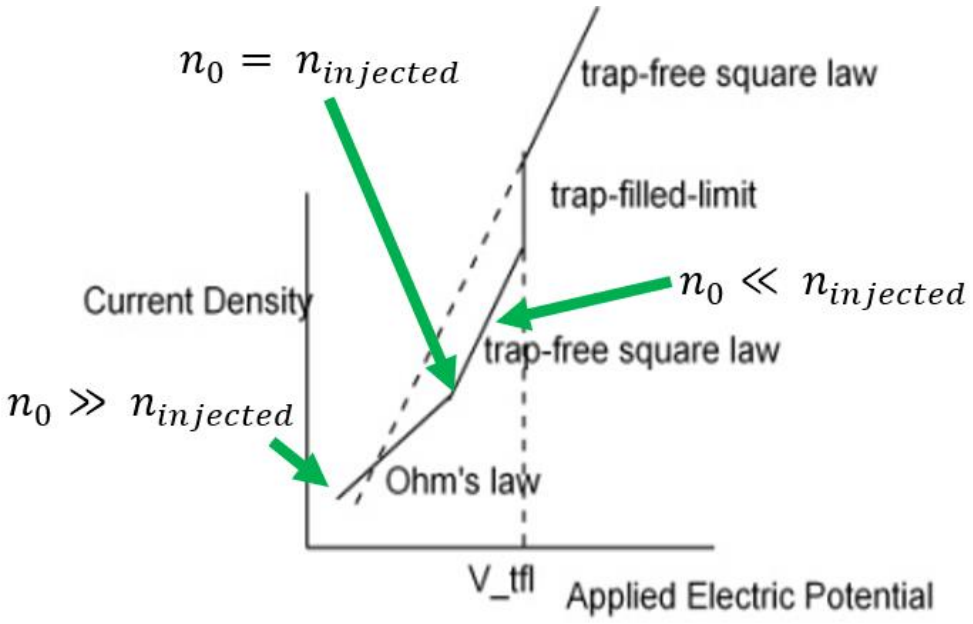

Figure 38. Voltage regions where the trap and free charge concentrations relate.[29]
Ohms law is expressed in the following

$$J_{thermal} = qn_0\mu_{eff}\frac{V_a}{D} \tag{5.5}$$

Where n_0 is the charge carrier concentration, Va is the applied voltage, and D is the thickness, and μ is the effective mobility. At higher voltages additional charge carriers are injected in the oxide, and the concentration of free charge carriers increases beyond n_o. The device loses its Ohmic characteristic and the current is proportional to the voltage square. On a log-log plot the slope is now 2 as shown in figure 38 above. Both the average speed of the carriers (μ*V/d) and the number of charge carriers ($n_{injected}$) increases with higher voltage leading to the observed square relation described in equation 5.4. The change from an ohmic slope to the trap free square law is the intersection of both curves and identified by the transition voltage V_x. The charge carrier

concentration can be determined from the voltage of this transition. Figure 39 illustrates the particular voltage where the trap and free concentrations are equal.

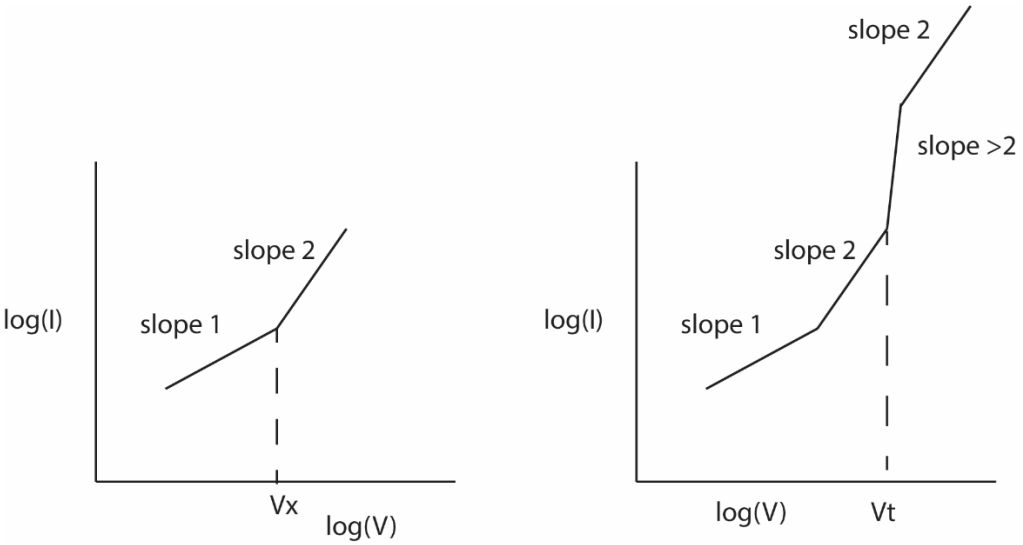

Figure 39. The transition voltage V_x and the threshold voltage .The transition voltage V_x identifying the cross over from Ohmic to square IV behavior (left) and the threshold voltage identifying the effect of deep traps.

Let it be noted that this technique that determines the low voltage charge carrier concentration cannot distinguish between holes or electrons. The equation used for the determination of the charge carrier concentration from the transition voltage V_x is as follows.

$$n_0 = \frac{V_x K_s \varepsilon_0}{qL^2} \tag{5.6}$$

Where n_0 is the low voltage charge carrier concentration, L is the thickness of the oxide, K_s is the oxide semiconductor's dielectric constant, and q is the charge carrier charge. The dielectric constant used to determine the carrier concentration of the NiFeO films was 250. This value was measured by Leblanc using an HP impedance analyzer (for low

frequency measurements data)[30]. Once the concentration is known the mobility of the oxide can be determined from the resistivity of the oxide. For this analysis it is assumed that θ equals one. There are many ways charge carriers can move through the oxide which is a topic up to much debate on which way dominates. The figure 40 shows various conduction mechanisms in the oxide.

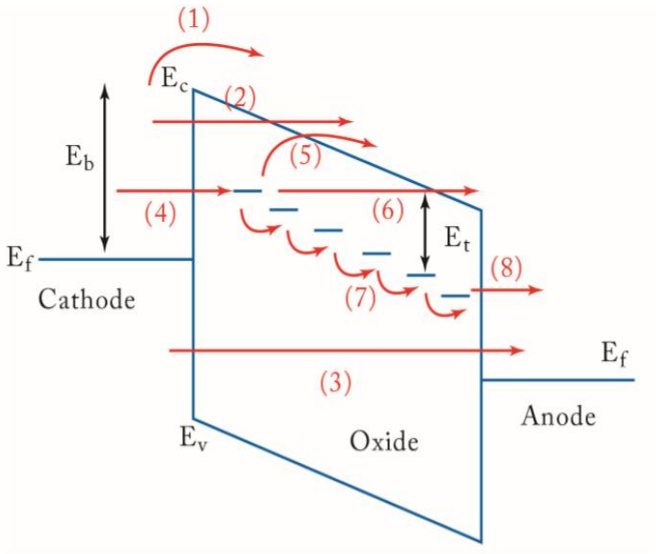

Figure 40. Schematic for the charge carrier paths through the oxide. 1) Schottky emission; 2) F-N tunneling; 3) direct tunneling; 4) tunneling from cathode to traps; 5) emission from trap to conduction band, which is essentially the Poole-Frenkel emission; 6) F-N- like tunneling from trap to conduction band; 7) trap-to-trap hopping or tunneling; and 8) tunneling from traps to anode[31].

In Figure 41 an IV curve is shown for a low oxygen flow NiFeO sample on n-type silicon. This figure is the same data but presented differently from figure 35. Near zero volts the resistance changes quite rapidly which is related to the filaments for resistive switching. The process was not completed at 4 volts possible due to no time constraints on this measurement.

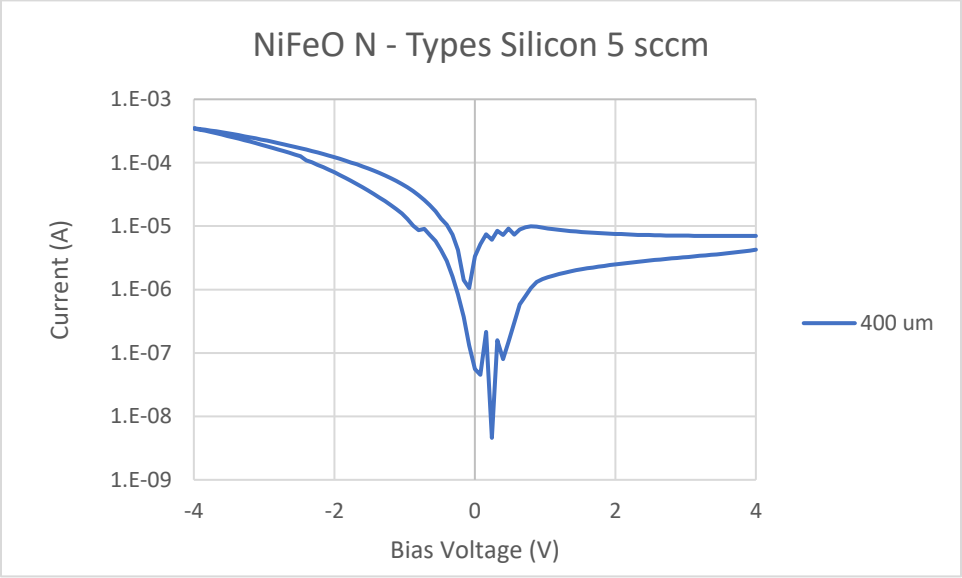

Figure 41. Resistive switching and diode behavior log(I) vs V for Au/NiFeO/n-Si. Wafer name 52618-02. Device code 22.400.1.

The general explanation for resistive switching is the concept of generating oxygen vacancies and the migration of oxygen ions (O^{2-}) which creates a conductive metallic filament between the top and bottom electrodes[31]. The concept of this path is revealed in figure 42.

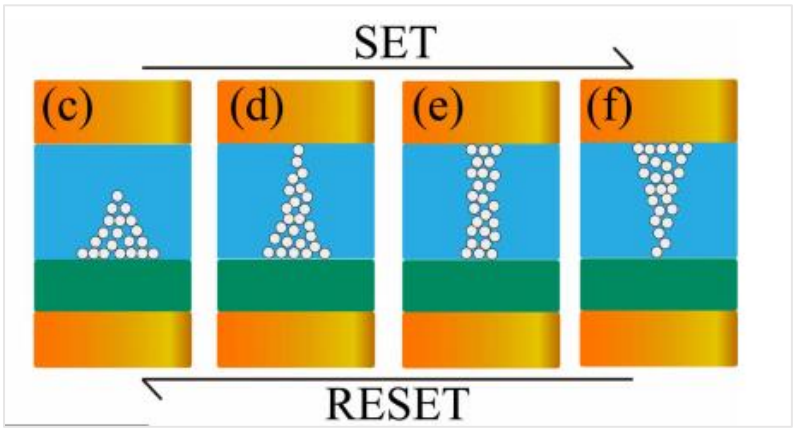

Figure 42. Schematics of the switching process. Circles are the oxygen vacancies. [32]

The mechanism for this hysteresis comes with a variety of other possible explanations. There are two different conduction mechanisms, one that focuses on the electrode oxide interface and the other that focuses on the bulk of the oxide material. Figure 43 summaries these conduction mechanisms relative to either the interface or bulk.

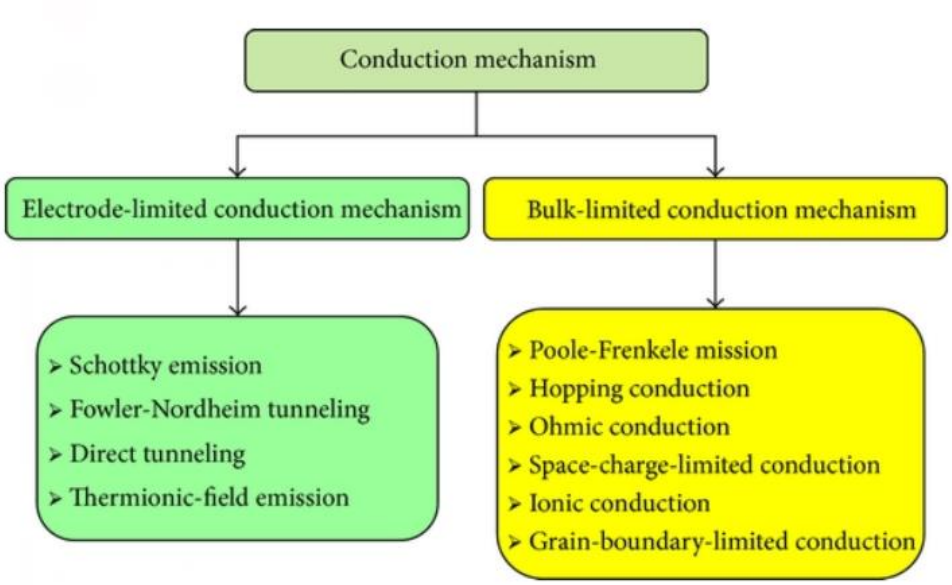

Figure 43. Conduction Mechanisms for dielectrics[33].

Figure 44 shows the current voltage behavior of low oxygen concentration NiFeO on p type silicon for a 400 um device.

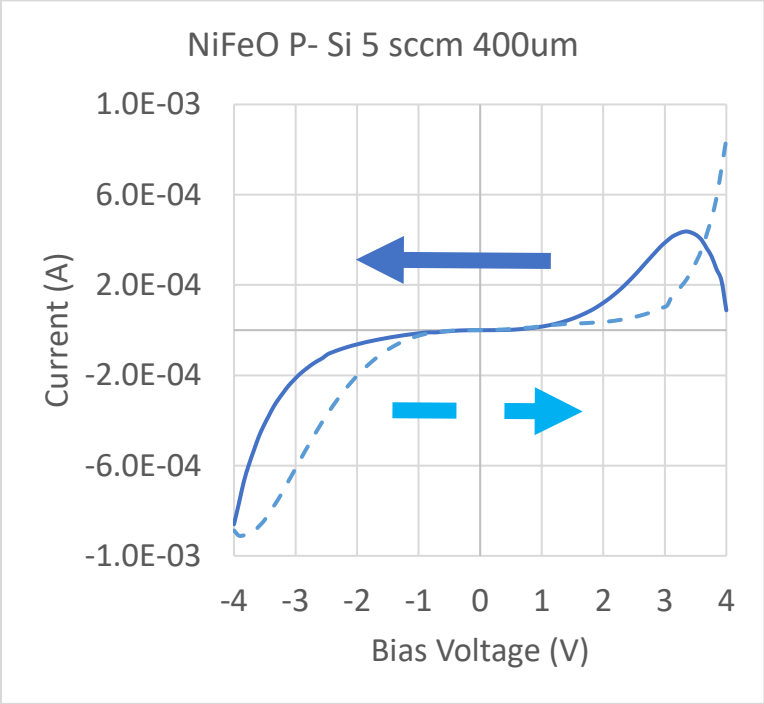

Figure 44. IV curves Au-NiFeO-Si devices: $Ni_{0.8}Fe_{0.2}O_{1-\alpha}$/p-Si. Wafer name 52618-02. Device Code 22.400.1.

The arrows refer to the direction of the voltage sweep with the dark solid blue line indicating the start of the measurement. This measurement used a 500ms delay between each measurement but jumped from zero volts to 4volts with no hold. When NiFeO is grown on a p type silicon wafer the first obvious change of the IV-curve is the disappearance of the rectifying properties. Although the hysteresis is still a behavior that is observed. The voltage cycle goes +4V → 0 → -4V → 0 → +4. A current jump around 4 volts could have a few possible explanations. The reset process for the switching mechanisms failed is one possible explanation. Or this jump could indicate that the Schottky barriers effect is not solely responsible for the hysteresis effects[25]. This current jump could also be a measurement defect due to the lack of a hold time constraint. Comparing low oxygen flow NiFeO grown on n and p substrates the current is

greater for the NiFeO grown on p substrates. This could be due to the bulk effects that govern the resistive switching. The space charge limited current (SCLC) is based off bulk effects which results from oxygen vacancies in the oxide. As there is not a strong rectifying effect these results suggest that there is no significant barrier for holes in the NiFeO/p-Si devices while there is a significant barrier for electrons in the NiFeO/n-Si devices. Further analysis of the IV data of figure 44 is presented in the appendix A.

The results of this section all had gold contacts sputtered on top of the oxide layer. According to literature gold is an inert material that has no high diffusivity or mobility in NiO which makes the creation of a gold filament difficult and unlikely[25]. Metallic ions are needed to form the filaments through a redox action in the oxide. The silicon substrate might have influenced this in favor of resistive switching while using gold electrodes.

Increasing the oxygen flow in the chamber to 20 sccm drastically changes the electronic properties of the NiFeO when grown on silicon substrates. Figure 45 below demonstrates the IV properties of device wafers made with a high oxygen concentration NiFeO film grown on an n type silicon substrate. For the device wafers made with high oxygen NiFeO no hysteresis was observed. The devices had strong rectifying properties with the $I_{forward}/I_{reverse}$>1000-10,000.

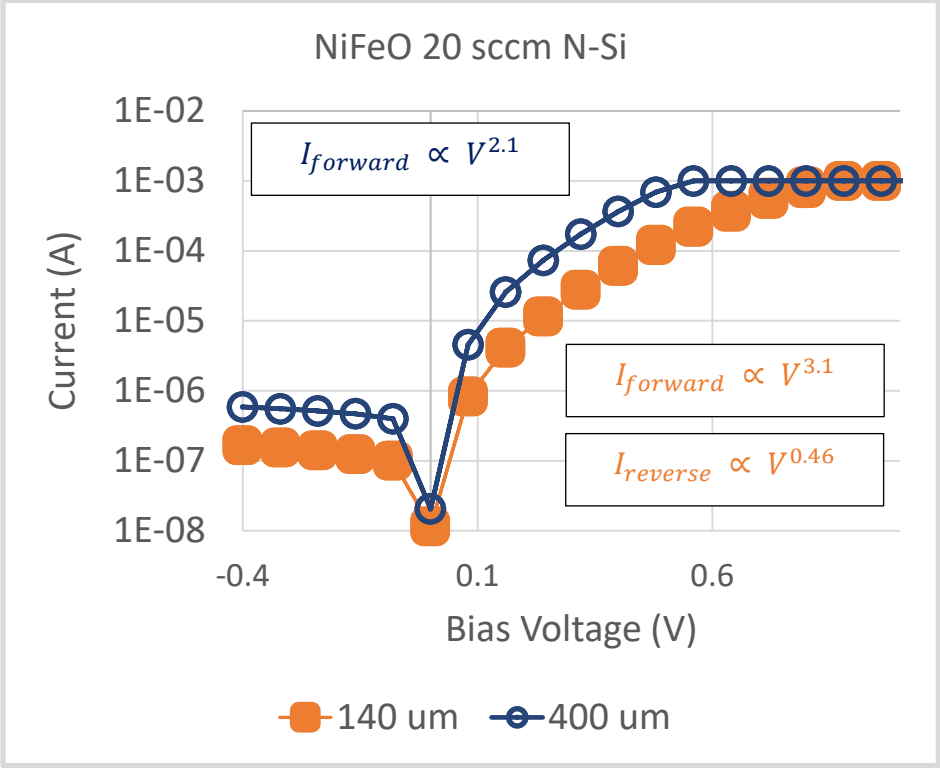

Figure 45. IV curves Au-NiFeO-Si devices, $Ni_{0.8}Fe_{0.2}O_{1+\alpha}$ /n-Si Device area**.** Wafer name 52818. Device code 22.400.0, Device Code 22.140.0.

The rectifying properties remain for this device structure due to the p-n heterojunction of the NiFeO silicon interface. However, no resistive switching is observed. This measurement used a 200ms delay on each measurement and no hold was used after the first voltage change. At high voltages, the current relates to the voltage by an exponent of 2.1 for the 400 um device in forward bias (i.e. $I \propto V^{2.1}$). V_x was estimated from the IV-curves shown in Figure 46 and 47 and was approximately 0.028 volt.

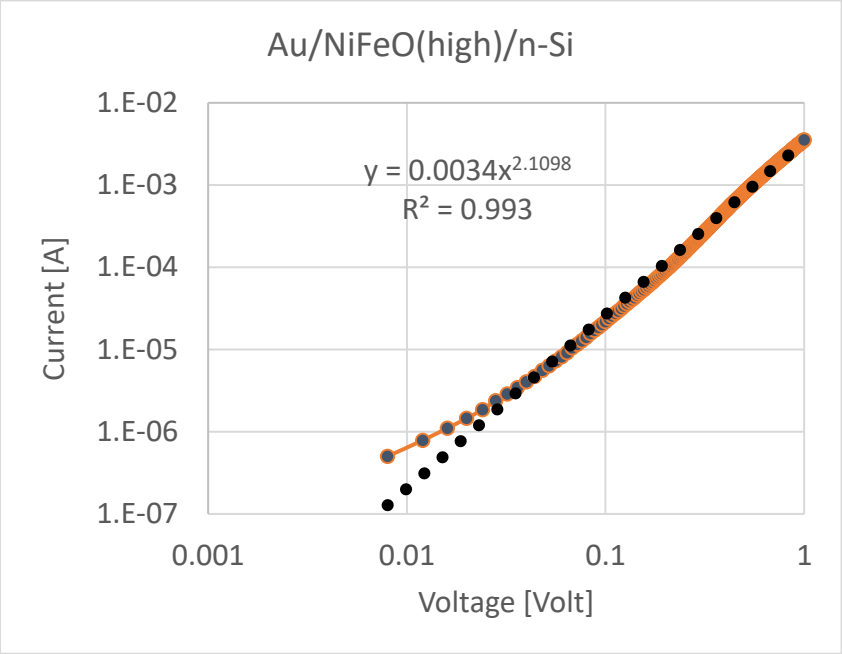

Figure 46. log-log Square Law for High oxygen flow NiFeO on n-Si.

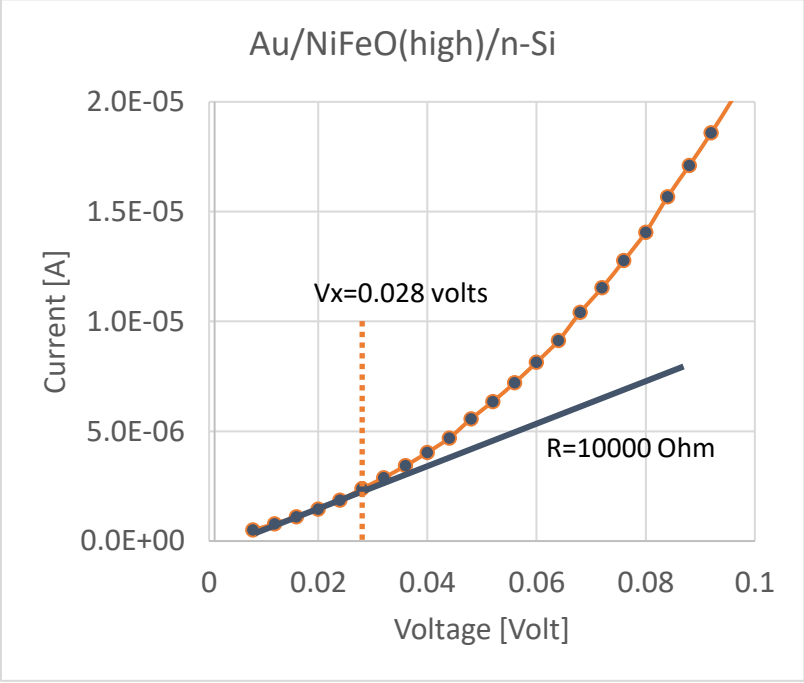

Figure 47. V_x determined from IV for High oxygen NiFeO.

Using this V_x, the charge carrier concentration was estimated using equation 5.6. Then the mobility was calculated using the resistance of the high oxygen flow NiFeO. Results are summarized in the following table 7.

Table 7. Mobility for high oxygen flow NiFeO.

Vx	**0.028 V**
Ks	250
ε_0	8.85×10^{-12} (F/m)
q	1.6×10^{-19} C
L	26 nm
A	6.08×10^{-7} m^2
R (low voltage)	10000 Ω
R (Similar Device)	10 Ω
R (Parallel Resistivity)	5.56 Ω
n_0	5.73×10^{23} m^{-3}
n_0	5.73×10^{17} cm^{-3}
μ	8.39×10^{-8} m^2 / V s
μ	8.39×10^{-4} cm^2 / V s

It is currently not clear if this is the electron or hole mobility of the NiFeO. The results of RBS and XPS measurements on NiO and NiFeO films sputtered under similar conditions suggest that the oxide films sputtered under high oxygen flow do not have oxygen vacancies but instead have metal vacancies which explains why no hysteresis and or switching was observed for high oxygen flow devices [38,39]. Figure 48 compares a gold/n-Si IV curve with the IV curve of a gold/NiFeO/n-Si device. The currents are larger for a device that includes a NiFeO layer. Note that the leakage current data of the devices are largely scattered.

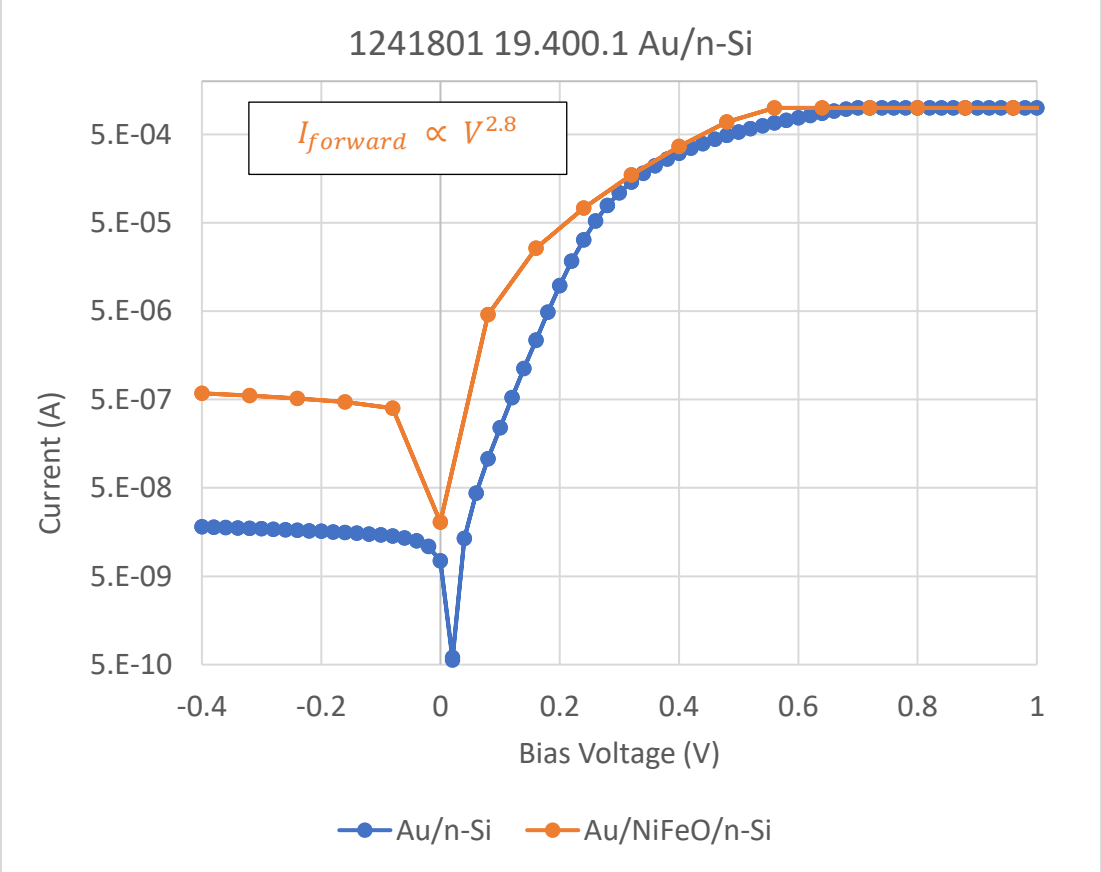

Figure 48. IV Comparison for Au/n-Si and Au/NiFeO/n-Si. Wafer name 1241801. Device code for Au/n-Si 19.400.1 and NiFeO 22.400.0.

Figure 49 below shows the IV curve of device made with high oxygen flow NiFeO on p-Si. Note that the devices on p-Si are no longer rectifying but keep a non-linear IV curve. For both measurements a delay time of 200ms was used but no hold time after the first voltage change. This also suggests that the valence band of the NiFeO and p-Si line up. The non-linear IV curve suggests that a symmetric barrier might be present possibly caused by charged defect states at the p-Si-NiFeO interface. For the Au/Si device the current has been shifted to the right by exposure to a light source. Figure 49 also shows the difference between similar devices on n and p silicon.

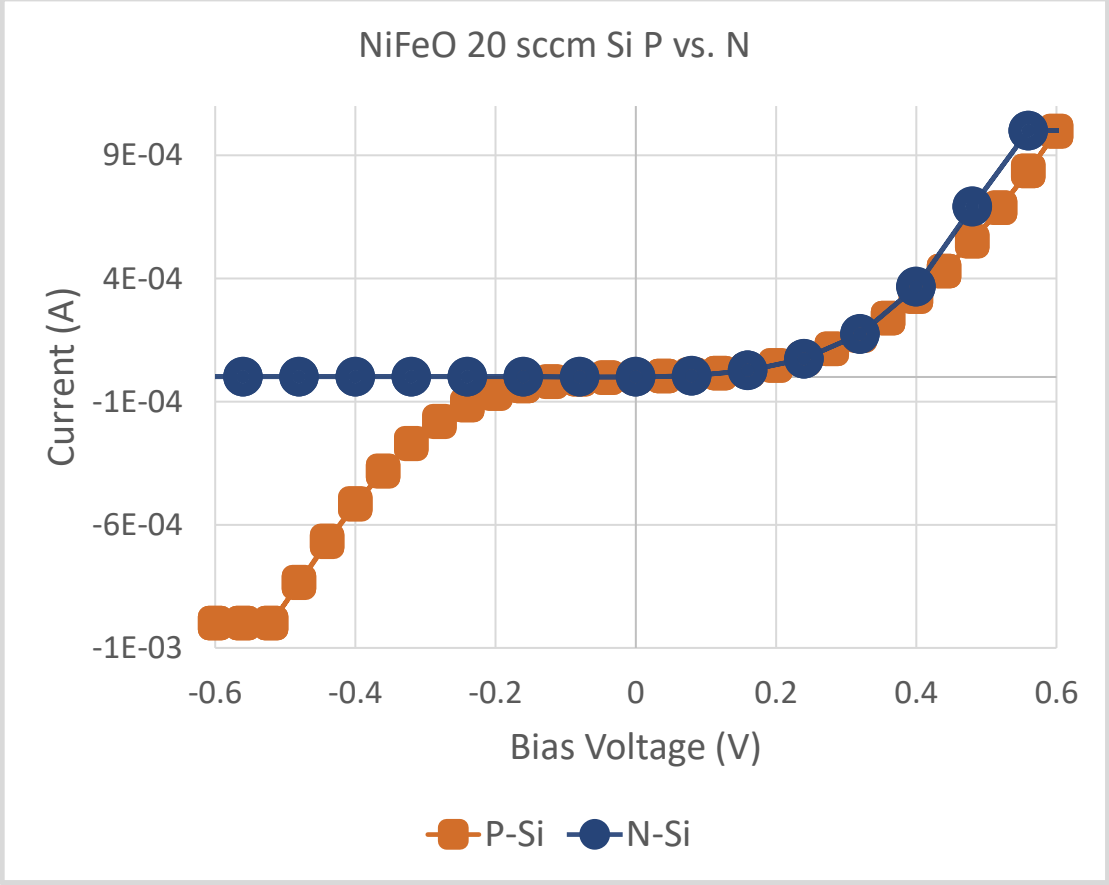

Figure 49. Comparison N- Si vs P-Si IV curves Au-NiFeO-Si devices. $Ni_{0.8}Fe_{0.2}O_{1+\alpha}$ /p-Si. Wafer name 5281801 for n-Si. 5281802 For p-Si. 22.400.1 device code for both measurements.

So, the IV curves measured on NiFeO-Si hetero-junctions suggest that the valence band of silicon sits just below the valence band of NiFeO and that NiFeO films are p-type. So, heterojunctions of NiFeO thin films sputtered on p-Si are not rectifying while heterojunctions of NiFeO thin films sputtered on n-Si are strongly rectifying. Also, the measurement on p type silicon used a 200ms delay time but no hold time after the first voltage change. These conclusions are summarized in the graphs of figure 50 below. A negligible band valence band offset between NiFeO and Si is consistent with literature. The valence band edge of Si is approximately located at 5.17 eV while the estimated valence band edge of NiFeO is approximately located between 4.2-4.7 eV (using a weighted average of the properties of NiO and FeO reported on in literature).

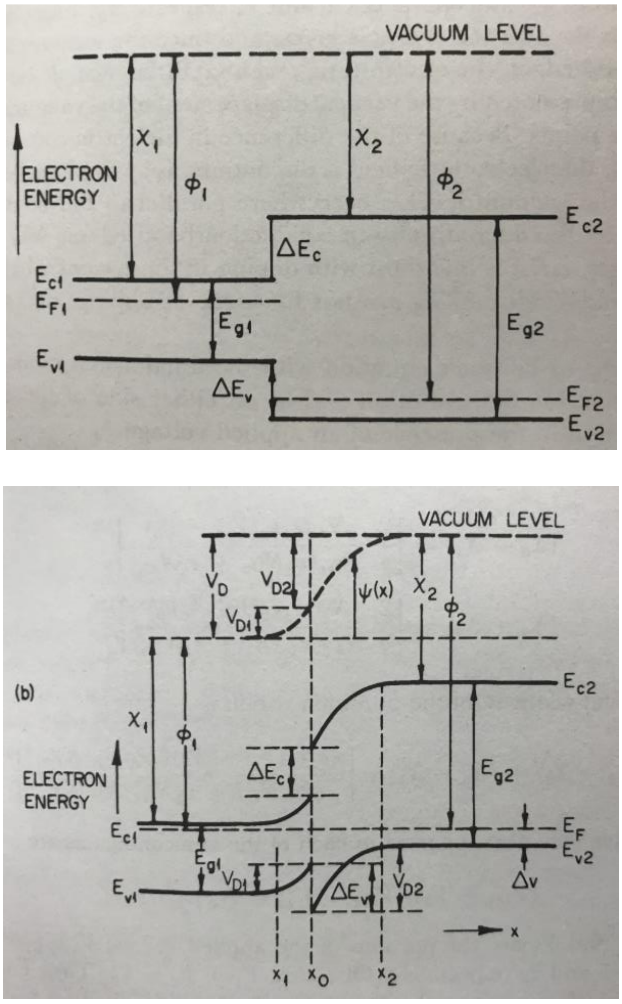

Figure 50. Band Diagram isolated semiconductor (top) and heterojunction (bottom). Band offset of NiFeO and n-Si for the isolated semiconductors (top) and energy band diagram of NiFeO/n-Si heterojunction (bottom) at thermal equilibrium[34].

Figure 51 below shows the IV characteristic of high oxygen flow Pt/NiOPyO/n-Si devices. Note that the estimated Fe concentration of this device was approximately 10% and varied from the iron concentration of the other devices reported on in this thesis. resulting in $Ni_{0.9}Fe_{0.1}O$. The space charge limited current dominates in forward bias. Reverse bias has a linear relationship between the current and voltage and yields a resistance of 33MΩ.

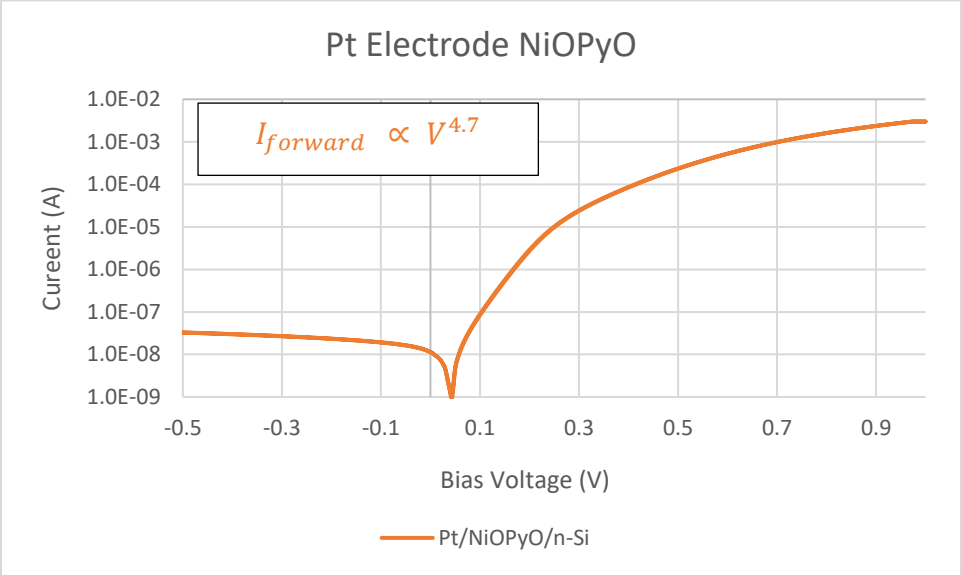

Figure 51. IV characteristics for Pt/NiOPyO/n-Si. Wafer name 41519. Device code 22.400.1.

In figure 52 a comparison between a Pt/Si junction is displayed along with the inclusion of an oxide between the electrode and the substrate.

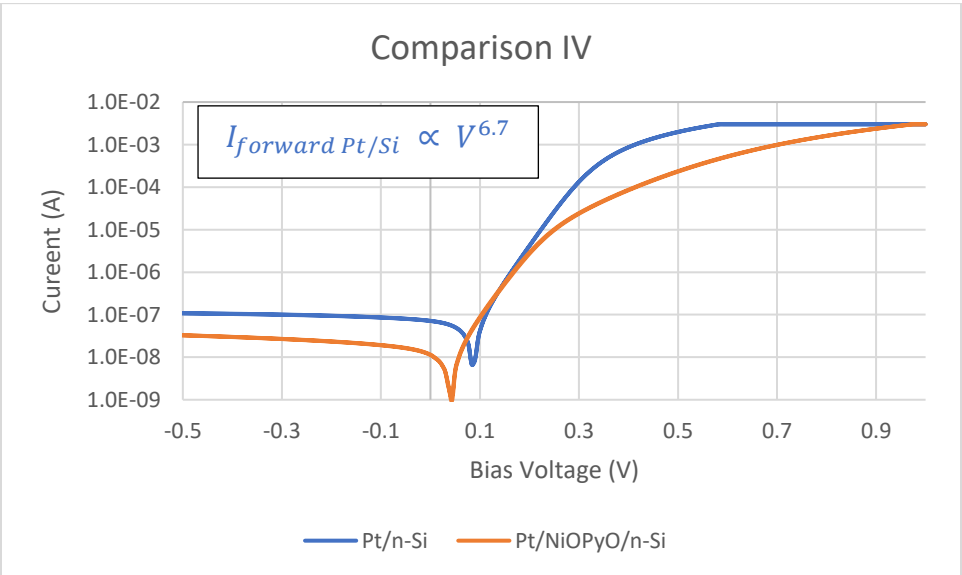

Figure 52. IV Comparison of the inclusion of NiOPyO between Pt and n-Si. Wafer name 41519. Device code 22.400.1 and 25.400.1.

The oxide does seem to change both forward and reverse bias current voltage relationships. In forward bias the space charge limited current dominates independent of the inclusion of the oxide layer. This measurement used a 300ms time delay with no hold. The exponent differs with the inclusion of the oxide layer by a factor of 1.4. In reverse bias for a Pt/n-Si junction the current is constant which is consistent with a saturation current which has an approximate value of 1.18×10^{-7} A. Since this sample was exposed to a light source the IV curve was slightly shifted right. The addition of the oxide layer has not diminished this light current but shift the current down and to the left.

Capacitance-Voltage Relationship Results

For conductivity mobility two different measurements are required to obtain the quantity. Resistivity and carrier density measurements are required when one wants to determine the mobility in the material. Carrier concentration is normally measured via the Hall effect, the magnetoresistance effect or from CV measurements. The latter technique can provide this information from the slope of a $1/C^2$ versus bias voltage plot. The CV curve can be measured with the probe station. The resistivity of the NiFeO films can be determined from current voltage measurements using a linear four point probe system. The linear four point probe system measures the sheet resistance and the resistivity is obtained by multiplying that quantity by the thickness of the film. The carrier density can then be obtained from a capacitance voltage measurement. A DC bias voltage is applied to the film stack which creates a depletion area. Then a small signal AC voltage of 10-20mV magnitude is superposed on the DC bias voltage with a frequency in the range of 1kHz to 1MHz. One converts the C-V plot into a $1/C^2$ vs. bias voltage plot and from the slope of the plot the carrier density can be obtained. CV measurements were taken of

devices on the high oxygen flow NiFeO/n-Si wafer using the single probe connections as the following figure indicates. The CV Measurements were made similar to the IV measurements with a single wire conventional probe directly placed on the top electrode and chuck which is depicted in figure 53. The capacitance is measured through the wafer and the chuck and this capacitance should not be an issue due to the area being so large that it approximates a short circuit.

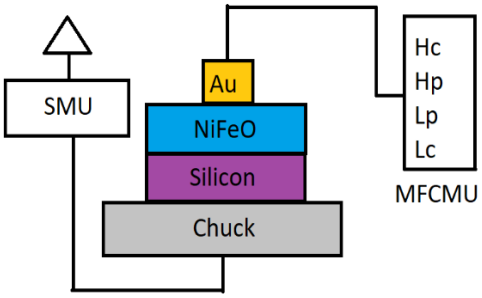

Figure 53. CV electric measurement configuration.

A metal-semiconductor junction was measured using this technique to determine the doping concentration of the wafer. A n-type silicon substrate was used for these tests with 100nm thick gold electrodes sputtered using a shadow mask. The apparent donor concentration can be calculated from the device area A, dielectric constant of the Si K_s, the permittivity of free space ε_o, the elementary charge q, and the slope of the $1/C^2$-Vbias curve using the following equation:

$$N_D = \frac{2}{qK_S\epsilon_0 A^2 \frac{d\frac{1}{C^2}}{dV}} \tag{5.7}$$

This carrier density is called the effective carrier density since the value is approximately the majority carrier density. The assumptions that premise this calculation require the substrate to be uniformly doped and for the depletion region to exist in reverse bias. Capacitance measurements were done in reverse bias ($V_a < 0$) to focus on the majority carriers. This concept is referred to as the depletion approximation where $N_D \approx n$ (i.e. the majority carrier concentration). This approximation also assumes total depletion for majority carriers in the space charge region to a depth of W and perfect charge neutrality beyond the depletion depth. This concept is depicted in figure 54.

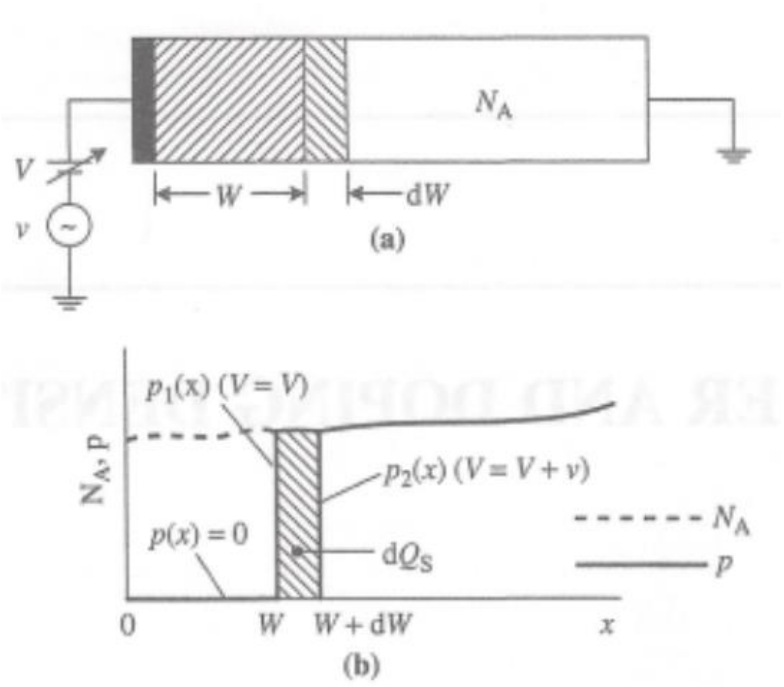

Figure 54. Schottky contact in reverse bias (top) and probed charges (bottom)[35].

Since the doping concentration is inversely proportional to the device area square (equation 5.7), it is important that the exact device area is precisely known for reduced error. On that note the following table 8, measured using the Hirox optical digital

microscope, shows the specific areas of the devices on the device wafer. Note that the realized device size was up to 40 um larger from the nominal design device size.

Table 8. Measured Radius of Au Electrodes on Silicon Substrate.

Au/Si Junction							
Target Radius (um)	400	280	200	140	100	71	50
Measured Radius (um)	418±1	305±1	232±1	175±1	137±1	109±1	84±1

The width of a reverse biased depletion region depends on the applied voltage and thereby depends on the capacitance which is defined as follows.

$$W = \frac{K_s \epsilon_0 A}{C} \tag{5.8}$$

The dielectric constant (K_s) for the NiFeO semiconductor used two different values depending on the measurements and the frequency used. For the CV measurements which uses high frequencies a dielectric constant of 50 was used[30]. The following graph shows the electrode area influence on the capacitance as it scales with the gold contact area. The y axis contains the inverse square of the capacitance and the x axis shows the reverse bias voltage which is shown in figure 55.

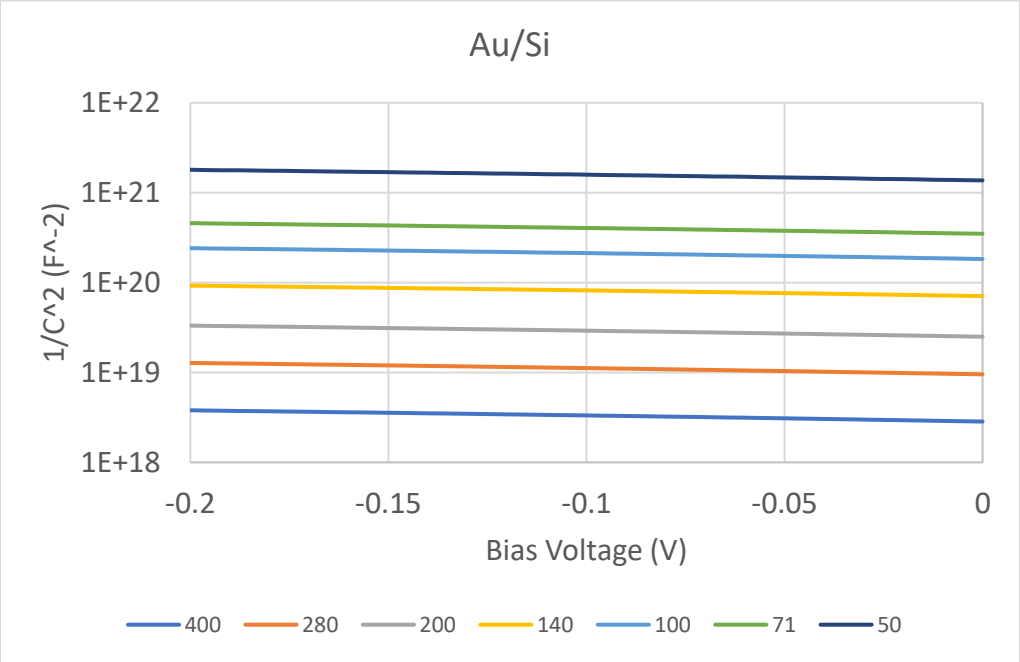

Figure 55. $1/C^2$ vs. bias voltage for Au/Si junction.

The following table 9 displays the values of the slopes from the fitted ($1/C^2$) curve. As well as the associated measured radii and the built-in voltage for each device.

Table 9. Built-in Voltages for Au/Si with calculated barrier height.

Die 19	**Film Stack**	**Au/n-Si**	
Radius Target (um)	Average Radius Measured (um)	($1/C^2$) Slope (F^{-2} V^{-1})	Built-in Voltage (V)
400	418 ± 5	4.66×10^{18}	0.61
280	305 ± 9	1.59×10^{19}	0.6
200	232 ± 7	4.16×10^{19}	0.6
140	175 ± 7	1.04×10^{20}	0.68
100	137 ± 8	3.00×10^{20}	0.67

Table 9. Continued			
71	109 ± 7	3.72×10^{20}	0.61
50	84 ± 7	2.11×10^{21}	0.65
AVERAGE			0.63±0.03
Barrier Height		Agree with literature	0.79±0.04
Nc	2.8E19cm^3		

The largest device area starts off at the bottom of the graph and decreases as the inverse square increases. The inverse square increases by a factor 2 as the device area falls by a factor 2. Two quantities can be determined from the above graph, i.e. the dopant concentration and the built-in voltage. The built-in voltage (V_{bi}) describes the potential across the depletion region at zero external bias voltage. This quantity can be determined as the x intercept by the following equation.

$$(V_{bi} - V_a) = \frac{q\epsilon_0 N_{d\,or\,a}}{2C^2} \qquad (5.9)[35]$$

The determination of the built-in voltage for a device with radius 400um is plotted below in figure 56 to demonstrate this technique.

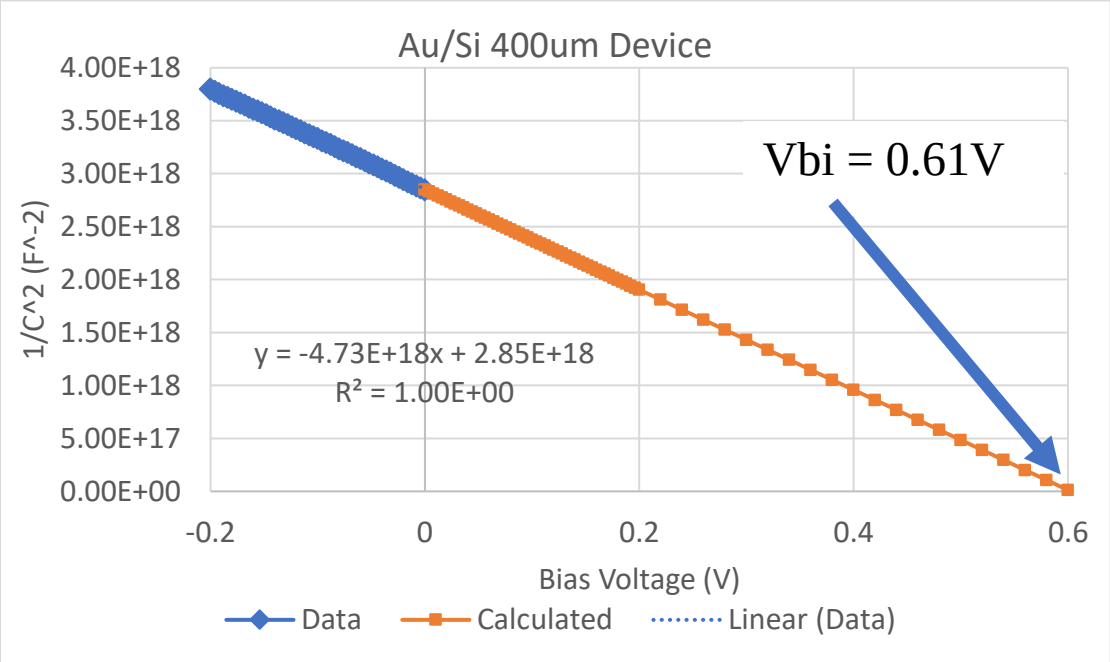

Figure 56. $1/C^2$ vs. Bias Voltage 400um Au/Si Device. Wafer name 12418-01. Device code 19.400.0.

The built-in voltage can be used to determine the barrier height of the semiconductor. This relationship is displayed by the following equations.

$$V_B = V_{bi} + V_o$$

And (5.10)[22]

$$V_o = \frac{kT}{q} \ln\left(\frac{N_c}{N_D}\right)$$

Nc is the effective density of states in the conduction band which for Si at room temperature is 2.8×10^{19} cm^{-3} [35]. Using the $1/C^2$ slope the donor concentration was used for the thermal voltage as well with a value of 8.6×10^{22} m^{-3}. Using this value and a doping concentration of 1×10^{17} cm^{-3} for the silicon equation 5.7 yields a barrier height of 0.79 ± 0.04 V, so an energy barrier of 0.79 eV. From literature a common barrier height from this technique using gold contacts is described in electrons volts of 0.79eV[35]. The

barrier height can also be estimated from the electron affinity of Si (4.05 eV) [9] and the metal work function of gold is 4.76eV using equation 5.8, to be approximately 0.71 eV. Note that this is an overestimate as the barrier is lowered by imaging effects.

$$q\phi_{bi} = q(\phi_m - \chi) \tag{5.11}$$

A typically energy band diagram of a metal semiconductor junction is reported in figure 57 below.

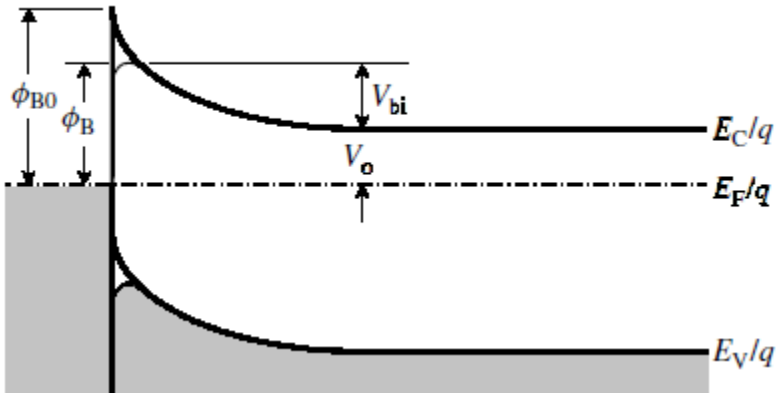

Figure 57. Energy Band Diagram for a rectifying metal semiconductor junction[35].

Using the slope for the inverse square capacitance graphs the donor density (N_D) is obtained from the silicon. The silicon wafer used was a n-type wafer which means that $N_D > N_A$, $V_{bi} < 0$, for $V_a < 0$. The results are shown for different device sizes in figure 58 below. It is currently not clear what causes the observed device size dependence.

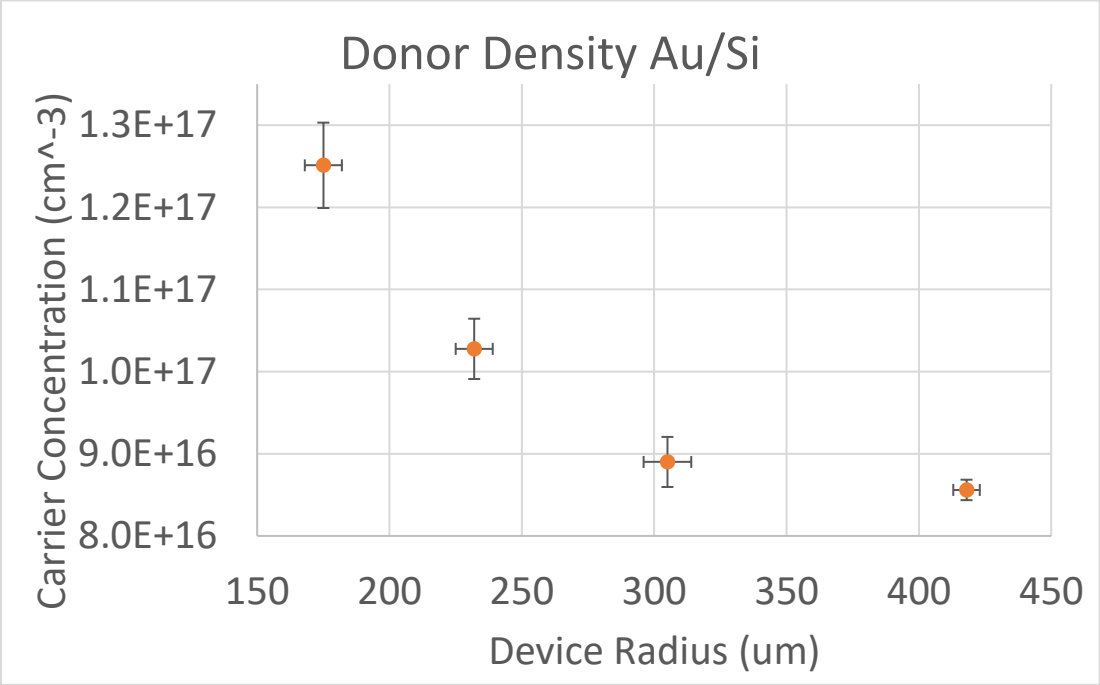

Figure 58. Donor Density vs. Area for Au/Si. Wafer name 12418-01. Device code 19.400,140.01.

The conductivity mobilities were calculated using the depletion approximation (i.e. $N_D \approx n$). The equation governing this calculation is defined below.

$$\mu = \frac{1}{qn\rho} \tag{5.12}$$

Where q is the electronic charge and n is the charge carrier density which is approximately equal to the donor density due to the depletion approximation. The calculated mobility for the larger devices is close to the hole mobility reported in textbooks for n-doped Si. The measured values are displayed in figure 59.

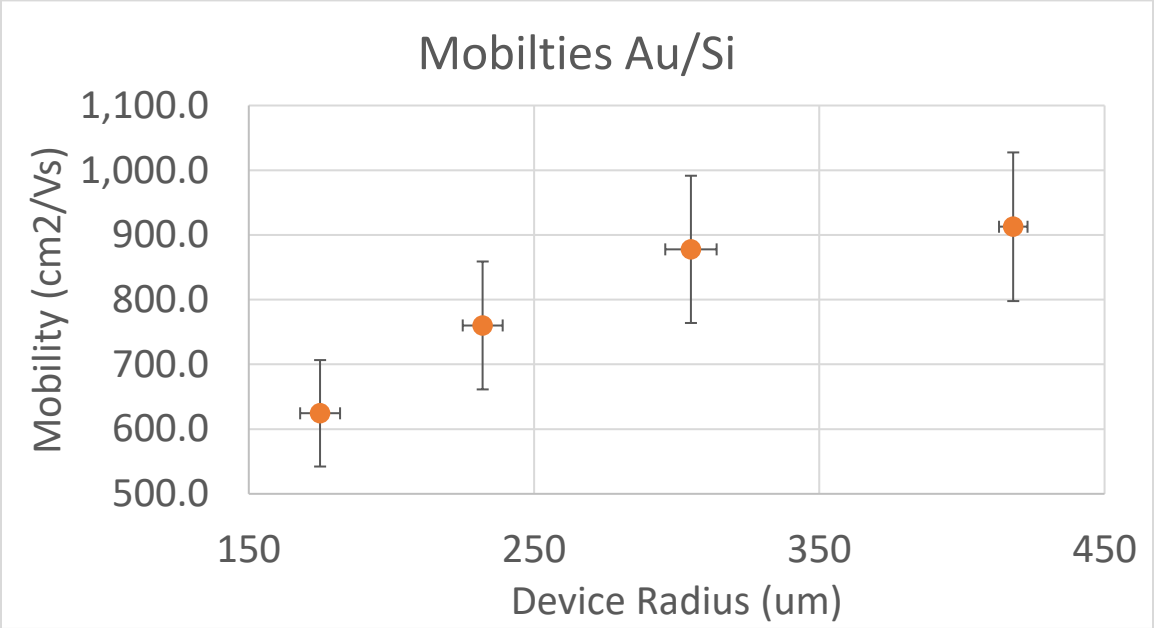

Figure 59. Mobilities for Au/Si. Wafer name 12418-01. Device code 19.400,140.01.

From literature the electron mobility for a arsenic doped silicon wafer is between 1184-731 $cm^2V^{-1}s^{-1}$ for doping concentrations between 10^{16}-10^{17} cm^{-3}[35]. The wafers used in this test were doped with antimony (Sb) which closely resembles a doped arsenic wafer. Using equation 5.4 the depletion area for the gold/n-silicon Schottky barrier is shown below to be only a few nanometers.

The CV properties of a p-n NiFeO/n-Si heterojunction was also measured using the previous mentioned techniques. The p type material is the high oxygen flow NiFeO sputtered film and the n-type material is the silicon substrate. A sputtered gold electrode is used which is shown in figure 33. Since there are two semiconductors in this device equation 5.7 cannot be used to determine the dopant density. Instead the equation has been alternated for an extra semiconductor layer by assuming an abrupt junction and uniformly doped semiconductors[34].

$$N_{Ap} = \frac{2\epsilon_n N_{Dn}}{d\frac{1}{C^2}/dV A^2 q \epsilon_n \epsilon_p N_{Dn} - 2\epsilon_p} \quad (5.13)[36]$$

Where ε_p is the permittivity of the NiFeO, ε_n is the permittivity of the n-Si, N_{Dn} is the donor concentration in the n-Si, N_{Ap} is the acceptor concentration in the NiFeO, A is the surface area of the device, and $d\frac{1}{C^2}/dV$ is the slope of the $1/C^2$-V graph.

Since the area is in the denominator is proportional to the area square of the device size must be precisely known to get a decent estimate of the acceptor concentration in the p-type NiFeO. The following table shows the surface areas of the devices size measured by the Hirox optical digital microscope.

Table 10. Device Radius for Die 11 Au/NiFeO/n-Si (high oxygen flow NiFeO)

Target Radius (um)	400	280	200	140
Measured Radius (um)	460±13	334±7	245±5	181±3

The capacitance measurements for PyO are explored in figure 60.

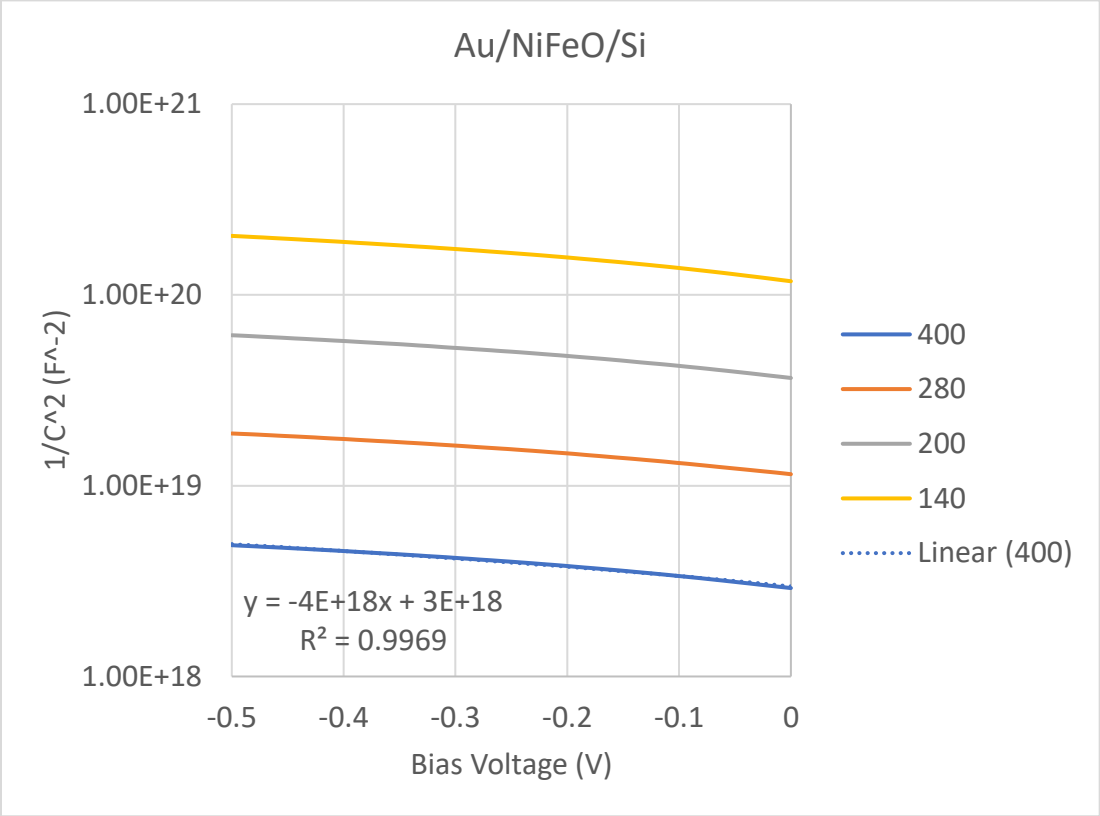

Figure 60. $1/C^2$ vs. Bias Voltage for Au/NiFeO/n-Si devices (high oxygen flow NiFeO).

The inclusion of the oxide layer did not influence the area scaling to the capacitance. The $1/C^2$-V slopes of the Au/n-Si Schottky diodes and the $1/C^2$-V slopes of the Au/NiFeO/n-Si heterojunctions are very similar suggesting the capacitance is hardly influenced by the presence of the NiFeO layer. However, the built-in voltage did increase possibly due to the NiFeO which is shown in figures 61 and 62 for two devices sizes.

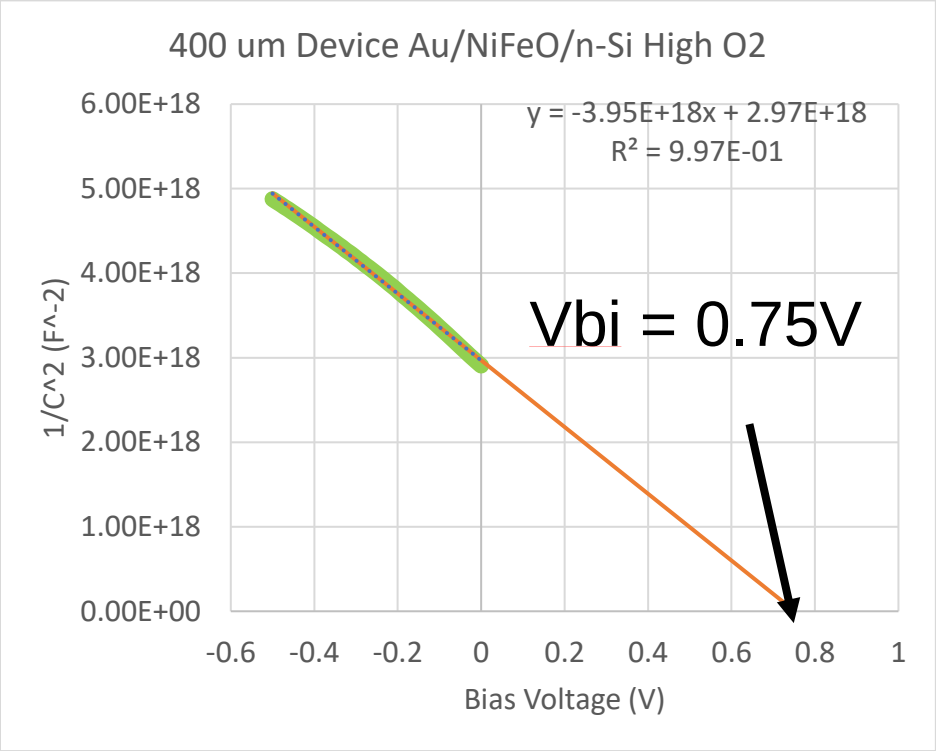

Figure 61. $1/C^2$ vs. V. High oxygen flow NiFeO for a 400um device.

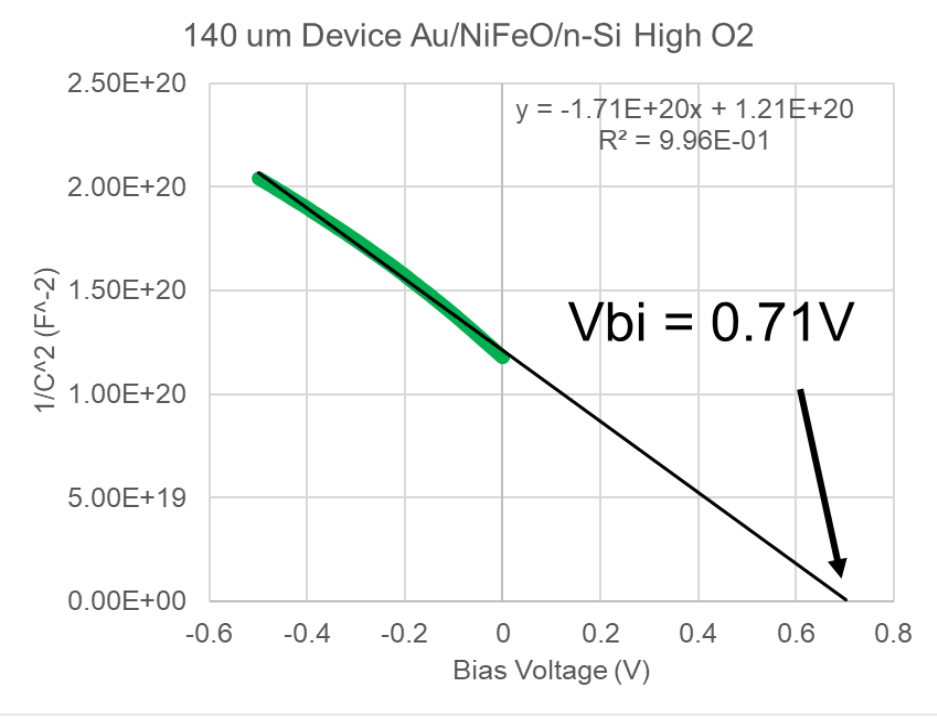

Figure 62. $1/C^2$ vs. V. High oxygen flow NiFeO for a 140um device.

Figure 63 below show the calculated doping concentration from the Si substrate using equation 5.7 and the measured slope on the Au/n-Si and the Au/NiFeO/n-Si devices. The graph also shows the calculated acceptor concentration in the NiFeO using equation 5.13 and the $1/C^2$-V slope of the Au/NiFeO/n-Si devices. The calculations suggest that the acceptor concentration in the NiFeO is in the 4-8E16 cm^{-3} range. The data also shows that the slope is not really affected by the insertion of the NiFeO layer, so the NiFeO layer might not contain a significant depletion layer.

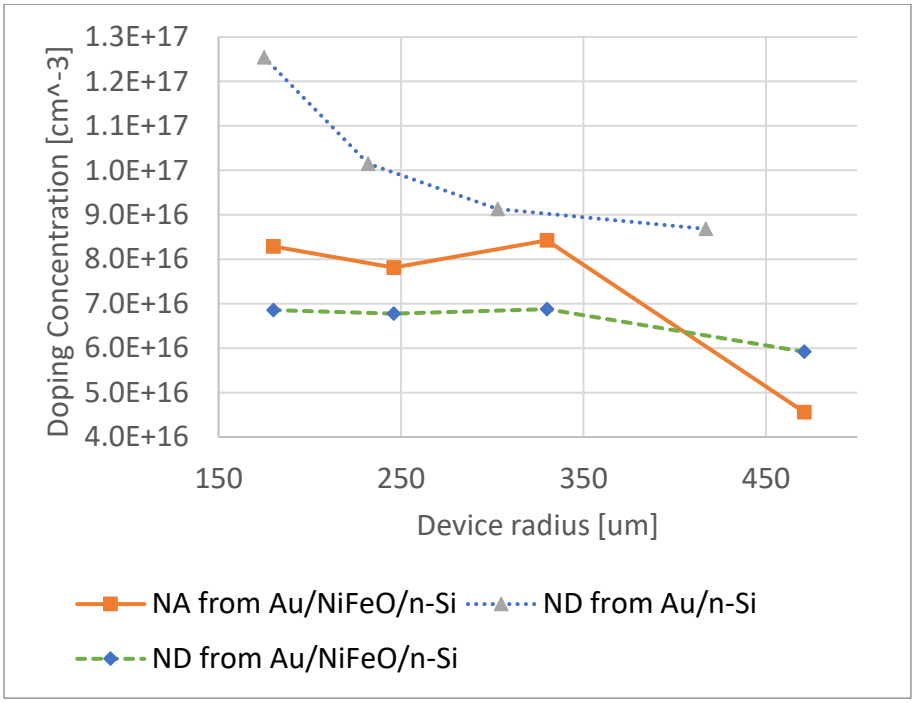

Figure 63. Dopant Concentrations Comparison of N_a and N_d of high oxygen flow. PyO/n-Si devices determined from CV curves.

The device size dependence suggests systematic errors in the calculated doping concentrations of ±25%. These results constitute questionable conclusions and therefore this data should be perceived as not more than a good guess. The slope found from the

$1/C^2$ graph seems to be very constant for similar electrode sizes but increases as the electrode size decrease. The built-in voltage seems to be different when comparing the devices with and without NiFeO. The table 13 below summarizes the data. The built-in voltage is larger for devices that include the NiFeO in between the silicon and the electrode similar to the results of [8] on Ag/NiO/n-Si devices.

Table 11. CV analysis with device area measurements.

Die 11	**Film Stack**	**Au/NiFeO/n-Si**	
Radius Target (um)	Average Radius Measured (um)	$(1/C^2)$ Slope (F^{-2} V^{-1})	Built-in Voltage (V)
400	460 ± 17	$4.2 \pm 0.9 \times 10^{18}$	0.75
280	334 ± 11	$1.5 \pm 0.2 \times 10^{19}$	0.76
200	245 ± 10	$4.93 \pm 0.04 \times 10^{19}$	0.80
140	181 ± 7	$1.7 \pm 0.1 \times 10^{20}$	0.71
AVERAGE			0.76±0.04
Die 19	**Film Stack**	**Au/n-Si**	
Radius Target (um)	Average Radius Measured (um)	$(1/C^2)$ Slope (F^{-2} V^{-1})	Built-in Voltage (V)
400	418 ± 5	4.66×10^{18}	0.61
280	305 ± 9	1.59×10^{19}	0.6
200	232 ± 7	4.16×10^{19}	0.6
140	175 ± 7	1.04×10^{20}	0.68

Table 11. Continued			
100	137 ± 8	3.00×10^{20}	0.67
71	109 ± 7	3.72×10^{20}	0.61
50	84 ± 7	2.11×10^{21}	0.65
AVERAGE			0.63±0.03

CV Measurement Challenges.

Figure 64 shows the CV-curve measured for different frequencies on the same device. As frequency increases the capacitance of a heterojunction should decrease which is observed in forward bias from figure 64. Although the reverse bias CV curve was reproducible, the forward bias CV data was scattered strongly and not always reproducible.

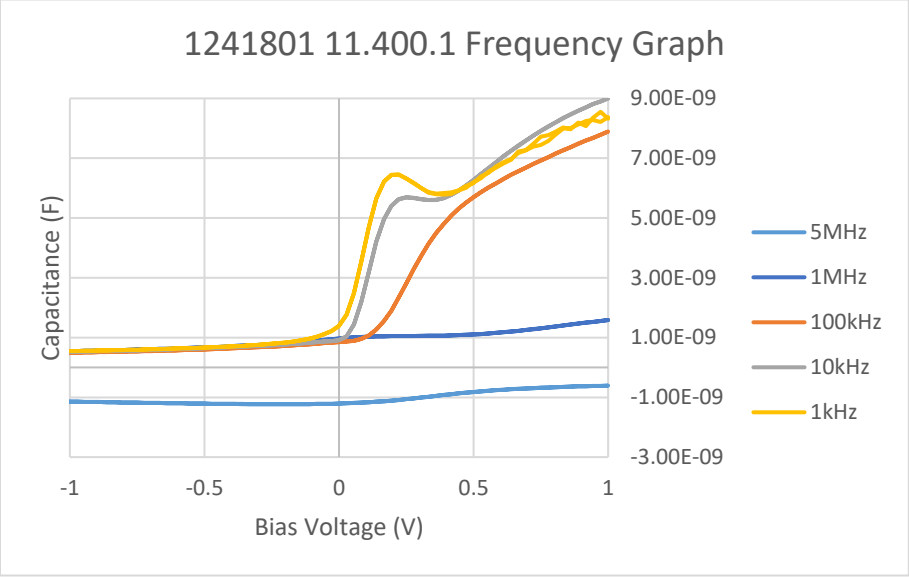

Figure 64. Mulitple Frequency Graph Au/NiFeO/n-Si. Wafer name 12418-01. Device code 11.400.1.

Figure 65 below may explain why the forward bias measurements were always in error. There might be significant leakage current when the chuck is in forward bias for a capacitance measurement. If the leakage current is significant this can be seen as power being dissipated and can give false readings.

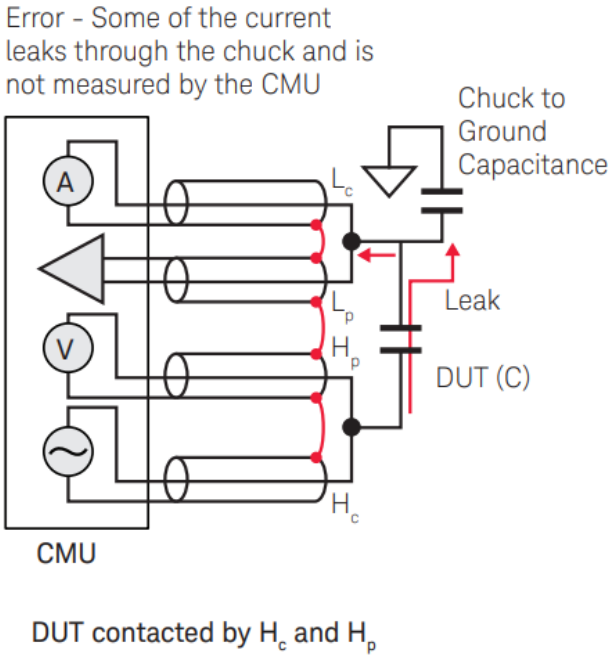

Figure 65. Schematic for forward bias capacitance measurements[37].

According to literature a quality factor less than 5 results in a false capacitance reading[22]. All tests done for this thesis yielded quality factors below 5 for forward bias and so no information exist for these devises in forward bias. Figure 66 shows the quality factor as a function of bias voltage and frequency.

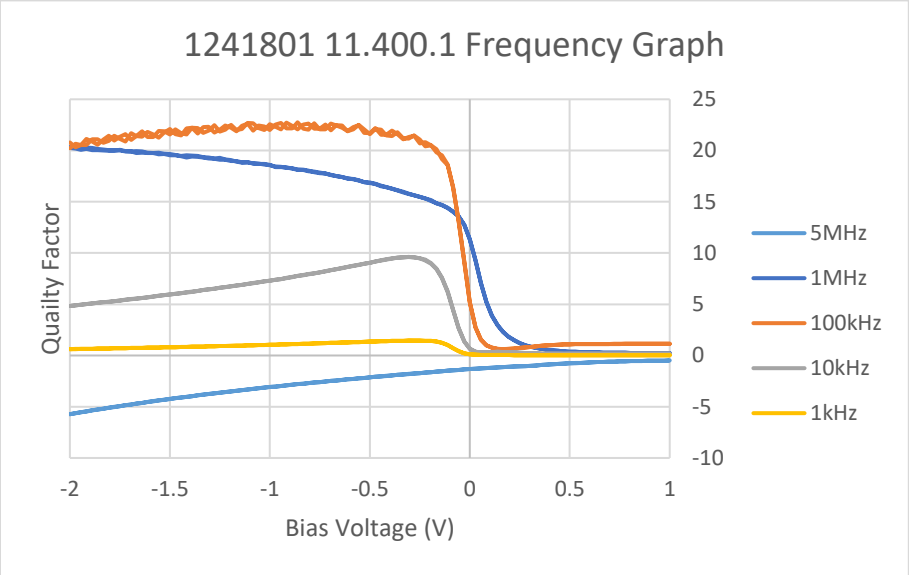

Figure 66. Quality factor vs. bias voltage with multiple frequencies.

The below schematic shows the connection of the Ground Switching Unit (i.e. Figure 67). This connection shorts the two probes so that the series inductance of the coaxial cables can be subtracted from the measurement. Shorting the two probes allows a path for any stray current to dissipate to ground rather than create a space charge that would affect the measurements.

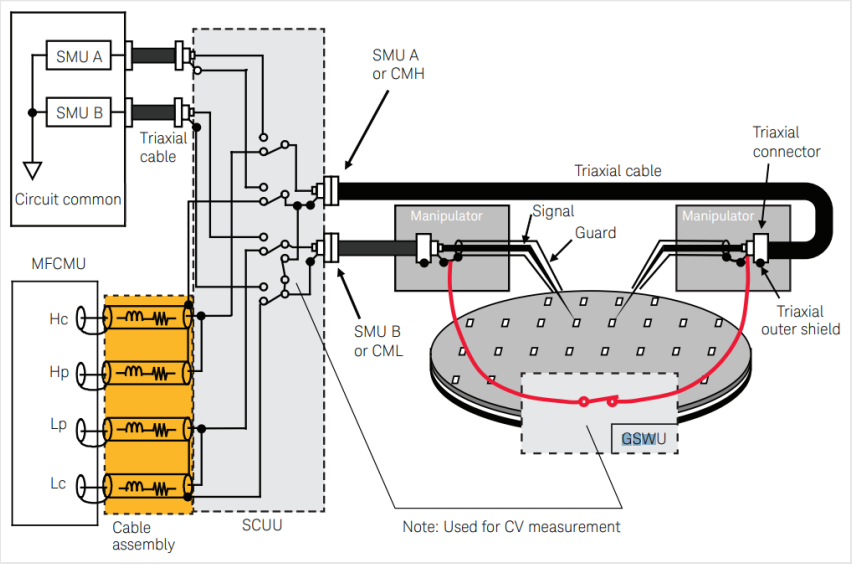

Figure 67. Grounding Switching Unit connection to device under testing[37].

The connections in the Multi-Frequency Capacitance Measurement Unit (MFCMU) stand for, H_c handles the signal source, H_p is the potential meter, L_c is the current meter, and the L_p is the potential meter to lock the phase of the measurement signal. The shorting of the two probes has an effect on the capacitance in forward bias and is shown in figure 68.

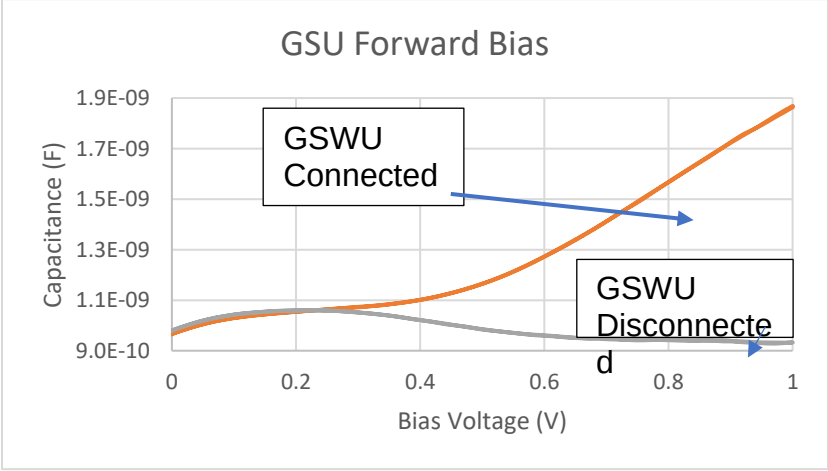

Figure 68. Forward Bias effect by connection of GSWU

Landing the probe at different locations of the electrode yields a widespread in the capacitance in forward bias. This is shown in Figure 69. The actual position of the probe relative to the electrode is displayed in Figure 70.

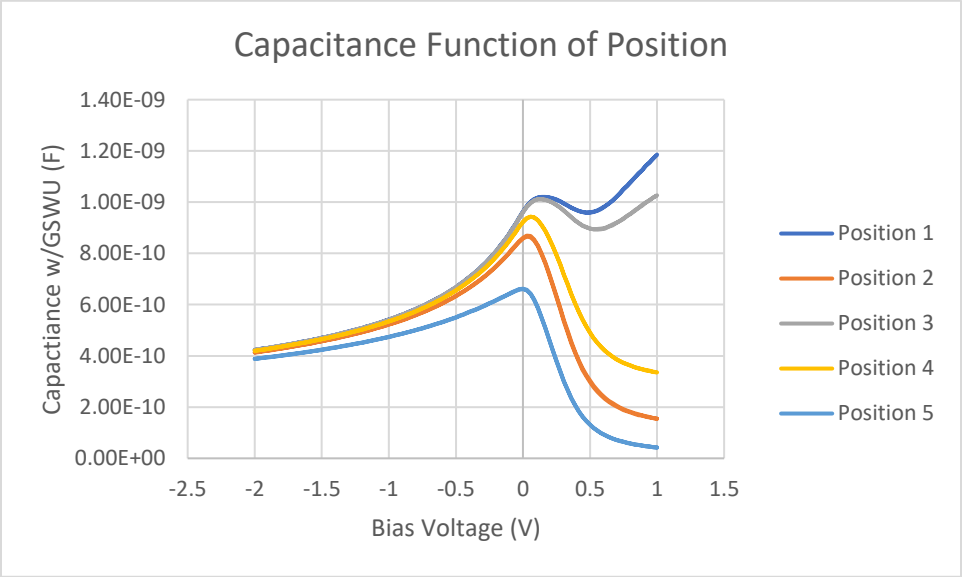

Figure 69. Probe position test. Capacitance vs. voltage.

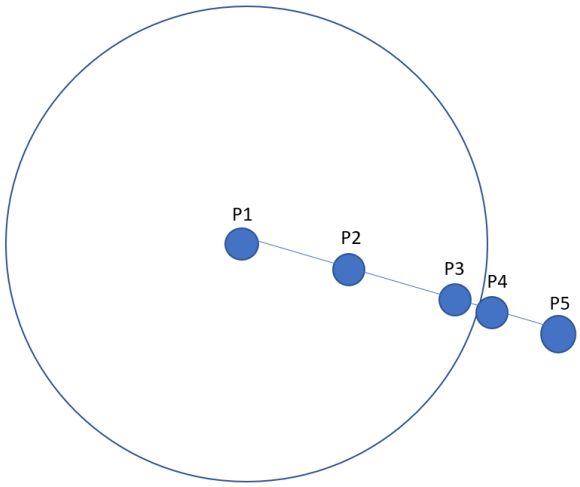

Figure 70. Probe Position on Electrode.

The quality factor in forward is relatively low so the true capacitance is not being measured. Even though the spread cannot be ignored, and this spread could be the result of contact resistance. In figure 71 the probe was raised and lowered followed by a CV measurement. As shown in the graph the measured capacitance in forward bias differs for each curve.

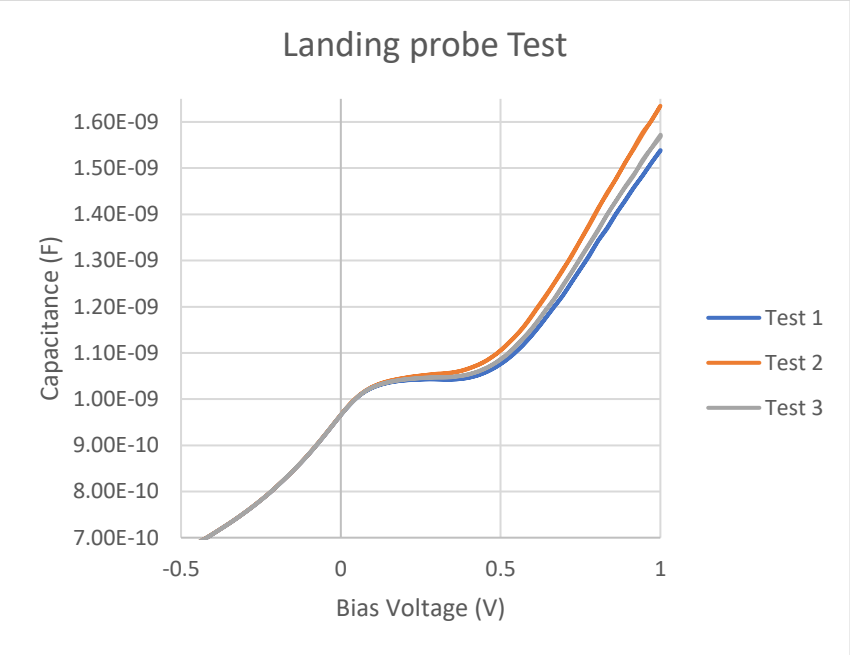

Figure 71. Landing probe test same location on electrode.

The graph above demonstrates the effect of a landing probe test. Test 1 began with landing the probe in the center of the electrode. After the test commenced the probe was lifted via the Summit 12000 automated control system. The tests ceased after the third trail since it was obvious the forward bias capacitance was affected by the landing of the probe multiple times. The series resistance from the probe landing seems to have an influence in forward bias but no in reverse. Landing the probe multiple times in the

same location causes the probe to dig in deeper to the electrode. The electrode should be an equipotential surface but the test above says otherwise.

VI. SUMMARY

This thesis focused on the electrical characterization of NiFeO thin films for the purpose of Resistive Random Access Memory device (RRAM) and novel heterojunctions devices. A sputter through mask was designed and created and used to make device wafers containing multiple Schottky diodes and NiFeO/n-Si heterojunctions. Devices sputtered at low oxygen concentration show hysteresis and thus resistive switching. The ratio between the high and low resistive state is less than a factor 10 and the results suggest that the observed effects are due to the charging of defects states. Devices sputtered at high oxygen concentration on n-type silicon show no hysteresis but strong rectifying effects. Rectifying effects were not observed from the devices made on p-Si. CV measurements were used to estimate the carrier concentration in the NiFeO thin films sputtered at high oxygen concentration to be on the order of 8×10^{16} cm^{-3}. The strong rectifying properties of the high oxygen flow devices on n-Si might be useful as selectors in RRAM devices and as electron blockers in photovoltaic devices and photodetectors. The mobilities calculated for NiFeO high oxygen flow are reported in the table below. Several different techniques were used to calculate the mobilities. The CV mobility focuses on the acceptor concentration while the IV mobilities cannot distinguish which carrier is dominate. The mobilities calculated with the V_x used different resistances depending on the lateral or perpendicular resistivity. The small perpendicular resistance used gets the mobility in close agreement with the CV analysis.

Table 12. Mobility Summary for High Oxygen Flow NiFeO using multiple techniques

Au/NiFeO/n-Si	**Mobility (cm^2/Vs)**
JV Curve Fit Constant	4E-7
CV Curve	8E-3
Literature NiO	1-100
Vx with 10000 Ohm	6.5E-7
Vx with 10 Ohm	6.5E-4
Vx with 5.56 Ohm	8.39E-4

VII. SUGESTIONS FOR FUTURE WORK

For future work to determine the characteristics of NiO and PyO the following parameters should be investigated: mobility (μ_p), carrier density (p), and effective mass (m_p) of the NiFeO thin films. Also, the electron affinity (χ) of NiFeO should be determined from the band offset of the heterojunction devices. There are quite a few ways of measuring the mobility of a semiconductor. Three measurements are available to the students, conductivity mobility, hall effect mobility, and magnetoresistance mobility. Conductivity mobility was performed in this thesis. The Hall effect mobility method is widely available and is commonly used for semiconductors. The weakness of this method lies with the special sample requirements and difficulty predicting the Hall scattering factor. Special geometrics are needed so that contacts made can be soldered onto the fabricated film. Students have a Bio-Rad (Hall, polaron) system available that performs Hall measurements in the MBE (Molecular Beam Epitaxy) lab. The HL5500PC is a high-performance Hall Effect Measurement System. It enables measurements of resistivity, carrier concentration, and mobility for many different semiconductors at two temperature (i.e. room temperature and 77K). The geometries that this system needs can have Van der Pauw, bar or bridge. The following figure 72 shows an example of how one sets up and performs this measurement.

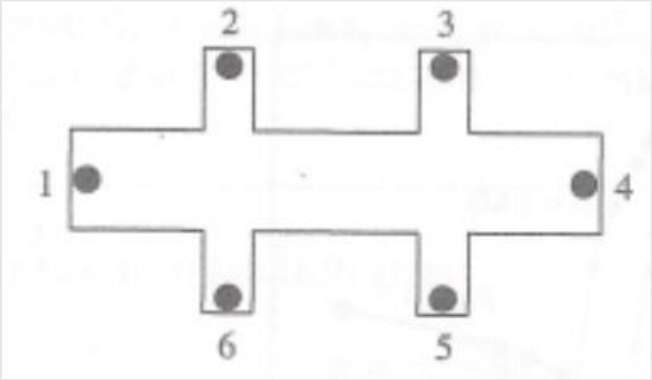

Figure 72. Device Connection Schematic for Hall Measurement.

Position 1 is the current source and position 4 is the current sink. Positions 2 and 6 along with 3 and 5 is where the hall voltage is measured. The voltages between 2 and 3 along with 6 and 5 is where the resistivity is measured in the absence of an applied magnetic field. The Hall coefficient (R_H) is defined as:

$$R_H = \frac{dV_H}{BI} \tag{7.1}$$

Once the resistivity and Hall coefficient are determined the Hall mobility can be calculated by the following equation.

$$\mu_H = \frac{|R_H|}{\rho} \tag{7.2}$$

Now here is the tricky part, once the hall mobility has been calculated it is time to find the mobility of the electrons and holes. This is possible through the following relationship.

$$\mu_H = r\mu_p \; ; \; \mu_H = r\mu_n \tag{7.3}$$

The Hall scattering factor (r) is what makes this technique very complicated. This factor is a function of the magnetic field and the temperature of the sample. The

scattering factor (r) also depends on what kind of scattering mechanism is affecting the charge carriers. Two scattering mechanism effect the factor which are impurity scattering and lattice scattering. The scattering factor is defined as.

$$r = \frac{\langle \tau^2 \rangle}{\langle \tau \rangle^2} \tag{7.4}$$

Where τ is defined as the mean time between carrier collisions. To determine what scattering mechanism is dominating the system a temperature series must be measured. Determining the mobility and plotting vs a temperature log scale will determine the scattering mechanism. The following figure 73 demonstrates what the results should look like.

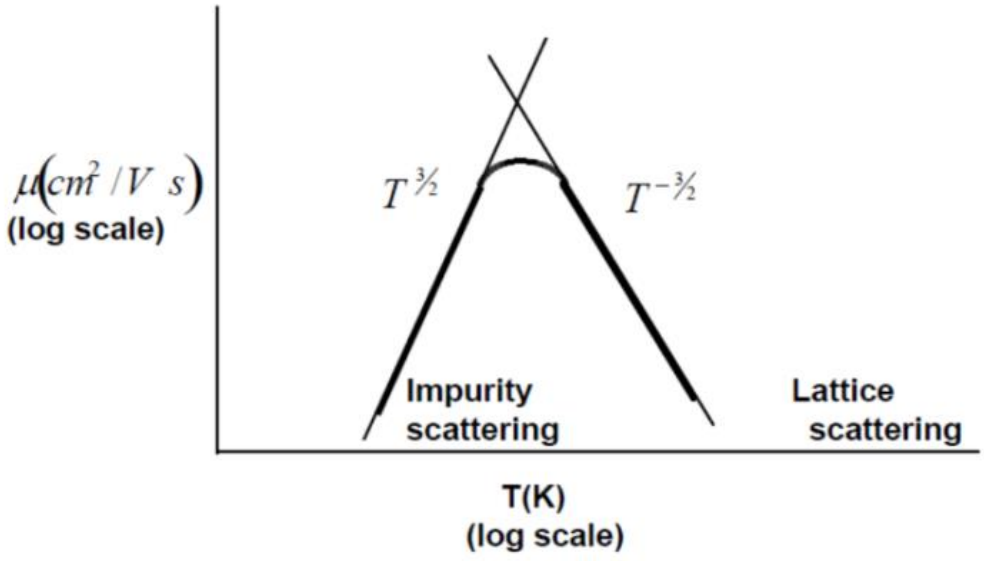

Figure 73. Mobility vs. Temperature. Scattering mechanism determination.

Two bands are in the valance band and at two points one band dominates but the curvature is small and therefore a larger effective mass for the holes is expected as can be understood from the following equation:

$$m_{ij}^{*} = \frac{\hbar^2}{\frac{\partial^2 E(k)}{\partial k_i \partial k_j}} \tag{7.5}$$

Very little scattering opportunities for the holes exists in NiFeO as the valance band near the valence band edge only shows one band so τ is not negatively impacted. Note that the top of the valence band is caused by the Fe atoms. There are two Fe atoms per unit cell for this calculation, so that is why we see two bands. It is clear that both are not identical. The effective mass for the electrons is smaller since the curvature at the bottom of the conduction band is larger. Also, there are no additional electron bands so the τ of the electrons is not negatively affected by multiple scattering opportunities. So, we expect the electron mobility to be larger than the hole mobility for NiFeO. Note that the story is different for NiO (see figure below).

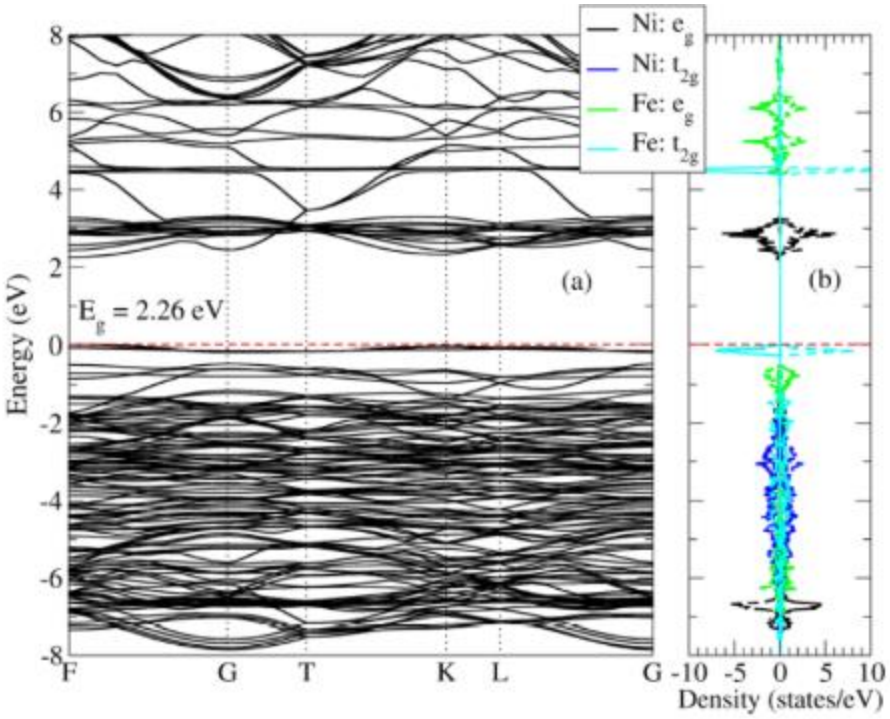

Figure 74. Band structure of $Ni_{0.75}Fe_{0.25}O$. The bandgap resides in the F zone as the red dashed line is the Fermi energy at 0eV[15].

According to the DFT calculations NiO is an indirect bandgap semiconductor[15] see Figure 5. We expect the electron effective mass in NiO to be higher than in NiFeO. Also, hole effective mass is smaller for NiO than for NiFeO as the top of the valence band is more curved for NiO than for NiFeO.

APPENDIX SECTION

A. The following graph describes the IV characteristic of devices made by low oxygen flow of NiFeO grown on p type silicon with gold electrodes, Figure 44. All observations regarding the attempt at modeling the current voltage relationship is an approximation.

Bias Voltage Sweep 1	Current Voltage Relation
Forward Bias V>0	
4 - 3.04V	Negative Differential Resistance
2.96 - 0.48V	$I \approx V^3$
0.4 - 0.2V	$I \approx V$, $R=3.33 \times 10^5 \Omega$
0.2 - 0.08V	Negative Differential Resistance
0V	$1.27 \times 10^{-7} A$
Reverse Bias V<0	
0 - 0.48V	$I = 1 \times 10^{-7.663V}$
0.56 - 4V	$I = 4 \times 10^{-6} e^{-1.351V}$
Bias Voltage Sweep 2	Current Voltage Relation
Reverse Bias V<0	
4 - 3.9V	Negative Resistance
3.9 - 3.7	Negative Differential Resistance
3.68 - 0.56	$I \approx V^{2.93}$
Forward Bias V>0	
0 - 1V	$I = 6 \times 10^{-7} e^{3.83V}$
1 - 2V	$I \approx V$, $R = 50000 \Omega$
2 – 3V	$I = 4 \times 10^{-6} e^{1.06V}$
3 – 4V	$I = 3 \times 10^{-7} e^{2V}$.

B. The sample thicknesses were measured with an ellipsometer and the results are presented in the following table.

Sample Name	Ellipsometer Thickness (nm)	Error ± nm	MSE
41519	23	1	4.6
042519A	177	6	3.2
052618-01	193	8	4.4
052819-02	16	2	13.5
051618-02	75	2	3.2
052818-04	91	2	2.6
052818-03	91	2	2.3
51718-03	196	19	9.6
52618-02	190	10	5.3
51718-02	116	15	12.8
51718-01	114	14	12.1
052818-01	22	3	0.9
12418-01	26	3	0.9

C. Thesis Sample Chart Parameters:

Sample Name	051618-02	051718-01	051718-02	051718-03	052618-01	052618-02
Substrate	Si : P-type	Si : N-type	Si : P-type	Si : P-type	Si : P-type	Si : N-type
Oxide Layer	NiFeO	NiO	NiO	NiO	NiFeO	NiFeO
Electrode	Pt	Pt	Pt	Pt	Au	Au
Oxygen Flow Ratio (Ar:O)	45::5	45::5	45::5	45::5	45::5	45::5
HF Clean	No	Yes	Yes	Yes	Yes	Yes
Sputter Time (seconds)	600	600	600	1200	1200	1200
Ellipsometer Thickness (nm)	75 +/- 2	114 +/- 14	116 +/- 15	196 +/- 19	190 +/- 10	16 +/- 2
Back Electrode				Pt		
Wafer Back Contact						
NiFeO Resistivity						
Si Wafer Resistivity						

Continued:

Sample Name	052818-01	052818-02	052818-03	052818-04	12418-01	41518-01	42519 - 01
Substrate	Si : P-type	Si : N-type	Si : P-type	Si : N-type	Si : N-type	Si : N-Type	Si :
Oxide Layer	NiFeO	NiFeO	NiFeO	NiFeO	NiFeO	NiO/PyO	NiO/PyO
Electrode	Au	Au	Au	Au	Au	Pt	Pt
Oxygen Flow Ratio (Ar:O)	30::20	30::20	45::5	45::5	30::20	30::20	45::5
HF Clean	Yes	Yes	Yes	Yes	Yes	Yes	Yes
Sputter Time (seconds)	1200	1200	600	600	1200	1200	1200
Ellipsometer Thickness (nm)	22 +/- 0	16 +/- 2	91 +/- 2	91 +/- 2	26 +/- 0	177 +/- 12	177 +/- 12
Back Electrode						Pt	Pt
Wafer Back Contact	Al	Al					
NiFeO Resistivity							
Si Wafer Resistivity							

D. Die code for wafer mapping.

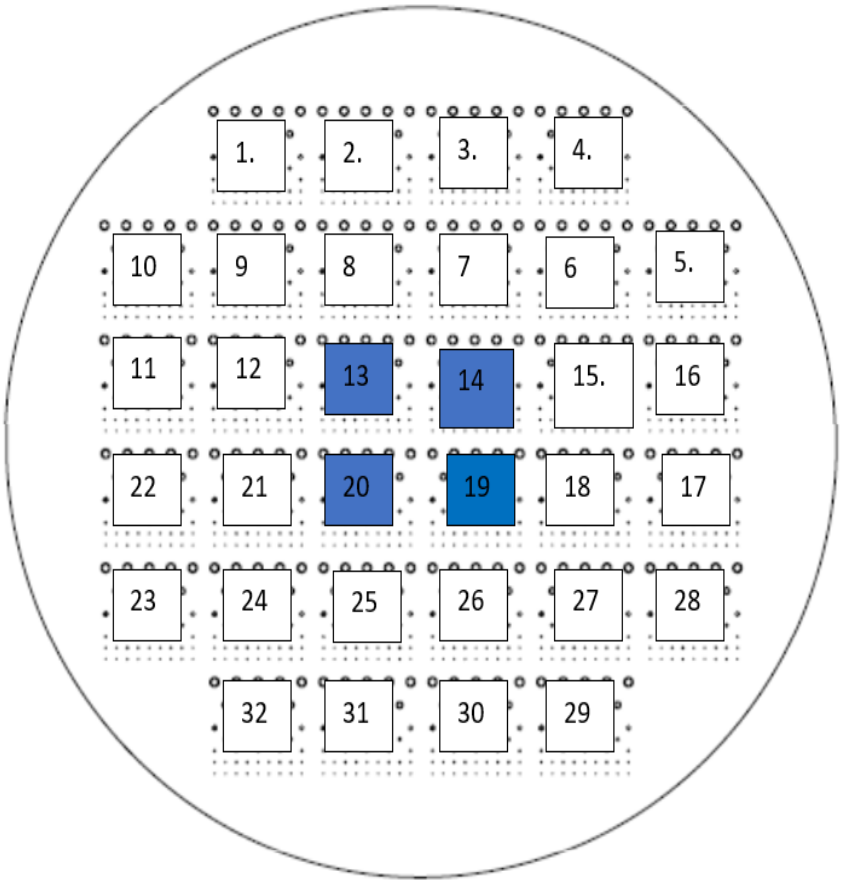

LITERATURE CITED

[1] S. Seo *et al.*, "Reproducible resistance switching in polycrystalline NiO films," *Appl. Phys. Lett. 85*, 5655, Volume, 85, Issue 23, 2004.

[2] H. Akinaga and H. Shima, "Resistive random access memory (ReRAM) based on metal oxides," *Proc. IEEE*, vol. 98, no. 12, pp. 2237–2251, 2010.

[3] X. Yang, J. Guo, Y. Zhang, W. Liu, and Y. Sun, "Hole-selective NiO:Cu contact for NiO/Si heterojunction solar cells," *J. Alloys Compd.*, vol. 747, pp. 563–570, 2018.

[4] B. Parida *et al.*, "Nanostructured-NiO/Si heterojunction photodetector," *Mater. Sci. Semicond. Process.*, vol. 71, no. July, pp. 29–34, 2017.

[5] A. H. Berg, G. S. Sahasrabudhe, R. A. Kerner, B. P. Rand, J. Schwartz, and J. C. Sturm, "Electron-blocking NiO/crystalline n-Si heterojunction formed by ALD at 175°C," *Device Res. Conf. - Conf. Dig. DRC*, vol. 2016-Augus, pp. 1–2, 2016.

[6] F. Menchini *et al.*, "Application of NiOx thin films as p-type emitter layer in heterojunction solar cells," *Phys. Status Solidi Curr. Top. Solid State Phys.*, Volume 13, Issue 10-12, 2016.

[7] W. J. Geerts, N. A. Simpson, A. D. Woodall, and M. S. Compton, "Indium tin oxide thin films deposited at low temperature using dual ion beam sputtering," in *Materials Research Society Symposium Proceedings*, Volume 1699, 2014.

[8] A. H. Berg, G. S. Sahasrabudhe, R. A. Kerner, B. P. Rand, J. Schwartz, and J. C. Sturm, “Electron-blocking NiO/crystalline n-Si heterojunction formed by ALD at 175°C,” in *Device Research Conference - Conference Digest, DRC*, 2016, vol. 379, Issue 38, pp, 2392-2398, 2016-Augus.

[9] M. S. Compton, “THE ELECTRIC, MAGNETIC, AND OPTICAL CHARACTERIZATION OF PERMALLOY OXIDE GROWN BY DUAL ION BEAM SPUTTERING,” Thesis, Texas State University, San Marcos, pp. 38,41,56, 2014.

[10] Y. Cui and A. Zakhidov, “ELECTRICAL AND OPTICAL PROPERTIES OF RRAM,” Thesis, Texas State University, pp. 25,30,56, 2016.

[11] M. A. A. Talukder, “INFLUENCE OF OXYGEN FLOW ON THE MICROSTRUCTURE, RESISTIVITY, AND FARADAY ROTATION OF REACTIVE RF SPUTTERED NIO AND FE-DOPED NIO THIN FILMS,” Thesis, Texas State University, San Marcos, pp. 85,99, 2017.

[12] M. A. A. Talukder, Y. Cui, M. Compton, W. Geerts, L. Scolfaro, and S. Zollner, “FTIR Ellipsometry Study on RF sputtered Permalloy-Oxide Thin Films,” in *MRS Advances*, 2016, pp. 1(49):3361-3366.

[13] T. S. U. Chandler Hutton, T. S. U. Talukder, Md Abdul Ahad, T. S. U. Nick Talbert, and T. S. U. Geerts, Wilhelmus J., “Electrical Characterization of NiO Thin Films,” in *Texas Section APS Spring Meeting, Tarleton State University,Poster Presentation*, 2017.

[14] F. J. Twagirayezu, “THEORETICAL AND EXPERIMENTAL DETERMINATION OF PROPERTIES OF NiO AND Fe-doped NiO,” Thesis, Texas State University, San Marcos, pp. 51,99,100,101. 2017.

[15] John Emil Petersen III, “Impurities in Antiferromagnetic Transition-Metal Oxides - Symmetry and Optical Transitions,” PhD Disseration, Texas State University, pp, 29,49,53,60. 2017.

[16] S. A. Campbell, *Fabrication Engineering at the Micro- and Nanoscale*. pp, 271-344, 2008.

[17] M. Ohring, *The Materials Science of Thin Films*. pp, 151, 161. 2013.

[18] D. L. Smith and D. W. Hoffman, “Thin-Film Deposition: Principles and Practice,” *Phys. Today*, pp, 56,109,466 1996.

[19] “AJA Orion, change targets, common error.” [Online]. Available: http://www.nanophys.kth.se/nanophys/facilities/nfl/aja/manual-web/change-targ-sebbe/target_change_and_common_err.html. [Accessed: 10-Oct-2019].

[20] J. N. Tompkins, Harland G., Hilfiker, *Spectroscopic Ellipsometry Practical Application to Thin Film Characterization*. New York: Momentum Press, LLC, pp, 14, 19, 32, 58, 2016.

[21] F. Pedrotti, *Introduction to optics (third edition)*. pp, 353, 2007.

[22] D. K. Schroder, *Semiconductor Material and Device Characterization: Third Edition*. pp, 81,161, 188, 294, 585. 2005.

[23] “Hirox Digital Microscope.” [Online]. Available: [Online]. Available: https://tracs.txstate.edu/access/content/group/42e1e849-eeef-406b-b0e0-bfe601845211/Equipment/Hirox%20Digital%20Microscope/SOP/190603%20Hirox%20Digital%20Microscope%20SOP.pdf [Accessed: 10-Oct-2019].

[24] G. Ma, X. Tang, H. Su, H. Zhang, J. Li, and Z. Zhong, “Effects of electrode materials on bipolar and unipolar switching in NiO resistive switching device,” *Microelectron. Eng.*, pp 17-20, volume 124, 2014.

[25] X. Yan, Y. Li, J. Zhao, Y. Xia, M. Zhang, and Z. Liu, “Resistive switching model change induced by electroforming in α-Fe<inf>2</inf>O<inf>3</inf> films,” *Phys. Lett. Sect. A Gen. At. Solid State Phys.*, pp, 2392-2395, Vol. 379, Issue 38, 2015.

[26] K. C. Kao, *Dielectric Phenomena in Solids*. Chapter 5, 2004.

[27] M. A. Lampert and P. Mark, *Current Injection in Solids*. New York: Academic Press, Chapter 2, 1970.

[28] T. S. U. Elizabeth G. LaBlanc, T. S. U. Compton, Maclyn Stuart, and T. S. U. Geerts, Wilhelmus J., “The Dielectric Properties of Permalloy-Oxide,” in *Poster Presentated at WISE Conference*, 2013.

[29] Shimeng Yu, *Resistive Random Access Memory (RRAM) From Devices to Array Architectures*. Pheonix: Morgan & Claypool Publishers, pp, 5,6,25,26, 2016.

[30] D. J. Seong, M. Jo, D. Lee, and H. Hwang, “HPHA effect on reversible resistive switching of Pt/Nb-doped SrTiO 3 Schottky junction for nonvolatile memory application,” *Electrochem. Solid-State Lett.*, pp. H168, Vol. 10, Issue 6, 2007.

[31] I. H. Inoue and A. Sawa, “Resistive switchings in transition-metal oxides,” in *Functional Metal Oxides: New Science and Novel Applications*, pp. 443-463, DOI: 10.1002/9783527654864.ch16, 2013.

[32] J. Zhu *et al.*, “ Resistive Switching Characteristics of Resistive Random Access Memory Based on a Ba x Sr 1-x TiO 3 Thin Film Grown by a Hydrothermal Method ,” *IEEE Electron Device Lett.*, pp. 1411-1414, Vol. 40, Issue 9, 2019.

[33] F. C. Chiu, “A review on conduction mechanisms in dielectric films,” *Advances in Materials Science and Engineering*. pp. 1-18, Vol 2014, 2014.

[34] *Heterojunctions and Metal Semiconductor Junctions*. Chapter 1-2, 1972.

[35] M. C. Richard S. Muller, Theodore I. Kamins, *Device Electronics for Integrated Circuits*. pp. 20,32,33,151,162,166,187,253,387. 2003.

[36] Y. Kokubun, S. Kubo, and S. Nakagomi, “All-oxide p-n heterojunction diodes comprising p-type NiO and n-type β-Ga2O3,” *Appl. Phys. Express*, Volume 9, Issue 9, Article number 091101, 2016.

[37] K. Technologies, “The Parametric Measurement Handbook 4th Edition.” pp. 33-51,77,78,85,178,179,180,198

[38] Binod D.C., Andres Oliva, Anival Ayala, Shankar Acharya, Fidele Twagirayezu, James Nick Talbert, Luisa M. Scolfaro, Wilhelmus J. Geerts, “Magnetic Properties of reactive co-sputtered NiFe-oxide samples”, IEEE Trans. on Magn. 55 (2019) 2900205, pp. 2900205-1-6, DOI: 10.1109/TMAG.2018.2866788.

[39] Fidele J. Twagirayezu, Md. Abdul Ahad Talukder, Wilhelmus J. Geerts, "Magnetic Properties of RF sputtered NiO and Ni0.8Fe0.2O1-d samples grown on SiO2/Si substrates, accepted for publication in Materials Research Innovations, July 19 2018, https://doi.org/10.1080/14328917.2018.155879